12-18-2013

Heterojunction Structures for Photon Detector Applications

Don Duleepa P. Pitigala Kankanakage
Georgia State University

HETEROJUNCTION STRUCTURES FOR PHOTON DETECTOR APPLICATIONS

by

P. K. D. DULEEPA P. PITIGALA

Under the Direction of Prof. A. G. Unil Perera

ABSTRACT

The work presented here report findings in (1) infrared detectors based on p-GaAs/AlGaAs heterojunctions, (2) J and H aggregate sensitized heterojunctions for solar cell and photon detection applications, (3) heterojunctions sensitized with quantum dots as low cost solar energy conversion devices and near infrared photodetectors.

(1)A GaAs/AlGaAs based structure with a graded AlGaAs barrier is found to demonstrate a photovoltaic responsivity of ~ 30μA/W (~ 450mV/W) at the wavelength of 1.8 μm at 300K. Additionally the graded barrier has enhanced the photoconductive response at 78 K, showing a responsivity of ~ 80μA/W with a $D^*=1.4\times10^8$ Jones under 1V bias at 2.7 μm wavelength. This is an approximately 25 times improvement compared to the flat barrier detector structure, probably due to the improved carrier

transport, and low recapture rate in the graded barrier structure. However, these graded barrier devices did not indicate a photoresponse with photoconductive mode at 300K due to high shot noise. Additionally, two generation-recombination noise components and a 1/f noise component were identified.

A series of GaAs/AlGaAs multilayer hetero-junction structures were tested as thermal detectors. A superlattice structure containing 57% Al fraction in the barrier and 3×10^{18} cm^{-3} p-doped GaAs emitter showed the highest responsivity as a thermal detector with a TCR of ~ 4% K^{-1}, at 300K.

(2)The photovoltaic properties of heterojunctions with J-/ H- aggregated dye films sandwiched between n– and p-type semiconductors were investigated for potential application as solar cells and IR detectors. Films of cationic dye Rhodamine-B-thiocyanate adsorbed on Cu_2O substrate are found to form organized dye layers by self-assembled J- aggregation, resulting in large red-shifts in the photo - response. Additionally, cells sensitized with a pentamethine cyanine dye exhibited a broad spectral response originating from J- and H-aggregates. The photocurrent is produced by exciton transport over relatively long distances with significant hole-mobility as well as direct sensitized injection at the first interface.

(3) A ZnO/PbS-QD/Dye heterostructure had enhanced efficiency compared to ZnO/Dye heterostructure as a solar cell. Furthermore, a ZnO/PbS-QD structure has demonstrated UV and NIR responses with 4×10^5V/W (390 nm) and 5.5×10^5 V/W (750 nm) under 1V bias at 300K.

INDEX WORDS: Photodetector, Graded barrier, GaAs/AlGaAs, Infra-red, Noise, Band-gap narrowing, Dye sensitized, Heterojunction, J-aggregates, Solar cells.

HETEROJUNCTION STRUCTURES FOR PHOTON DETECTOR APPLICATIONS

by

P. K. D. DULEEPA P. PITIGALA

A Dissertation Submitted in Partial Fulfillment of the Requirements for the Degree of

Doctor of Philosophy

in the College of Arts and Sciences

Georgia State University

2013

HETEROJUNCTION STRUCTURES FOR PHOTODETECTOR APPLICATIONS

by

P. K. D. Duleepa P. Pitigala

Committee Chair: A. G. Unil Perera

Committee: V. Apalkov

D. R. Gies

A. Kozhanov

R. Mani

B. D. Thoms

K. Tennakone

Electronic Version Approved:

Office of Graduate Studies

College of Arts and Sciences

Georgia State University

December 2013

DEDICATION

This dissertation is dedicated to all the people who inspired, encouraged, supported and guided me in gaining knowledge and understanding.

ACKNOWLEDGEMENTS

I would like to express my deepest gratitude to my supervisor Dr. Unil Perera for his guidance, and encouragement throughout this study. His constant enthusiasm, support, and invaluable suggestions made this work successful. Deepest gratitude is also due to the members of my dissertation committee: Dr. Vadym Apalkov, Dr. Douglas Gies, Dr. Alexander Kozhanov, Dr. Ramesh Mani, Dr. Brian Thoms, and Dr. Kirthi Tennakone for fruitful discussions, technical assistance, and effort in reading and providing me with valuable comments on this dissertation.

I wish to thank Dr. H. C. Liu and his group, and Dr. L. H. Linfield and his group for their GaAs/AlGaAs samples, and Dr. M. Hanary and his group for providing the newly synthesized dyes for this study. I would like to convey special acknowledgement to former members and colleagues Dr. Steven Matsik, Dr. Gamini Ariayawansa, Dr. Viraj Jayaweera, Dr. Ranga Jayasinghe, and Dr. M. S. Shishodia for valuable discussions on the subject matters. I would also like to thank present colleagues in the group: Dr .Yang-Feng Lao, Dr. Jitto Titus, Mr. Justin McLaughlin, Mr. Hiren Patel, Mr. Seyoum Wolde and Mr. Dilip Chauhan for their support and discussion in successful completion of this work. I wish to thank all the individuals of the Department of Physics and Astronomy, and friends for their contribution, friendship, and help.

I also acknowledge funding agencies as; This material is based upon work supported by, or in part by, the U. S. Army Research Laboratory and the U. S. Army Research Office under contract/grant numbers W911NF-08-1-0448 and W911NF-12-2-0035, and The US National Science Foundation under grant numbers ECS-0553051 and ECCS-1232184.

Finally, I take this opportunity to express my profound gratitude to my beloved parents, Mr. & Mrs. P. K. D. Somasiri, and my beloved wife, Indika Senevirathna, for their moral support and patience during my study at GSU.

TABLE OF CONTENTS

LIST OF TABLES

LIST OF FIGURES

1. INTRODUCTION

1.1 Motivation

There are numerous types of electronic devices based on interaction of electromagnetic (EM) radiation with semiconductor materials, which are called optoelectronic devices. Optoelectronics is fascinating field with variety of applications. One type of these optoelectronic devices is the photon detectors with responses in different regions in EM spectrum varying from ultraviolet (UV) to Terahertz (THz). Photon detectors enable humans to observe the EM radiation that are not sensitive to the human vision due to limitation of the sensitivity to frequency/wavelength, or due to low intensity in the visible radiation to be sensed by optical nerves. Another application of the optoelectronic devices is to use as a solar energy to electrical energy converter (solar cell). Even though the solar cells' main application is conversion of solar energy in to electrical energy, it can also be considered as a photon detector. For example, if the response spectrum of the solar cell is broaden beyond the visible spectrum and generate photocurrent or photovoltage through absorption of ultraviolet or infrared radiation. It can be used as ultraviolet or infrared detector with suitable cut on or band pass filters. In the field of solar cells, the dye sensitized solar cells are an emerging technology. It is mainly developed as a low cost solar energy converter to be used as an alternative to solar cells based on silicon and other toxic and expensive inorganic materials. These vast varieties of applications in optoelectronic devices have motivated me in this study.

Work presented in this thesis deals with three different studies in the area of photon detection in the IR region and also topics relevant to photovoltaic solar energy conversion. (1) Chapters 2 to 6 describe infrared detectors based on GaAs/AlGaAs heterojunctions. Chapter 2 describes the photovoltaic response in a device with an AlGaAs graded barrier. Chapter 3 discusses the photoconductive mode response enhancements in graded barrier structures structure and compares their behavior with a well-studied flat barrier structure. Chapter 4 deals with the device noise, which affects the response of the graded barrier devices under photoconductive mode operation at 300 K. Chapter 5 presents a study of

the temperature coefficient of resistance (TCR) in GaAs/AlGaAs heterojunction structures, and its application as an uncooled thermal detector. Chapter 6 discusses the Burstein-Moss and band gap narrowing effect in GaAs and AlGaAs, and their effects on barriers created at the GaAs/AlGaAs hetero-junction under illumination. (2) Chapters 7 and 8 are based on a study with dye sensitized heterojunction devices, sensitized with J-aggregating dyes, which can be developed as low cost solar energy conversion device or a near infrared photodetector. (3) Chapter 9 is a study of a UV-IR dual band system, adopting interband transitions in high band gap semiconductor material ZnO, and PbS quantum dots.

1.2 Electromagnetic radiation

The wavelength range of the electromagnetic spectrum extending from few picometers (pm) to kilometers (km) [1] is divided into seven sub spectral regions named as Gama-ray, X-ray, Ultra-Violet (UV), Visible, Infrared (IR), Microwave, and Radio wave. Out of these, the IR radiation region is further divided in to sub regions known as short wavelength (SWIR), mid-wavelength (MWIR), and long wavelength-IR (LWIR), depending on the wavelength ranging from ~ 0.8 –5 μm, 5 – 30 μm and 30μm -1 mm respectively. Furthermore, the FIR region from ~ 30 μm to 3 mm is also known as the terahertz (THz) region [2].

1.3 UV and IR photodetectors

The human eye is only sensitive to the visible spectrum; therefore, humans are blind to the other regions of the EM spectrum. However, all objects with temperature above absolute zero (0 K) emit radiation with an emission peak determined by the temperature. Unless the temperature of an object is approximately over 900-1000 K it will not emit visible radiation at sufficient intensity to be detected by human eyes. On the other hand, objects with temperature over 4000 K will emit a large amount of UV

radiation, as the maximum emission peak shift towards the UV spectrum. Unlike IR radiation, even though the human eye is not sensitive to UV radiation, exposure to UV radiation can damage the optical nerve in the eye. Detectors sensitive to UV and IR are naturally needed, because useful information can be acquired by analyzing UV and IR emissions/absorptions from objects and different materials.

IR detectors used in diverse variety of civilian and military activities, i.e., estimating heat losses in buildings, quality control of various food items and precision imaging and identification of heat emitting objects. Firefighters use IR detectors to identify the origins of fires and in security and defense sector use them for night vision, and security screening in airports. Additionally IR detectors are used in technological fields such as communication and integrated circuit manufacturing and identifying faulty electrical connections. Furthermore, UV and IR detectors are invaluable in study of astronomical objects to gain information, generally inaccessible through other regions of the electromagnetic spectrum.

1.4 Different types of detectors

Photo detectors are generally categorized on basis of the response spectrum of the device (eg. UV, IR, or THz detectors), or the detection mechanism (photons or thermal). Alternative ways of categorization are based on the type of the junction at the material interface (eg. Homo-junction or Hetero-junction), or the band alignment at the material interface (Type-I, Type-II, or Type-III). Since the work presented in this dissertation is based on photon and thermal detection by hetero-junction systems, only those topics are discussed in the following sections.

Homo-junction devices [3] have an interface of semiconductor materials with the same bad gap, but with two different doping (eg. p-type or n-type), or doping concentrations to create a barrier at the interface. HgCdTe and InSb are two important materials that have been studied as homo-junction IR detectors [4, 5]. In contrast, the hetero-junction devices [6] use two materials of different band-gap to generate a barrier at the interface (eg. GaAs/AlGaAs, InAs/GaSb).

1.4.1 Photon detectors

Photon detectors are based on carrier excitation in semiconductor materials due to absorption from incident radiation causing a net carrier flow, which can be measured as a current or a voltage in the device [7-9]. Photon detectors have much higher sensitivity and fast response time compared to thermal detectors [10].

Photon detectors are divided into two categories known as photovoltaic and photoconductive type based on biasing used in its operation. Photovoltaic devices generate a current or a voltage upon illumination and usually contain p-n or p-i-n type semiconductor junctions, where the notations are representing p – p doped, i - intrinsic, and n – n doped semiconductors. Photovoltaic devices do not require additional bias voltage, although very small applied bias voltages (< 100 mV) are sometimes invoked as a means of amplification.

IR- photoconductive devices respond as changes in net current flow when photo-excited carriers are generated by absorption of IR irradiation. The IR signal strength is generally measured as voltage across a load resistor connected in series with the detector. Photoconductive devices have a dark current due to the applied electric field, and the performance of the device is dependent on the magnitude of this current, as the photoresponse is measured as the difference of the total current under IR exposure and dark current. The dark current is a major source of noise in many optoelectronic devices including IR detectors. Different types of electronic noises and their implication on photon detection are discussed in Section 1.5.

1.4.2 Thermal detectors

Thermal detectors [11] utilizing temperature dependent phenomenon of the detector material. Many temperature dependent properties of materials have been used for detection of infrared radiation. The temperature dependence of electrical resistivity , thermal expansion are familiar temperature

dependent properties of materials, that have used in detecting IR radiation [12] [13]. Pyroelectric detectors utilize the temperature dependent charge separation in the material, known as the pyroelectric effect. Thermal detectors have slower response times compared to photovoltaic and photoconductive photon detectors.

1.5 GaAs/AlGaAs heterojunction photon detectors

Hetero-junction interfacial work function internal photoemission (HEIWIP) detectors typically use the inter-band transition of the carriers over the barrier, created due to the difference in the relevant energy bands of the two materials at the junction interface. GaAs/AlGaAs is one of the commonly used material combinations in hetero-junction type detectors [14]. Alternations of the aluminum fraction in the AlGaAs layer modulate the band gap of the AlGaAs material; hence we can adjust the barrier height of the designed device to match the required IR photon energy to be detected.

1.5.1 Uncooled heterojunction IR photon detectors: Split-off band detectors.

Uncooled detection of infrared radiation is becoming important owing to the necessity of such detection techniques in a wide range of applications in the civilian, industrial, medical, astronomy, and military sectors; as bulky liquid nitrogen tanks or thermo electric coolers (TECs) are not practical for such applications.

Impurity-to-band detectors require very low temperatures for efficient operation. Inter sub-band transition based detectors [10] were introduced In order to overcome the need for very low temperature cooling. On the other hand, Quantum well detectors are based on inter sub-band transitions, but the absorption of normal incident radiation is restricted due to the selection rules [15] and require

45° grating coupled with the device for best performance; therefore, the quantum efficiency of quantum well based devices is low .

HEIWIP detectors [6], based on intra-valence band transitions (light-hole (L-H) to heavy-hole(H-H) transitions or heavy-hole transitions to split-off (SO) band) were introduced to overcome the selection rule limitations. The split-off band infrared detector is a newly developed, emerging device based on the p-doped GaAs/AlGaAs system [16] that utilize hole transition in the H-H / L-H band to SO band as the detection mechanism [16, 17]. The SO band detectors have shown promising results to be developed as an uncooled IR detector [18].

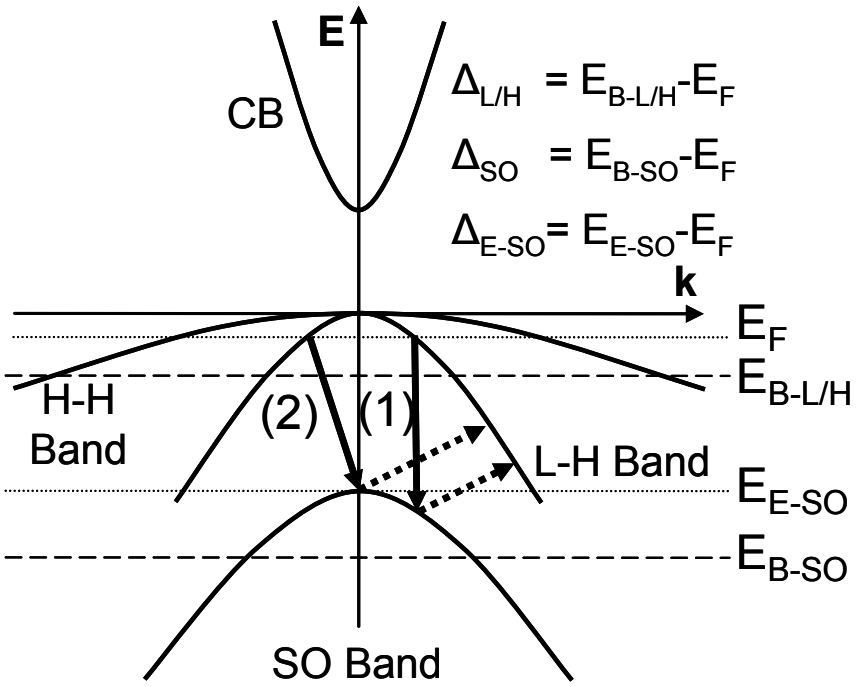

Figure 1-1: Band diagram for the emitter region of split-off band detector, illustrating the different IR detection threshold mechanisms. The horizontal dashed lines EB-L/H and EB-SO indicate the L-H/H-H and split-off band maximum (k=0) positions in the barrier. The horizontal dotted lines EF and EE-SO indicate the Fermi energy and the split-off energy in the emitter at k=0. The arrows indicate the possible threshold transition mechanisms (1) direct transition from L-H band to SO band followed by scatter back to L-H band (2) indirect transition followed by scatter back to L-H band.

A band diagram (E-k) of the emitter region of a SO band detector is shown in Figure 1-1. The detection mechanism is based on the carrier transitions in the three valence bands as shown in Figure 1-1, the L-H and H-H bands which are degenerate at k = 0, and the split-off band s separated from them by an energy $E_{E\text{-}SO}$. At equilibrium the *p*-doped region will have the Fermi level in the L-H and H-H bands, and above the split-off band maximum. Arrows in the Figure 1-1 illustrates the possible threshold transition mechanisms. These could be direct or indirect transitions. When the carrier is in the split-off band, it can escape directly or scatter back into the L-H/H-H bands before escape. In case of a direct transition (solid arrow 1), no phonons are involved; therefore momentum (k) is conserved. Then the excited carrier must scatter back to the L-H band (or the H-H band) to escape as shown by the dashed arrows. A phonon involved indirect transition (arrow 2) is also possible and high energy is required for these transitions. The indirect absorption has two thresholds. (1) The difference of the Fermi energy and the split-off band at k=0 in the emitter ($\Delta_{E\text{-}SO}$) if escape with a scattering. (2) For escape without scattering, the difference between the Fermi energy and the split-off band at k=0 in the barrier (Δ_{SO}). The horizontal dashed lines $E_{B\text{-}L/H}$ and $E_{B\text{-}SO}$ indicate the L-H/H-H and split-off band maximum level (at k=0) in the $Al_xGa_{1-x}As$ barrier. The horizontal dotted lines E_F and $E_{E\text{-}SO}$ are the Fermi energy and the split-off energy at k=0 in emitter region. Even though Δ_{SO} is constant for a given material system, $\Delta_{L/H}$ can be adjusted by varying Al fraction and the doping concentration of the emitter layer[6].

1.6 Noise in optoelectronic devices

Noise is a limiting factor of the performance of optoelectronic devices. 1/f noise, generation-recombination (G-R) noise, Johnson noise, and Shot noise are the main components that can be found in a noise spectrum of a device [19].

1/f noise gets its name due to the proportionality of the amplitude to the inverse of frequency. 1/f noise is further characterized as $1/f^{\alpha}$ where α varies from ~ 0.5 to 2 depending on the gradient in the amplitude vs. frequency [20]. As the α gets larger, the noise decays faster as the frequency increases. Hence, the effect on the device performance is less significant with high α compared to 1/f noise with low α. Furthermore, 1/f noise is one of the common types of noise found in many electronic devices.

Generation-recombination noise, well known as GR noise is a result of a carrier being trapped and released by impurity or defect states in the material in the device [21]. The amplitude of the GR noise is proportional to the trap state density of the material and depends on the growth method of the device.

Johnson noise is caused by the thermal and resistance fluctuations in the device [22]. The Shot noise, also known as quantum noise, depends on the current flow in the device [23]. The Shot noise and the Johnson noise, also known as the white noise, are an important factor for performance of photodetectors as the specific detectivity (D*) is determined by the Jonson noise and Shot noise level using the Eq. 1-1 [1], where, R- is responsivity, A_D – is the electrical aria of the device in cm^2, Δf – is the band width, and Noise- is the white noise density.

$$D^* = \frac{R \times \sqrt{A_D}}{Noise / \sqrt{\Delta f}} (Jones) \qquad \text{Eq. 1-1}$$

1.7 Dye sensitized heterojunction nanostructures

Photoexcited dye molecules which are anchored to a semiconductor surface can inject electrons and holes to the conduction band (CB) and to the valence band (VB), respectively, with proper band alignment [24, 25]. This process is known as dye-sensitization, and it affords a way of transferring energetic carriers (either electrons or holes) to a semiconductor. The electronic coupling of the dye molecule

to the semiconductor surface causes a fast electron injection [26] and effectively circumvents the dissipative processes that generally occur when an electron transits across a surface.

The main difference between the dye sensitized solar cells (DSSC) and p-n homo-junction junction solar cells is the photon energy absorber. In p-n junction solar cells the photon energy is absorbed directly by the carriers in the semiconductor by band gap excitations, but in DSSCs the photon energy is absorbed by the dye chromophores (the part of the molecule defining the color of the dye) and the electron-hole pair is generated in the dye molecule. These electrons and holes are transferred on to the relevant semiconductor material through their chemical bonding.

The DSSCs can be divided in to two groups as photoelectrochemical (PEC) solar cells and dye sensitized solid-state solar cells (DSSSC). The electron transfer processes in both the types are almost same; the difference in these two types is the interface. The PEC cell has an n-type or p-type semiconductor/dye/electrolyte structure and the solid state cells have n-type semiconductor/dye/p-type semiconductor structure. Usually, the material used as n-type semiconductor is TiO_2, and CuI or CuSCN is used as the p-type semiconductor.

1.7.1 Electron transport in DS Solid-State solar cell

An energy band diagram of a DSSSC is illustrated in Fig. 1-2. Briefly the electron transport process is as follows; when the cell is illuminated, the photon energy is absorbed by the dye molecules. The internal energy of the dye molecule arises from ground state (G.S) energy to the exited state (E.S) energy due to the absorbed energy of the photon (the excited dye molecule is denoted as D^*). The dye molecules inject electrons to the conduction band (CB) of the n-type semiconductor. Meanwhile, a hole will be created at the valence band of the p-type semiconductor by donating an electron to dye cation (D^+) (the energy of the dye cation should lie below the valence band of the p-type semiconductor to allow

this transition). Electrons collected in the CB of the n-type material will recombine with the holes in p-type material by traveling through the external path connected across a load resistor.

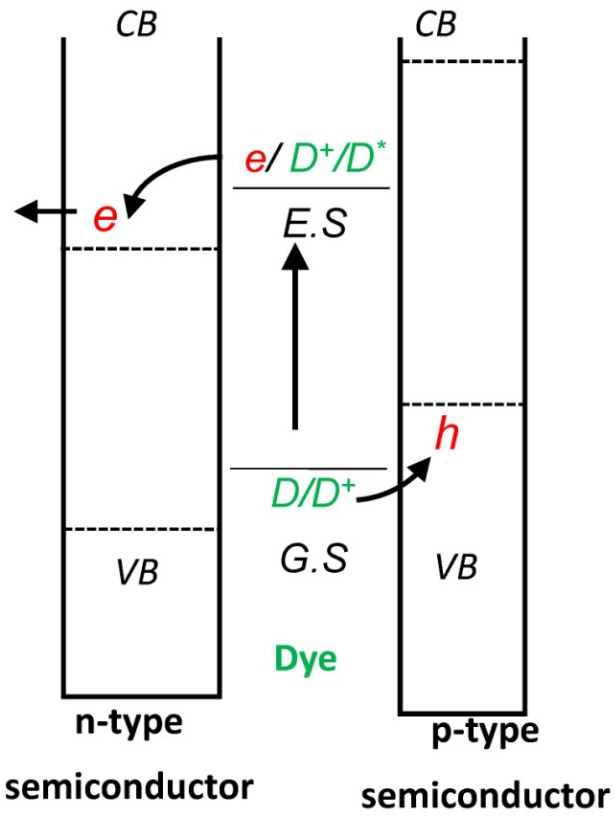

Figure 1-2: An energy band diagram of the DSS Solar Cell. G.S:-Ground state, E.S:- Excited stare, VB:- Valence band, CB:- Conduction band, e- electron, h- hole D- dye with ground state energy, D*- dye with excited state energy, D+ - ionized dye molecules.

1.7.2 H and J aggregates

H-, or J- aggregates of the dye is referred to a self-association of dyes in solution or in a solid/liquid interface owing to strong intermolecular Van Der Waals like attractive forces between the molecules. The aggregates in solution exhibit red or blue shifts in the absorption spectrum as compared to the monomeric molecules. From the spectral shifts, two main aggregation patterns of the dyes in different media have been proposed. The bathrochromically shifts (long-wavelength or red shift) in the absorption spectrum known as J-bands named after E.E. Jelly [27], one of the first workers who investigated these shifts. The other is the hypsochromically shift (short-wavelength or red shift), or the H-bands (H for hypsochromic) of the aggregates. The transition moment coupling of the dye molecules are the main cause of these shifts. Using H- or J- aggregates of dyes the response spectrum of the dye sensitized device can be broadened or shifted to long or short wavelengths in the photon spectrum.

2 UNCOOLED GRADED BARRIER HETEROSTRUCTURES FOR PHOTOVOLTAIC MODE OPERATION

2.1 Introduction

Group III-V semiconductor materials are extremely important for the development of infrared (IR) detectors operating over a wide wavelength range [17, 18, 28, 29]. Most photovoltaic devices are based on p-n junction structures. Use of superlattice structures for infrared photovoltaic devices has gained increasing interest in recent years [30-32]. Photovoltaic response has been demonstrated in multi-quantum-well structures, which generate a photovoltage owing to the Schottky junction characteristics [33]. Furthermore, photovoltaic multi-quantum-well IR detectors with GaAs/AlGaAs superlattice structures, consisting of n-doped GaAs and undoped AlGaAs layers with a graded barrier at one contact end, have also been reported for use at low temperatures [34]′[35]. This chapter demonstrates p-doped GaAs/$Al_xGa_{1-x}As$, emitter/graded barrier structures with different aluminum fractions (x), operating as a photovoltaic detector under uncooled conditions. The zero bias reduces the Joule heating in the device, and also will reduce low frequency noise and dark current.

2.2 Experimental procedure and device structures

Six devices were tested, each consisting of a barrier/emitter/barrier structure between two contact layers; a schematic of the valence band structure is shown in Fig.2- 1(a). Of these six wafers, five had the barriers graded with a decreasing Al fraction (X2) from the emitter end and to (X1) towards the bottom contact end of the structure. The sixth sample had a flat barrier instead of the graded barrier as the control sample. All structures had a constant barrier (X3) between the emitter and the top contact. Device parameters are given in Table 2-1, where X1, X2 and X3 represent the aluminum fractions of the barriers at the bottom contact end and the emitter end of the graded barrier, and in the flat barrier, respectively. Out of the five wafers, three of the graded barriers were grown using continuous alloy frac-

tion variation (SP1005, SP1006, SP1007), whilst the other two (V0727, V0728) were formed by digital alloying as described elsewhere [36].

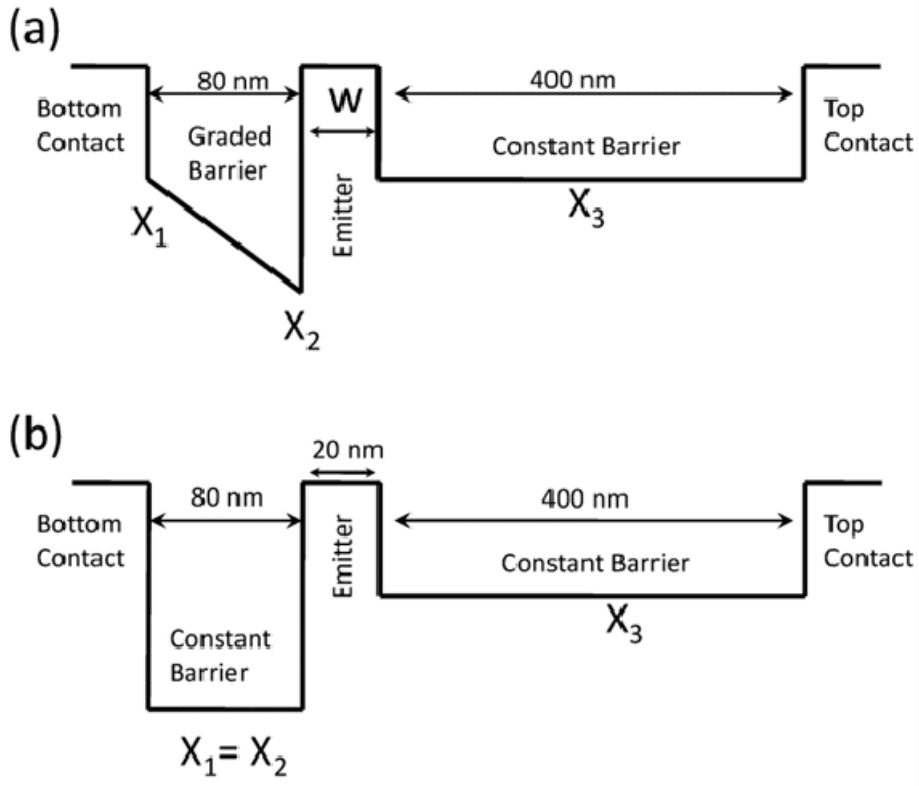

Figure 2-1: Schematic diagram of the valence band structure of the devices: (a) the graded barrier structures and (b) the constant barrier structure. The barrier thicknesses are 80 nm and 400 nm, and the emitter thicknesses (W) and Al fractions (X_j ; j=1..3) are tabulated in Table 2-1. The top contact, bottom contact and the emitter are highly p-doped (10^{19} cm^{-3})

The sample has a constant barrier ($Al_{0.75}Ga_{0.25}As$) on the bottom contact side (instead of the graded barrier) and a small constant barrier ($Al_{0.57}Ga_{0.43}As$) at the top contact side, separated by a single GaAs emitter layer. The emitters were p-doped to $1\times10^{19}cm^{-3}$ in all six wafers. All wafers studied were grown by molecular beam epitaxy, and processed into mesas by wet etching followed by deposition of metal contacts.

Table 2-1: Sample parameter and aluminum fractions at barrier heights of the detector structures (band diagram shown in Fig.2-1.). All samples have contacts and emitters doped to 1×10^{19} cm^{-3}, 80 nm wide graded barrier, and 400 nm wide constant barrier.

Sample	**Emitter** Width (nm)	**Graded Barrier**		**Constant Barrier** Aluminum Fraction (X_3)
		Contact End Aluminum Fraction (X_1)	Emitter End Aluminum Fraction (X_2)	
V0727	20	0.55	1.0	0.55
V0728	80	0.55	1.0	0.55
SP1005	20	0.45	0.75	0.55
SP1006	50	0.45	0.75	0.55
SP1007	80	0.45	0.75	0.55
SP1001	80	0.45	0.75	0.55

2.3 Results and Discussion

Four dominant photoexcitation and carrier transport mechanisms under photovoltaic mode are summarized in Fig 2-2, using the valence band diagram for the graded barrier structures. In the first path, named h1, the exited carriers (holes) in the bottom contact region scatter from the graded barrier and fall back into the bottom contact layer. In the second path (h2), exited carriers have sufficient energy to overcome the higher end of the graded barrier, and are collected at the bottom contact layer even

after scattering off the graded barrier. Therefore, a net charge will be accumulated at the bottom contact. This carrier accumulation generates a shift in the energy levels between the two layers (bottom contact and emitter).

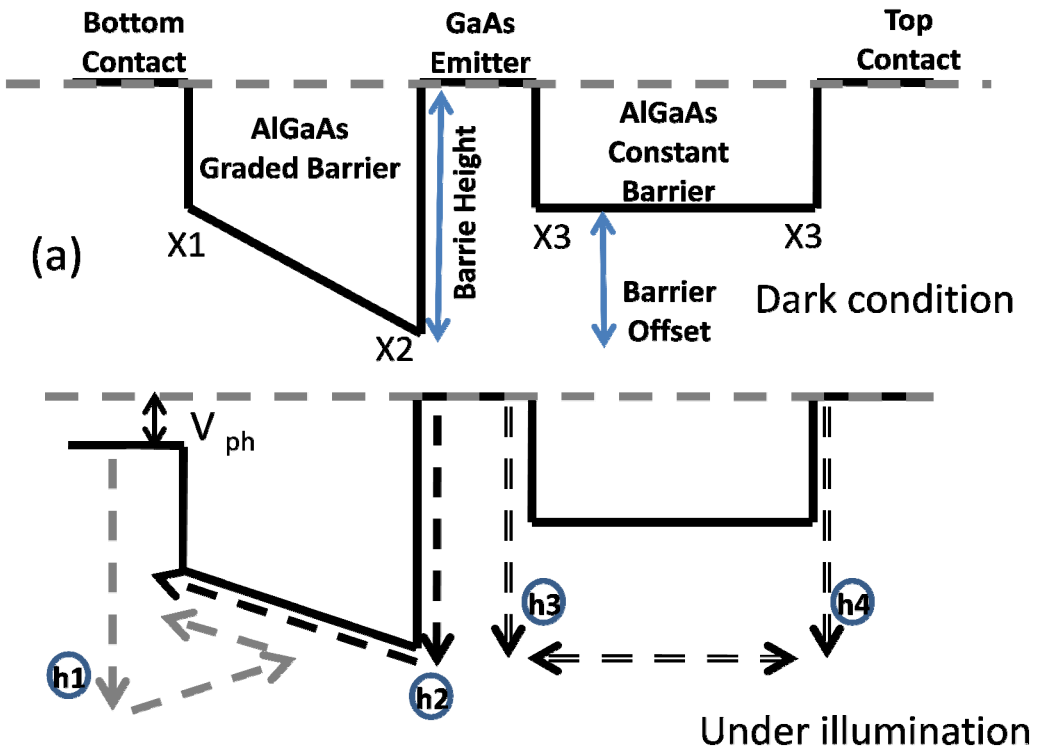

Figure 2-2: Schematic diagram of the valence band alignment in the graded barrier structure before (upper) and after (lower) illumination. X1, X2, and X3 represent the aluminum fractions at the two edges of the graded barrier, and in the flat barrier (see Table 2-1). Carrier transport processes in the structure are illustrated by arrows. When the device is illuminated, exited carriers (holes) will diffuse over the barriers as represented by arrow paths h1, h2, h3 and h4. The transitions h1 and h2 will result in carrier accumulation at the bottom contact. This generates a shift in the Fermi energy between the two contacts, resulting in a photovoltage (V_{ph}).

In the third and fourth paths, h3 and h4 respectively, excited carriers from the emitter (top contact) will pass over the constant barrier and transport to the top contact (emitter) region. The net carrier accumulation at either emitter or top contact will be zero. Therefore, there will be no energy band shift between the top contact and emitter region due to carrier transport between them. Owing to the asymmetry of these carrier transport mechanisms, a photovoltage (V_{ph}) will be generated between the bottom and top contact. For example, a photovoltage of 0.6 mV was observed in V0728, when illuminated with the full spectrum of the IR source (1 μm to 5 μm) of an FTIR spectrometer. This response was linearly proportional to the light intensity.

2.3.1 I-V characteristics

I-V characteristics for V0728 and SP1007 at 300 K at low bias are shown in the Fig. 2-3. The V0728 has the higher resistance (15 kΩ at zero Bias) and lower dark current compared to SP1007 (2.1 kΩ at Zero Bias) throughout the voltage domain. The asymmetry in the I-V diagram is due to the asymmetry in the device structure. The differences in the barrier heights are causing the differences in resistance for the two devices. At negative bias (top contact negative) the slope of the graded barrier becomes less steep; hence the effective barrier height is reduced allowing an increased dark current to flow through the device. Due to the higher resistance, the carrier accumulation in the V0728 will be higher allowing a larger photovoltage buildup compared to the SP1007.

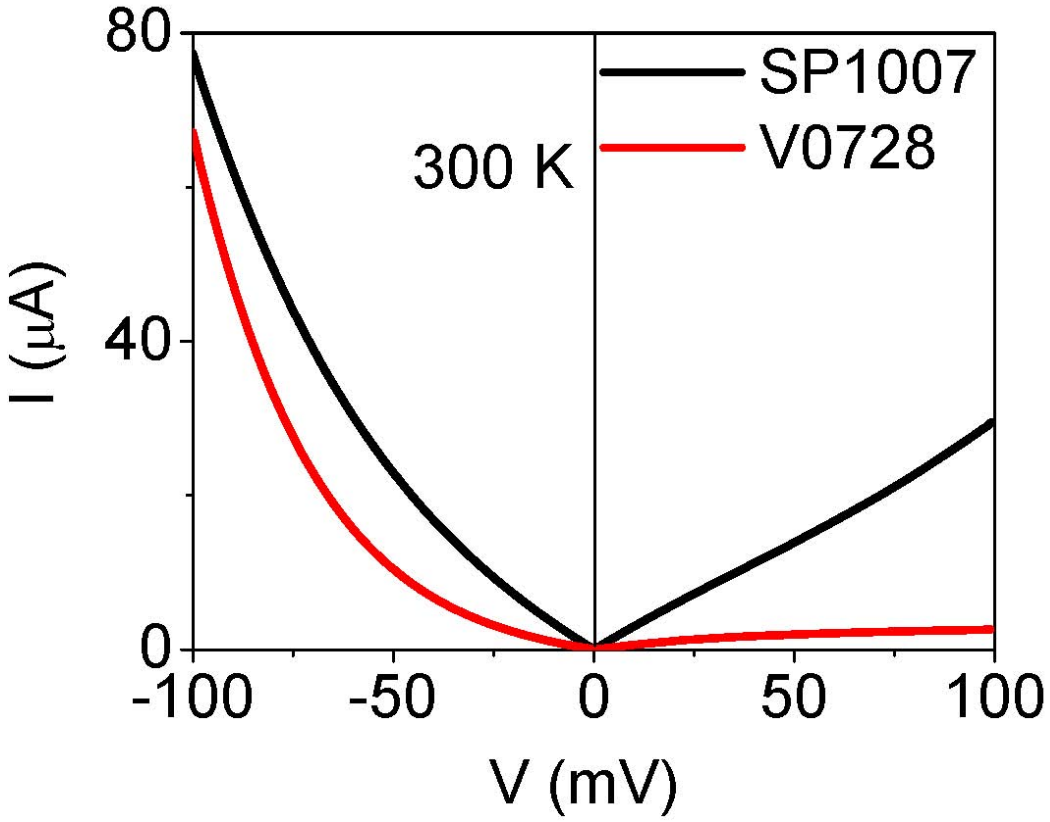

Figure 2-3: IV characteristic curve of the devices V0728 and SP1007 at 300 K. Positive or negative bias indicate, positive or negative voltage applied at the top contact with respect to the bottom contact, respectively.

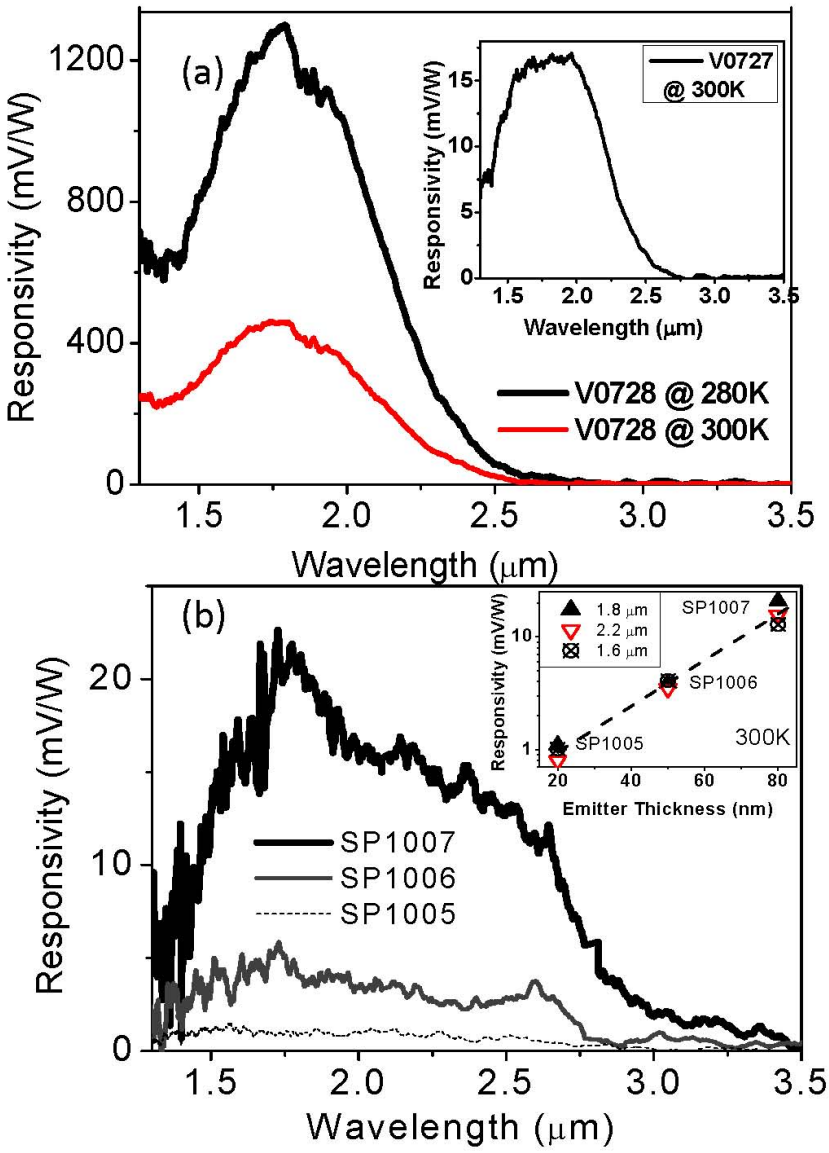

Figure 2-4: (a) The photovoltaic response of V0728 at 280 K and 300 K; the photovoltaic response shows a peak at a wavelength of 1.8 μm and a threshold at 2.6 μm. The photovoltaic responsivity increases with the decreasing temperature. Inset: Responsivity of wafer V0727 at 300K. The responsivity of V0727 is lower owing to the smaller emitter, 20 nm compared to 80 nm in V0728. (b) The photovoltaic response of SP1007, SP1006 and SP1005 at 300 K. The photovoltaic response decreased with decreasing emitter thicknesses (80 nm, 50 nm & 20 nm respectively). A peak response was seen at a wavelength of 1.8 μm, and a threshold was observed at 3.5μm. Inset: The peak responsivity (at 1.8 μm) extracted from response curves of the three devices, which shows an exponential increase in the responsivity with increasing emitter thickness.

2.3.2 Photovoltaic responsivity at room temperature

A photovoltaic response was observed for all the tested devices with a graded barrier (V0727, V0728, SP1005, SP1006 and SP1007) when measurements were conducted at room temperature. As the spectral responsivity measurements and open circuit voltage of the device was measured by a voltage amplifier coupled with the Perkin Elmer system 2000 FTIR. The data was calibrated using responsivity of a bolometer. Out of the tested devices, the highest signal was observed for the device based on the wafer V0728, as expected through the analysis of I-V data. The open circuit voltage responsivity spectra of a device from this wafer at 280K and 300K are shown in Fig. 2-4(a). At 300K, a peak responsivity of 460 mV/W was observed at the wavelength of 1.8 μm and the estimated photocurrent is ~ 30 μA/W. The responsivity has increased as the temperature decreases due to increased charge accumulation with increasing device resistance. The temperature variant responsivity are later shown in section 2.3.6.

The Johnson noise limited specific detectivity value for the device is calculated as ~1.5×10^6 Jones using the Eq.2-1.

$$D^* = R_v \sqrt{\frac{A}{4kTR_0}}, \qquad \text{(Eq. 2-1)}$$

Here, R_v is the responsivity in volts per Watt, R_0 is the resistance at zero bias, A is the area of the device, k is the Boltzmann constant and T is the temperature. When the temperature of the device was reduced, an increase in the responsivity and D* to 1.28 V/W and 2.8×10^6 Jones was observed, respectively. The peak responsivity and D* values at 300K, at 1.8 μm, are summarizeded in Table 2-2. The quantum efficiency (QE) of the devices is calculated to be 0.03% at the peak response.

The responsivity spectra of SP1005, SP1006, and SP1007 at room temperature are shown in Fig.2-4(b). SP1007, having a thicker emitter of 80 nm, shows a higher responsivity compared to the other two wafers (SP1006 and SP1005) which have thinner emitters of 50 nm and 20 nm, respectively. A simi-

lar behavior was observed for V0728 and V0727 (responsivity shown in inset of Fig. 2-4 (a)); the response is higher in V0728 with an 80 nm emitter. Since each wafer has the same doping density in the emitter, the device with a thicker emitter is thus likely to have an increased charge accumulation. The higher photovoltage is a result of a higher number of carriers accumulated in the contact region. Wafer SP1001, which did not have a graded barrier, did not show a photovoltaic response when operated close to room temperatures. Without the graded barrier, there will be no net carrier transport in either direction, and hence no photovoltage should be observed.

2.3.3 Effects of emitter thickness

The ratio of the peak responsivity (1.8 μm) for V0728 to V0727 is ~ 26, whilst for SP1007 to SP 1005 it is ~19. This responsivity increment is much greater than the ratio in emitter thickness. The responsivity increase in the SP devices with emitter thickness is shown in the inset of Fig. 2-4(b), and shows an exponential behavior. This phenomenon has not as yet been fully understood. The difference in the responsivity ratios between V07 and SP samples may, however, be a result of the differences in the rate of scattering at the barriers, owing both to the two different methods used in growth, and also to the difference in the aluminum fractions in the graded barriers (the gradient in the barrier). In addition to the differences in the device resistance, the accumulated carriers may discharge quickly in the SP series devices compared to the V07 series.

2.3.4 Effects of barrier heights

Devices V0728 and V0727 show a photoresponse threshold at ~2.6±0.2μm, while SP1005, SP1006 and SP1007 show a broader response region with a threshold around 3.5±0.2μm. The Arrhenius plot of dark current verses temperature gives the barrier height as ~490±15meV (2.55±0.1μm) and

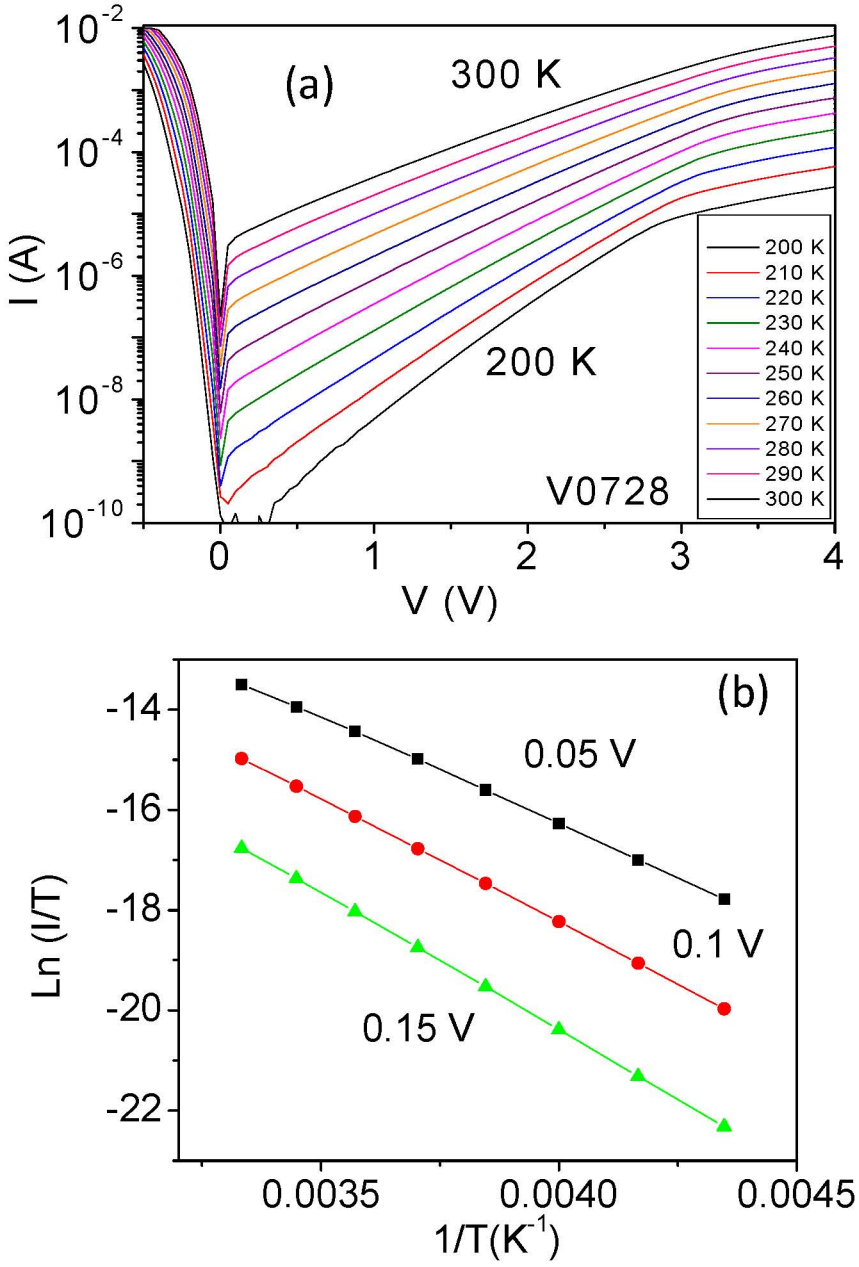

Figure 2-5: The dark current variation with temperature and Arrhenius plot for V0728

~360±10meV (3.44±0.1μm) in agreement with the photovoltaic response threshold. The I-V data and Arrhenius plot for V0728 at three different bias voltages are shown in Fig. 2-5. The barrier height calculated using the Anderson rule, conduction band to valance band ratio (CB:VB) of 60:40 gives a VB barrier height ~610 meV for AlAs/GaAs interface in V07 series (barrier due to difference in aluminum fractions x=1 and x=0) and a barrier height of ~430 meV for the $Al_{0.75}Ga_{0.25}As$/GaAs interface (x=0.75 and x=0) in the SP series. The constant barrier height is ~300 meV (x=0.57 and x=0) for both the sets of devices. Therefore, the barrier offset for V07 and SP samples are ~310 meV (x=0.57 and x=1) and ~130 meV (x=0.57 and x=0.75), respectively. None of the barrier heights calculated by the Arrhenius data are equivalent to any of the barriers or barrier offsets calculated by the 60:40 ratio of the CB:CV alignment at GaAs/AlgaAs interface. The difference in the values obtained by Arrhenius data and Anderson rule can be due to the tunneling effects through the thinner region of the graded barrier. Another reason can be the 60:40 ratio may not reflect the correct band offset for the aluminum fraction, x, > 0.45, as the X- valley becomes lower than the Γ–valley for AlGaAs under this condition and the band gap becomes indirect and lower than the energy difference between VB and Γ-valley [37]. Additionally, different CB:VB ratios ranging from 50:50 to 85:15 can be found in literature [14, 38-40] for GaAs/AlGaAs interface, and the 67:32 (66:34) ratio gives a band offset of 488 meV (365 meV) for V07 (SP) devices agreeing with the values calculated by Arrhenius data (490 ± 15meV and ~360 ± 10meV).

2.3.5 Noise and detectivity

The variation in D* for V0728 with wavelength in both the photoconductive mode (with a bias of -0.1V) and photovoltaic mode (0 V bias) are shown in the Fig. 2-6. The noise generated by the measuring instruments is negligible compared to the device noise. The inset of Fig. 2-6 shows the noise current density (S(f)) of V0728 at a -0.1V bias voltage, and at 0 V bias. At high frequency (f > 10 kHz) the measured noise density is closer to the Johnson noise limit. D* calculated with the measured noise at 10 kHz,

is 1.2 × 10^6 Jones. As a comparison between the photovoltaic and photoconductive modes of operation, sample V0728 was then operated in photoconductive mode under the negative bias (bottom contact positive) for which it was designed. The D* value of 1.5 × 10^6 Jones for photovoltaic operation was significantly higher than the photoconductive value of 3.5 × 10^4 Jones. This indicates the potential for better performances of devices, in the photovoltaic mode of operation using graded barriers at room temperature.

Table 2-2: The responsivity in mV/W and μA/W and specific detectivity (D*) of the devices at 300K and a wavelength of 1.8 μm.

Device No.	***Peak Responsivity***		***D****
	mV/W	μA/W	***(Jones)***
V0727	~17.1	~2.1	6.0×10^4
V0728	~450	~30	1.2×10^6
SP1001	--	---	--
SP1005	~1.1	~1.0	9.9×10^3
SP1006	~3.9	~4.1	3.3×10^4
SP1007	~20.8	~10.4	1.4×10^5

However, the D* obtained for this device is comparatively low compared to other infrared directors working at room temperature and responding in shorter wavelength (< 2μm), such as the p-i-n InGaAs detector with D* of the order of 10^{11} Jones. In contrast, the results shown in this chapter are not from a device designed for optimal photovoltaic mode operation. However, unlike those detectors, graded barrier detectors are intra-band devices, providing wavelength tunability by adjusting the barrier height. Therefore, implementation of the design can lead to uncooled IR detectors for long wavelength

detection. Further improvements of D* are possible by modifying the structure parameters of the graded barrier device, such as having thicker emitters, adjusting the barrier thicknesses, the aluminum composition in the barriers, multiple layers, emitter doping, and substituting the emitter layer with different materials with higher absorption coefficient.

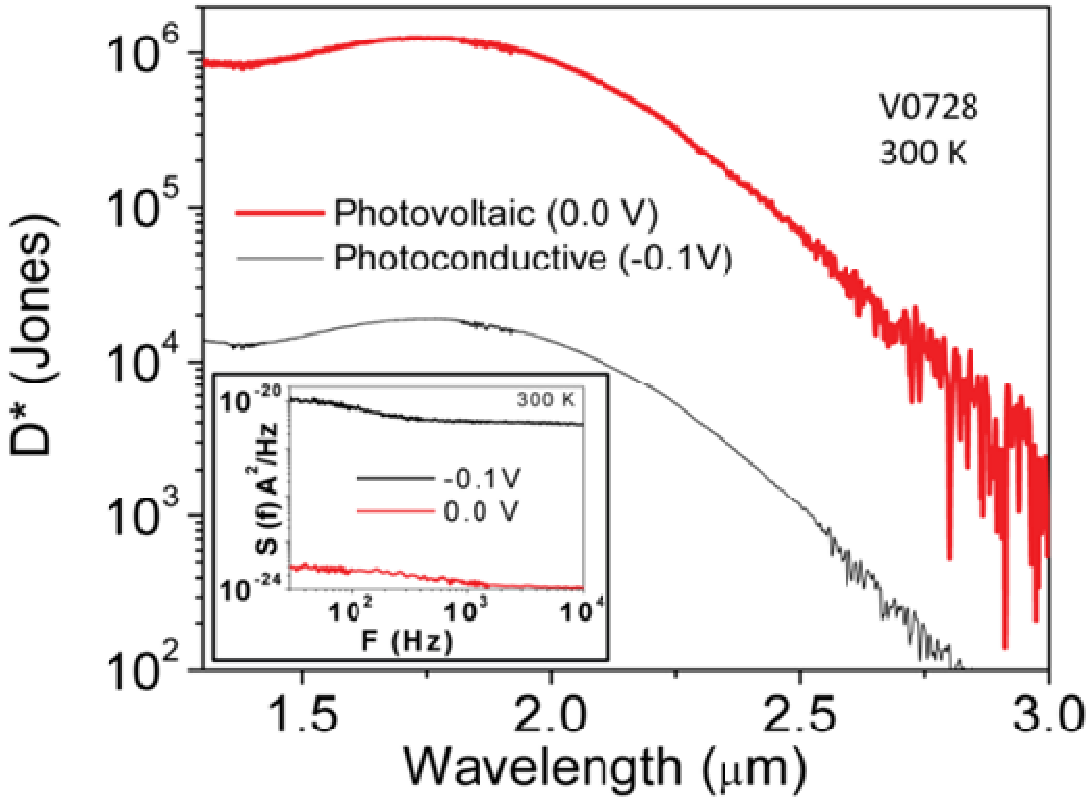

Figure 2-6: Detectivity of V0728 as a function of wavelength in a photoconductive mode (with a bias of -0.1V) and photovoltaic mode (0 V bias) at 300 K. The photovoltaic mode has a higher detectivity due to low noise. Inset: The noise current density (S(f)) of V0728 at -0.1V bias voltage, and 0 V bias, shows a low noise level in the device with 0V bias due to absence of shot noise caused by dark current in the biased device.

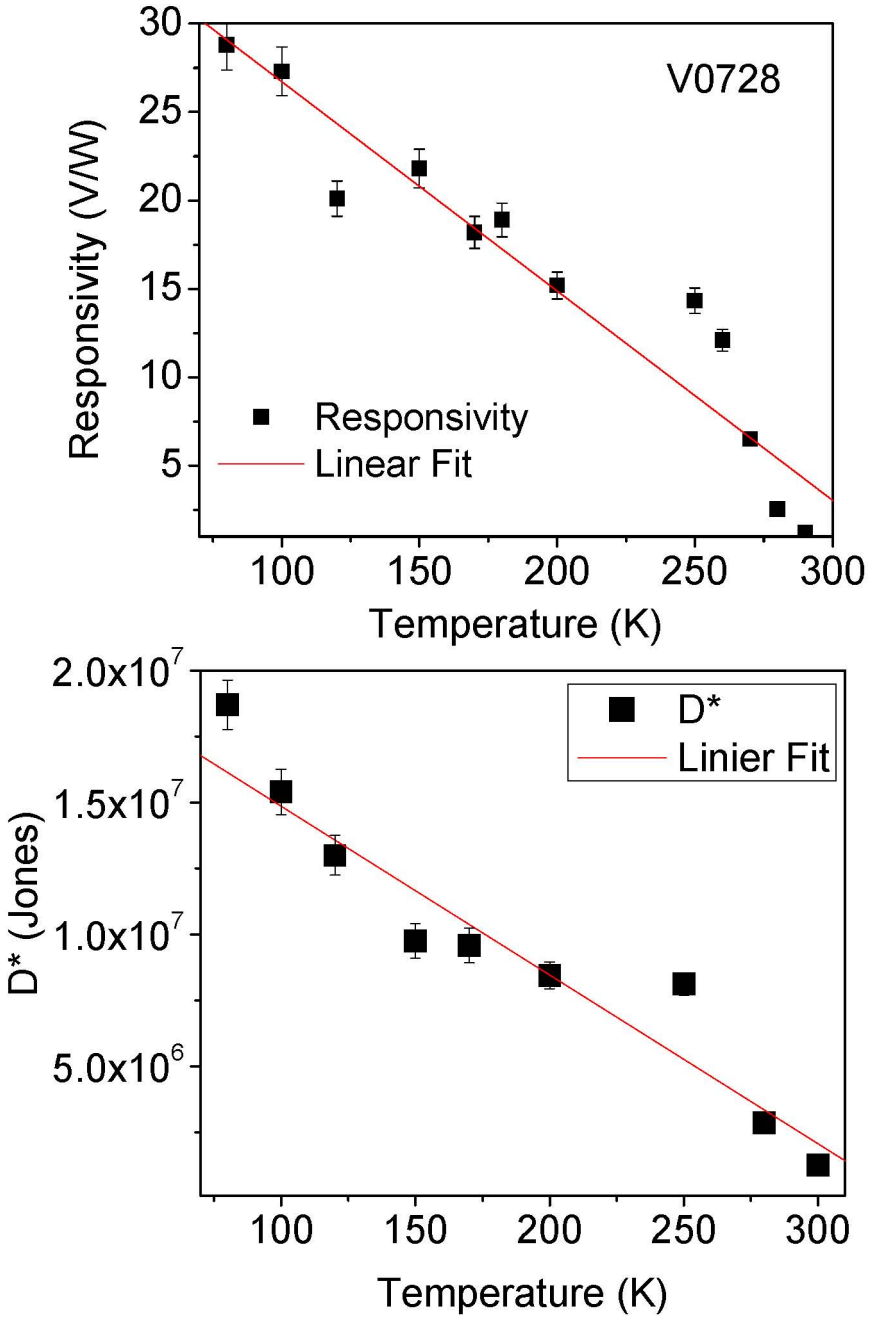

Figure 2-7 The Responsivity (top) and detectivity (bottom) variation at 1.8 μm wavelength of V0728 with different temperatures.

2.3.6 The photovoltaic response at low temperatures.

The variation of photovoltaic responsivity and D* at 1.8 μm wavelength for V0728 as a function of temperatures 80 K to 300 K are shown in Fig. 2-7. The response increases as the temperature decreases, and at 80 K the responsivity is ~ 28 V/W. The change of detectivity (D*) at different temperatures are also shown in Fig. 2-7. The D* reaches ~ 1.8×10^7 Jones at 80 K. Even though a linear fit is shown in the Fig. 2-6, agrees better with the low temperature responsivity, the response in the temperature region 300 K to 250 K shows a rapid increase with decreasing temperature.

Response spectra of V0728 at 120 K and 170 K are shown in Fig. 2-8. As can be seen in the figure, the response threshold shifts towards the long-wavelength region as the device temperature reduces to 120K in V0728. This trend was observed for temperatures below 120 K, and it diminishes as temperature increases, and completely disappears in temperatures greater than 150 K. This red shift in the threshold wave length is only observed in V0727 and V0728 where the aluminum fraction in the graded barrier is higher than other graded barrier devices.

The cause of the red shift in spectrum can be the effect of indirect carrier transitions from the light hole band to split-off band which was observed by Jayaweera et. al. [18] in split-off band detectors. But the cause of temperature dependence is yet to be clearly identified. Additionally, the SP10 series devices with low aluminum fraction in the barrier do not show this red shift in the response because of their long wavelength threshold compared to the V07 devices.

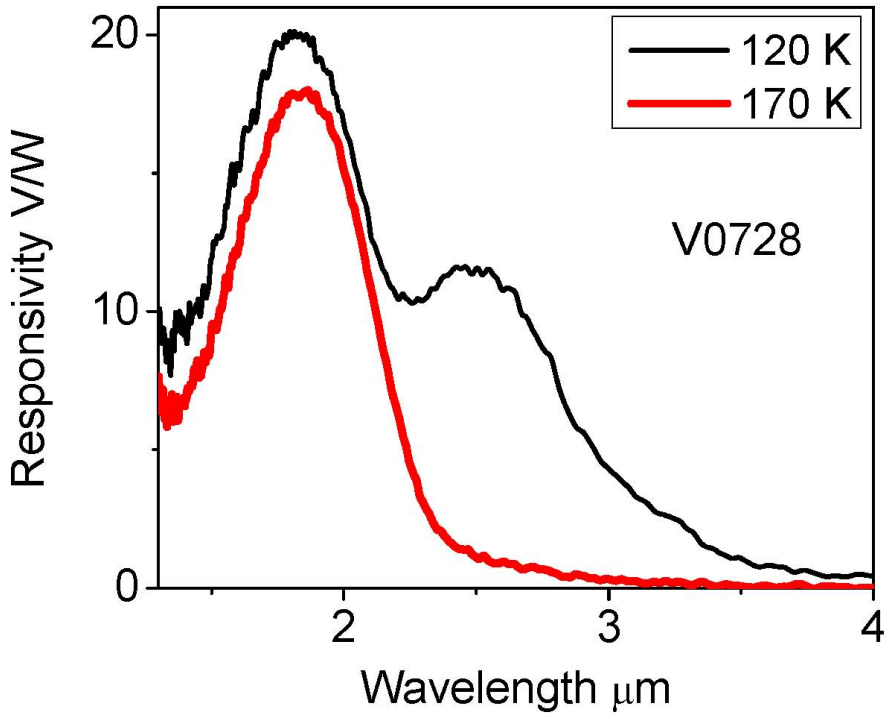

Figure 2-8: The response spectra of V0728 at 120 K and 170K. As the temperature decreases a second response peak arises in the device.

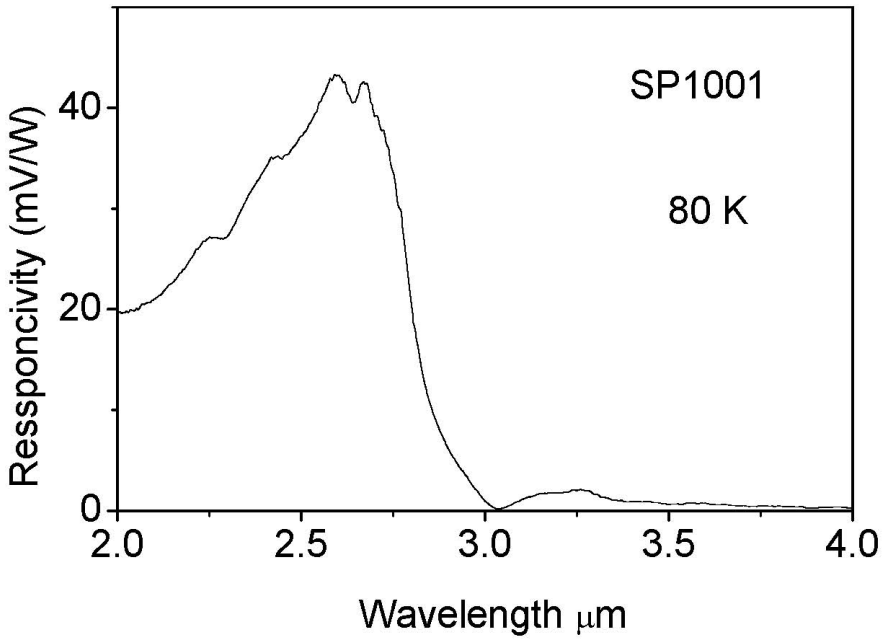

Figure 2-9: The photovoltaic response observed for the constant barrier device (SP1001) at 80K.

Another interesting observation was the photovoltaic response observed in the devices without graded barrier (SP1001) at low temperatures (T < 200 K). The photovoltaic response observed in the SP1001 at 80 K, is shown in Fig. 2-8. A cause for this PV response in SP1001 was not fully understood, but few possible causes are stated below.

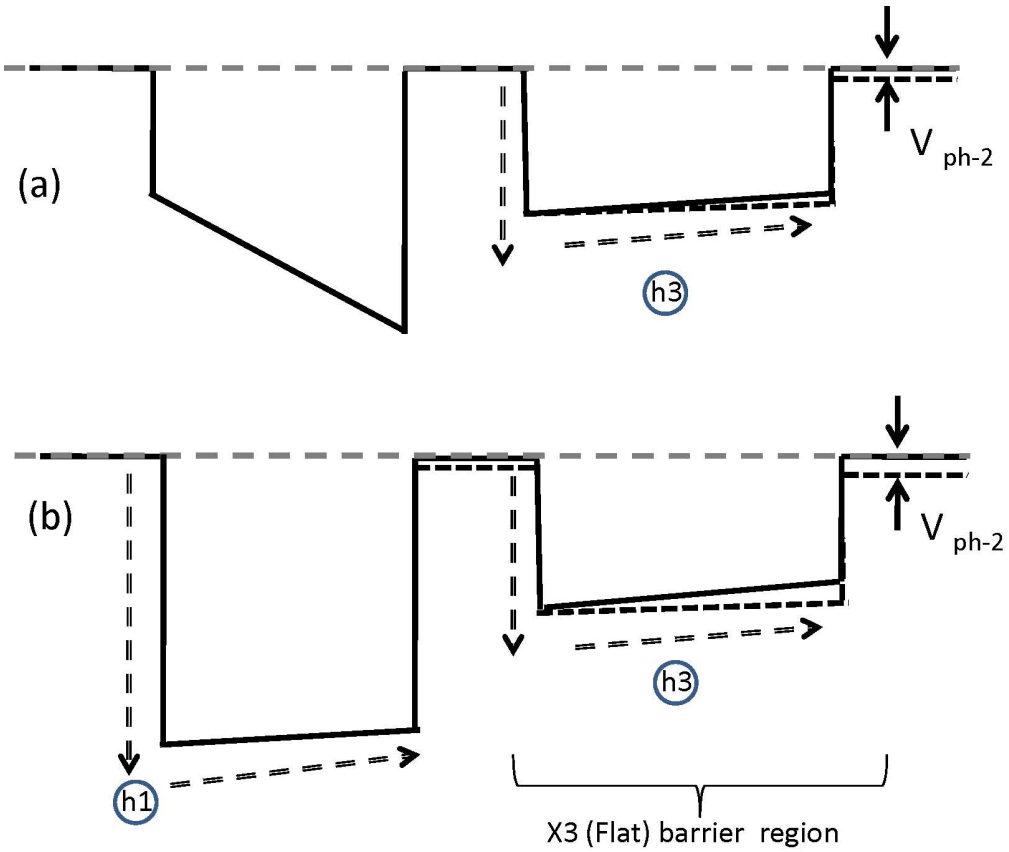

Figure 2-10: (a) The carrier transition mechanism involved in the response threshold red shift in V0728 and (b) the carrier transition mechanism involved in the photovoltaic response in the constant barrier structure (SP1001)

One possible reason for the observation is the thermo-electric effect in the device. As one end of the device is cooled and the other end is illuminated with infrared radiation (heating), there is a possibility of small temperature difference present between the two ends of the device causing a net carrier flow in to one direction. A similar effect was observed by Schneider et. al. [41] for a AlGaAs/ GaAs/AlGaAs single well structure. A possible carrier transition mechanism responsible for the photovoltaic response in the SP1001 at low temperature is shown in Fig. 2-10. Due to the temperature difference at the two ends an energy gradient will emerge in the flat barrier (the X3 barrier) region. The temperature difference causes the band gap of AlGaAs barrier to vary causing a slight gradient in the barrier region. This will disrupt the equilibrium between the carrier transition process h3 and h4 shown in the Fig. 2-2, and there will be a net carrier flow towards the top contact region until the carriers accumulate and shift the valence band energy in the top contact region so that equilibrium is reestablished. This temperature gradient can cause a negative effect on the graded barrier structures' photoresponse as the temperature gradient causes carrier flow in the opposite direction (carriers accumulate at top contact, instead of the bottom contact as shown in Fig. 2-2). But as can be seen in Fig. 2-9 the photoresponse due to this thermal effect is very small (~ 40 mV/W @ 80 K) compared to ~28 V/W responsivity observed in the V0729 at 80 K.

Another possible cause for the low temperature photo-voltaic response in SP1001 is the growth defects. During MBE growth a non-uniform barrier with a slight slant may have been generated. Furthermore, dopant migration can also cause band bending to generate a gradient in the flat barrier region [42]. Additionally experimental and theoretical studies by Larkins et. al. [43] show a photovoltaic response can be generated due to asymmetric interface roughness in the structure.

The photovoltaic response generated in SP1001 due to an energy gradient associated with temperature differences, defects generated during growth or doping migrations is very weak even at low temperature. So, at room temperature this response can resulted in a low signal to noise ratio.

2.3.7 Future Work: Possible improvements in responsivity and detectivity for room temperature operation

Possible modifications and expected improvement factors are summarized in Table 2-4 and are briefly discussed in this section. Based on the results and calculations published elsewhere [44], increasing the emitter doping from 1×10^{19} cm^3 up to 3×10^{19} cm^3, will result in an improvement factor of ~3 is expected by increasing the number of excited carriers. Similarly, from an analysis of the improvement in the responsivity with increasing gradient in the barrier, shown in Fig 2-2 (a) and (b), an improvement by factor of ~3 is expected by lowering the aluminum fractions from X1 = 0.55 to 0.05 at the lower end of the barrier. Lowering the aluminum fraction at the lower end of the graded barrier will allow the VB in the bottom contact to shift further, generating a higher response voltage. With the addition of 30 emitter/barrier layers will improve the photon absorption hence an improvement factor of 25 is expected. Multilayer structure will increase the photon absorption in the device; and more carriers will be excited and accumulated in the contact region. Additionally, multilayer device can act as a series connection of individual units; therefore, increase the response voltage.

Furthermore, keeping the resistance of the device to an optimum value by adjusting the barrier thicknesses to maintain the low noise as well as a high responsivity, will improve the D* by an additional factor of 3 or more making the D* > 10^9 Jones, what would make this device competitive with the reported photovoltaic devices operates under low applied bias voltage [45]. Additionally, as theoretical models have predictions of around 20 times enhancement of absorption via plasmon effects [46, 47] an improvement factor of ~20 can be expected via enhancing the absorption using surface plasmon effects.

The result is a total enhancement of a factor of 10^4. Furthermore, by adopting different materials with higher absorption coefficient (α; at λ ~1 μm, T ~295 K and p-doped) than GaAs (α ~20 cm^{-1}) [48] such as InN (α ~10^3 cm^{-1}) [49] and InP (~200 cm^{-1}) [50] shall enhance the absorption resulting the performance of the device increase by a factor of 10 or more. This offers the prospect of the detectivity to be greater than 10^{11} Jones which is a competitive with commercially available detectors, such as the p-i-n InGaAs detector with D* of the order of 10^{11} Jones.

Table 2-3: Summary of expected enhancement factors due to modifications proposed for the present structure.

Description	***Present Value***	***Proposed Value***	***Expected Improvement Factor in D****
Increase doping	1×10^{19} cm^{-3}	3×10^{19} cm^{-3}	3
Gradient in the barrier (X1-X2)	0.55	0.05	3
Increase Number of layers	1	30	25
Impedance (Johnson Noise)	15 kΩ	2 kΩ	3
Plasmon effect	-	15	15
High absorbing material	GaAs(α ~20 cm^{-1})	InN(α ~10^3 cm^{-1})	50
		InP(α ~200 cm^{-1})	10

2.4 Conclusion

In conclusion, single emitter barrier structures with p-doped GaAs emitters and undoped AlGaAs graded barriers were tested for their photovoltaic (without applied bias) response. We found that structures with a graded barrier had a photovoltaic response at room temperature and without any applied bias voltage. A device with a higher aluminum fraction in the graded barrier (x=1 to 0.55) and with an emitter thickness of 80 nm, showed the highest responsivity of ~ 450 mV/W at 300 K. This responsivity

was shown to increase as temperature is decreased. Furthermore, increasing the emitter region thickness by a factor of four led to an increase in the peak responsivity by a factor of ~ 26. Devices also showed better D* values when operated in a photovoltaic mode rather than in a photoconductive mode. Possibilities of further enhancing the responsivity and detectivity are discussed. Additionally, the concepts presented in this paper can be extended to long wavelength IR radiation in the 8 – 14 μm range, as well as the terahertz frequency range, using phosphide and nitride based materials. Use of a photovoltaic mode of operation thus offers considerable potential advantages for long wavelength detection.

3 PERFORMANCE IMPROVEMENTS OF A SPLIT-OFF BAND DETECTOR WITH A DIGITAL-ALLOYING GRADED BARRIER UNDER PHOTOCONDUCTIVE MODE OPERATION

3.1 Introduction

The development of infrared (IR) detectors operating at or around room temperature would be of great benefit for many practical applications. The reduction or elimination of weight and power requirements for cooling systems will greatly enhance the attractiveness of these detectors. A number of different approaches to improve the operating temperature of IR detectors have been studied, including: bulk HgCdTe operating up to 200 K [51], quantum well [52, 53], quantum dot [54], and type-II strained superlattice [55] detectors. The split-off band detectors were successfully tested recently [18] showing a ~4 μm threshold detector operating up to room temperature. However, the performance of these split-off band detectors was low owing to excessive recapture of excited carriers in the emitters. A model for the response of the split-off band detectors was proposed, suggesting possible improvements in the device design [44].

Split-off band detectors consist of highly p-doped emitters between undoped barriers. The absorption in the emitter excites carriers from the light/heavy hole bands into the split-off band. The excited carriers then escape into the barrier, typically after scattering back into the light/heavy hole band at the emitter-barrier interface, and are collected by an applied electric field. One possible approach to improve the performance of the detectors is to use a graded barrier. The extra kinetic energy of carriers entering over the high-sided barrier should reduce the excess trapping leading to photoconductive gain by a mechanism similar to that in QWIPs [56].

Furthermore, as projected by Matsik et. al [44] a graded barrier with the injection side higher than that the escape side will artificially heat the carriers entering the emitter. Providing a sufficiently large height difference between the two edges of the barrier will allow excited carriers to escape after

scattering, and the trapping rate will be reduced. Additionally, grading will allow the thermal escape from the contact and the emitter to be balanced reducing space charge buildup [44].

There are different approaches to grow graded barriers in GaAs/AlGaAs based devices. One approach is to gradually change the aluminum available in the growth chamber, and the other method is to use GaAs and AlAs layers in alternate order, as in a superlattice structure, with varying thicknesses this arrangement is like a binary number system hence it has been dubbed as digital alloying [57]. Two different digital alloying formulas used in the growth of the graded barriers are described later in section 3.2.2 and 3.2.3.

3.2 Device structures and growth procedure

Five different devices (parameters of these structures are given in Table 3-1) with single emitter sandwiched between two barriers were tested to study the effects of a graded barrier on device performance. The valence band diagram of the devices is similar to that shown in Fig. 2-1 in Chapter 2. Out of five devices, the device 1001 consists of a constant barrier as in Fig. 2-1 (b), and it is used as the control to compare the performance of graded barrier versus the constant barrier. The other four structures consist of graded barriers and can be categorized into three groups depending on the method used in growing the graded barrier. For the device 1007 the graded barrier was fabricated by gradually increasing the aluminum fraction during the growth. In the structures 0905, 0906, 0912 “digital alloying” was used to grow the graded barrier. Two different digital alloying approaches were used have identified as ‘averaging’ and ‘subminiband’. These two digital alloying approaches are briefly described below. The expected aluminum fraction at each barrier and expected barrier heights are shown in Table 3-1, and Table 3-2, respectively.

Table 3-1: Sample parameter and aluminum fractions in the barriers of the detector structures (band diagram shown in Fig.2-1.). All samples have contacts and emitters doped to 1×10^{19} cm^{-3}, 80 nm wide graded barrier, and 400 nm wide constant barrier. Acronyms used for the alloying method used in graded barrier: Dig.-MB: Digital alloying with "subminiband" approach; Dig.-Av: Digital alloying with "averaging" approach; and Non-Dig.: non-digital alloying approach.

Sample	**Alloying Method**	**Emitter** Width (nm)	**Graded Barrier**		**Constant Barrier** Aluminum Fraction (X_3)
			Contact End Aluminum Fraction (X_1)	Emitter End Aluminum Fraction (X_2)	
0905	Dig.-Av	50	0.45	0.75	0.55
0906	Dig.-Av	80	0.45	0.75	0.55
0912	Dig.-MB	50	0.45	0.75	0.55
1007	Non-Dig.	80	0.45	0.75	0.55
1001	Non-Dig.	80	0.45	0.75	0.55

Table 3-2: Expected barrier heights of the detector structures

Sample	**Graded Barrier Heights**		**Constant Barrier height** (E_3) meV
	Contact End (E_1) meV	Emitter End (E_2) meV	
0905	240	380	240
0906	240	380	240
0912	230	390	240
1007	240	380	240
1001	240	380	240

3.2.1 Non-digital alloying approach

The device 1007 is grown with non-digital alloying (n-DA) approach. In n-DA the aluminum fraction is continuously changed by gradually adjusting the aluminum concentration and temperature in the growth chamber to grow the graded barrier.

3.2.2 "Averaging" approach

The digital alloying "averaging" (DA-A) approach was used for devices 0905 and 0906. In this barrier the carriers will only see an average aluminum fraction for several adjacent layers [57], i.e., one monolayer of GaAs and two monolayers of AlAs would affect the carrier like a $Al_{0.67}Ga_{0.33}As$ layer. Rough and partial AlAs/GaAs interfaces will break up any miniband formation, and hence improve the averaging behavior. The formulas used in growth of the DA-A graded barrier structures are as follows. The graded barrier was effectively grown as 31 periods of GaAs and AlAs with thicknesses (0.45+0.01N)L/31 and (0.55−0.01N)L/31 respectively, where N is the number of the period and L is the total thickness of the graded barrier. The final five periods were grown by dividing the layers into four sub periods using the remaining barrier thickness according to the above formula. The original formula has to be disrupted because if the above formula is used continually the thickness of GaAs layers will become thicker than the AlAs layer. Fig. 3-1 shows a schematic of the layer arrangement in the graded barrier with a graphical representation of GaAs and AlAs layer thickness variation using a histogram.

3.2.3 "subminiband" approach

The digital alloying "subminiband" (DA-S) approach, used in the graded barrier growth of 0912, has quantum well energy levels creating a miniband forming a graded barrier. The GaAs/AlAs layer quality needs to be high with good interfaces, so that the carrier wave functions are not localized in a single

well. In DA-S approach 11.3 Å AlAs barriers were used throughout with 12 periods each of 7.5, 5.5, 4.6 and 3.7 Å GaAs wells. In the structure 0912, the highest miniband energy level is calculated to be closer to the barrier height energy of $Al_{0.75}Ga_{0.25}As$. A schematic of the layer structure, change of quantum well widths and carrier transport through the miniband are illustrated in Fig. 3-2.

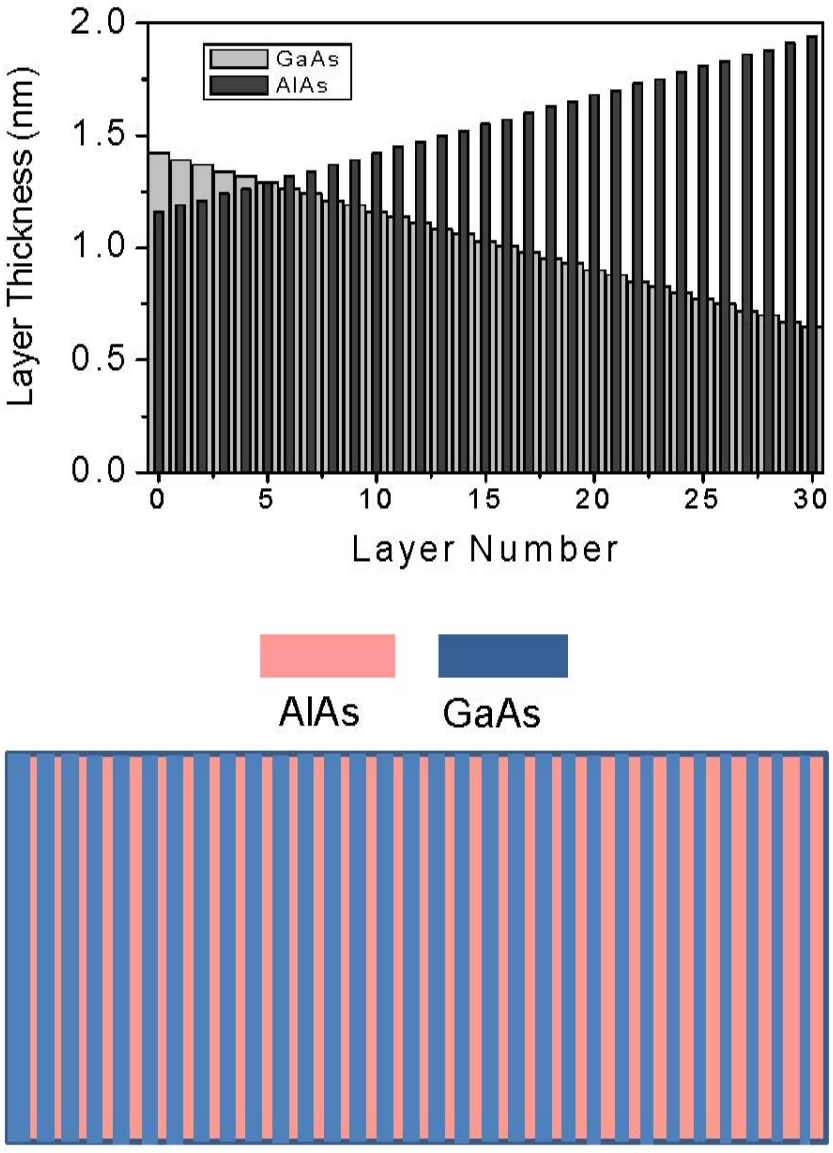

Figure 3-1 Graphical representation of GaAs and AlAs layer thicknesses in “averaging” approach and a schematic of layout in the barrier region.

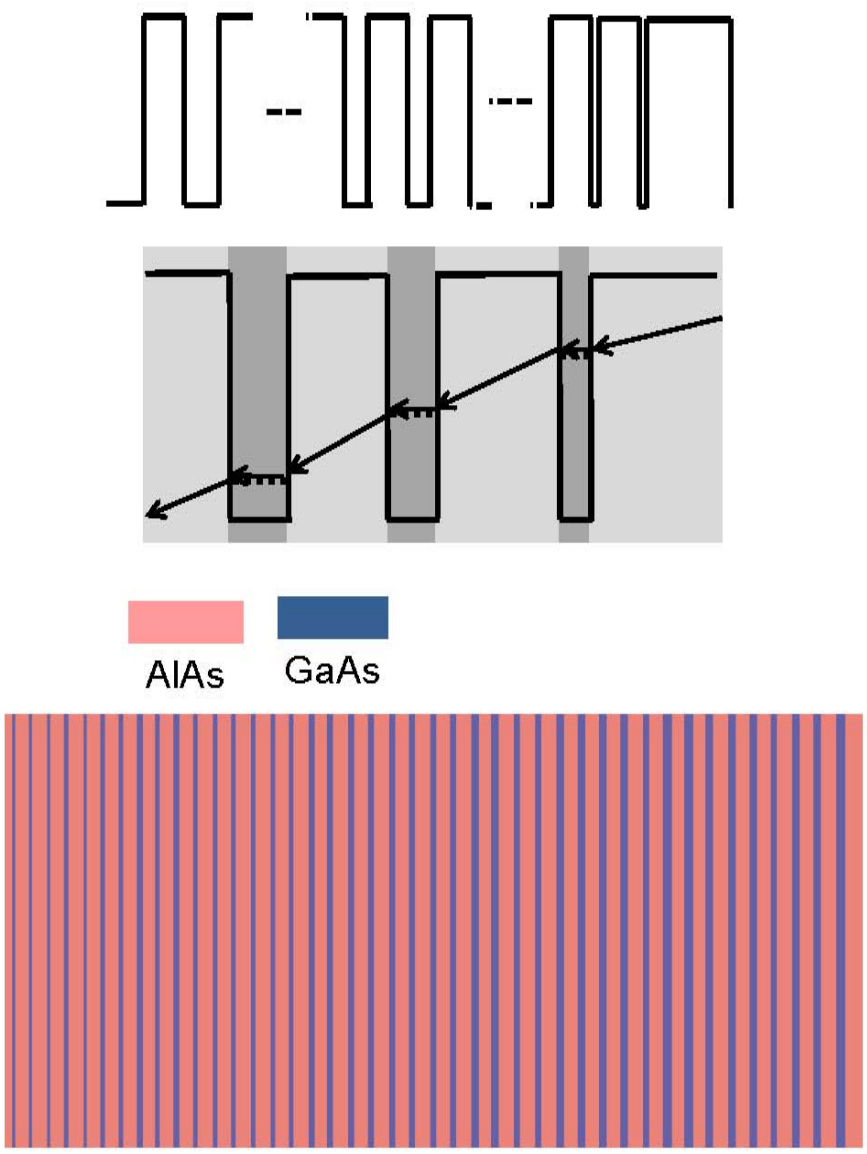

Figure 3-2 Approximate quantum well / barrier arrangement created by the “subminiband” approach with the ground state miniband in the superlattice structure and carrier transported through the ground state miniband and a schematic of the layer arrangement.

3.3 Results

3.3.1 Analysis of digital alloyed graded barrier: "averaging" vs. "subminiband" approaches

This section compares the performance of the two devices grown with the two digital alloying approaches, the 0905 grown by DA-A approach and 0912 grown by DA-S approach. These two structures have same device parameters with a 50 nm emitter.

A tunneling electron microscopy (TEM) image of the graded barrier region for a wafer grown with the DA-A approach is shown in Fig. 3-3(a). A clear layer separation between GaAs and AlAs layers in most of the area in first 26 layers can be seen in the TEM image, but in some sectors we can also observe GaAs layers that breach into the AlAs layers making the layer thicknesses uneven. Furthermore, the final five periods having the thinner layers of the subperiods cannot be seen owing to the resolution limits of the image. The TEM image in Fig. 3-3(b) shows the layer structure at the graded barrier region, where the DA-S approach was used in growth of the graded barrier. A layer separation, between GaAs and AlAs layers is observed in some area in the barrier region, however; the layers appear to almost disappear in some regions and are inconsistent across the entire sample as seen in this TEM.

The IV characteristics of the two devices are shown in Fig.3-4 (a). A higher dark current in 0905 is observed in -1 V bias, and the dark currents in the two devices are very similar to each other at low negative bias (V> -0. 4V) to + 1V bias, even though the dark current in 0912 is high in this range. At higher positive bias 0912 has a lower dark current compared to 0905. The activation energies for the 0905 and 0912 are 270, 320 meV, respectively (Table 3-3). These activation energies are lower than expected from the theoretical values.

The response spectra of 0905 and 0912 are shown in the Fig. 3-4(b), and responsivity values at the peak wavelength of 2.8 μm are given in Table 3-4. The responsivity spectrum of both the devices shows a similar profile with two peaks under negative bias and the one response peak under positive bias. The device 0905 has ~ 2 times higher responsivity compared to the 0912 at both the negative and

positive bias, indicating that the digital alloying DA-A approach is a better method than the DA-S approach.

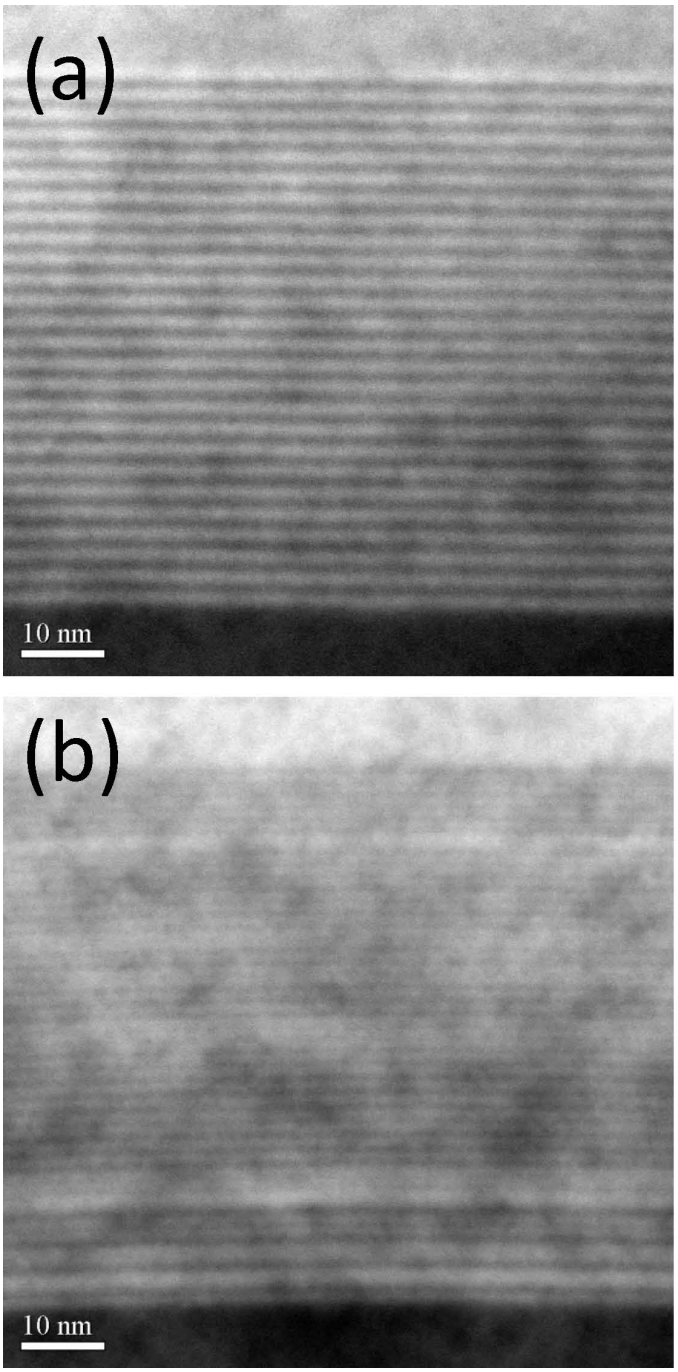

Figure 3-3 : (a) TEM image of the graded barrier showing layer separation in the "averaging" approach. (b) TEM image of the graded barrier showing layer separation in "subminiband" approach.

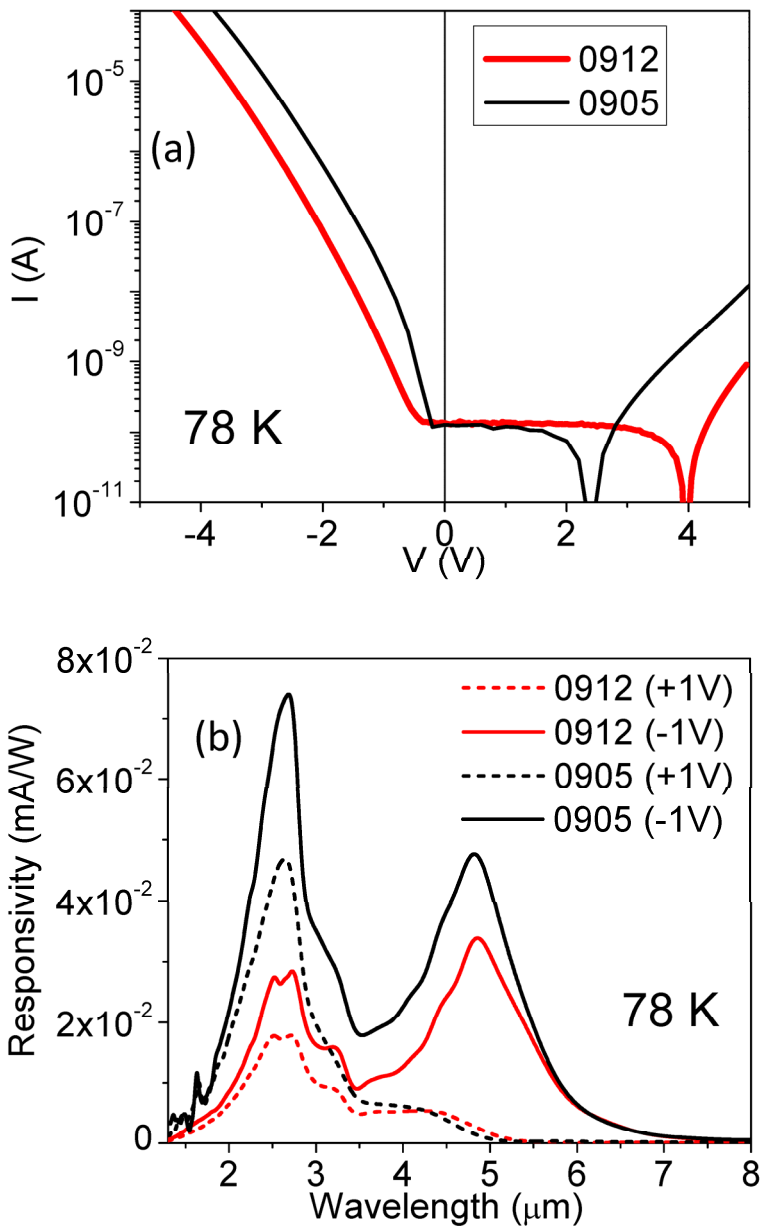

Figure 3-4: (a) The responsivity and IV characteristics of two graded barrier structures grown by "averaging" (0905) and "subminiband" (0912) approaches. (b) The response profile is similar in both structures under positive and negative bias, although the structure 0905 has the highest response.

Table 3-3: The activation energy calculated by Arrhenius plot where the expected value is ~ 390±5 meV for 0905 and 460±10 meV for 0912

Sample	**Activation Energy** meV
0905	270 ± 10
0912	310 ± 10

The Shot noise powers (S(f)) of the devices at 78 K are calculated by Eq.3-1, where, the q and I are electron charge and dark current respectively.

$$S(f) = 4qI \qquad \text{(Eq. 3-1)}$$

The shot noise limited detectivity (D*) is calculated by Eq.3-2, where, the $\mathcal{R}$ and A are responsivity, and electrical area of the device respectively.

$$D^* = \frac{\Re\sqrt{A}}{\sqrt{S(f)}} \qquad \text{(Eq.3-2)}$$

Due to the high dark current in the device 0912 under -1 V bias, the D* of the two devices are altered with the polarity as shown in Table 3-3. The higher activation energy observed for 0912 compared 0905 is the result of low dark current in 0912.

Table 3-4: The shot noise power, responsivity, and D* of the devices 0905 and 0912, grown with two digital alloying approaches, at 78 K under + 1V and -1V bias.

Device	Shot noise (A^2/Hz)		Responsivity (A/W)		Detectivity (D*) (Jones)	
	1V	-1V	1V	-1V	1V	-1V
0905	7.7×10^{-29}	1.2×10^{-26}	4.4×10^{-05}	7.4×10^{-05}	$1.3\times10^{+08}$	$1.8\times10^{+07}$
0912	8.8×10^{-29}	9.4×10^{-28}	1.8×10^{-05}	2.7×10^{-05}	$4.9\times10^{+07}$	$2.3\times10^{+07}$

Due to the layer unevenness, observed in the TEM image (Fig. 3-3 (b)), of the DA-S approach graded barrier the device 0912 may not have performed as well as expected. Therefore, this result does not provide a clear conclusion of whether the DA-A approach or the DA-S approach is better in graded barrier growth. But, in next two sections the performance of the flat barrier device and graded barrier devices with n-DA approach and DA-A approach are presented, showing improvements in responsivity and D* with the implementation of the graded barrier.

3.3.2 Analysis of flat barrier vs. graded barrier (non-digital alloying approach)

This section presents a comparison of the current-voltage (IV), responsivity and detectivity (D*) of graded barrier structure 1007 and the flat barrier structure 1001 at 78 K. Both these devices do not have digital-alloyed barriers, but both have similar dimensions including the emitter thickness at 80 nm. Therefore the only difference between the two structures is that one consists of a graded barrier and the other has a flat barrier.

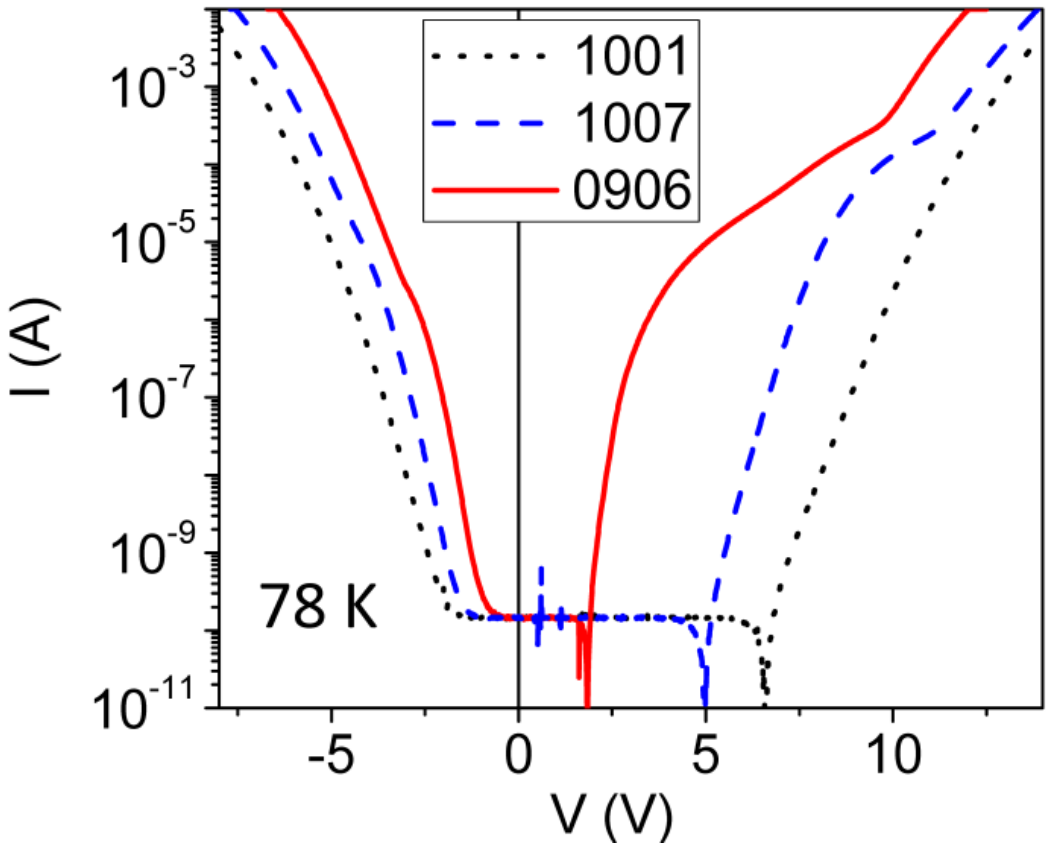

Figure 3-5: IV characteristics of the devices 1001, 1007 and 0906 at 78 K. The asymmetry in the IV curves is due to the asymmetry in the structure. 1001 have the lowest dark current at high negative bias (V < -1V). The device 0906 shows the highest dark current of all three devices.

The I-V characteristics of the two devices at 78 K are shown in Fig. 3-5. The bottom contact is used as the electrical ground. The asymmetry seen at the I-V measurements is due to the asymmetric barriers in the structures. This plot shows increasing dark current in 1007, at large negative and positive bias voltages, compared to 1001. When a large electric field is applied, the effective barrier gradient at the graded barrier will increase, and at the same time the effective barrier width will decrease causing a barrier breakdown. As a result, the 1007 device has its breakdown voltage at a lower bias compared to the 1001. Furthermore, the shoulder like feature in the observed in I-V curve around +10 V bias for 1007 indicates carrier tunneling in the graded barrier device. Carrier tunneling can be prominent in the graded barrier due to the reduced barrier height and the thickness with increasing electric field.

Table 3-5: The activation energy calculated by an Arrhenius plot where the expected value is ~ 390±5 meV for all the devices.

Sample	**Activation Energy** meV
0906	270 ± 10
1007	380 ± 10
1001	470 ± 10

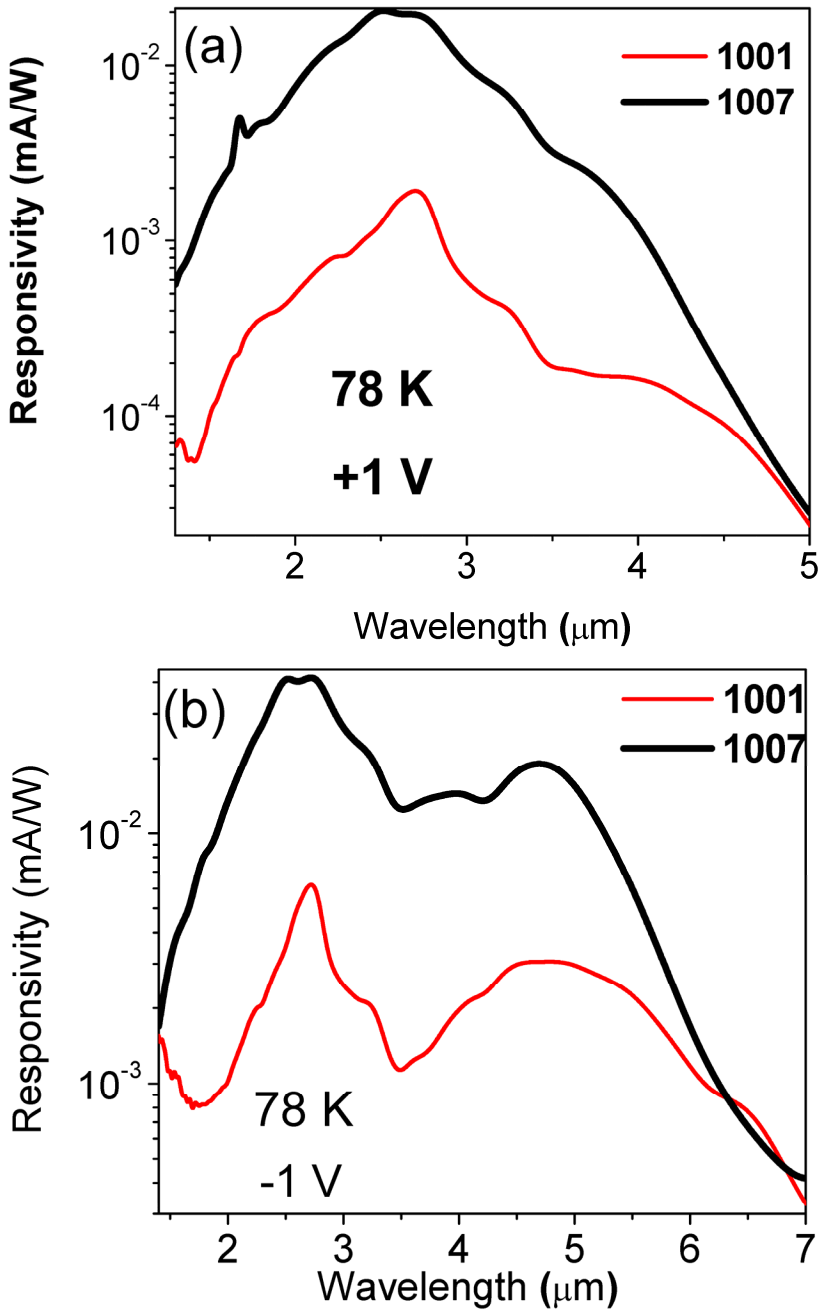

Figure 3-6: The responsivity comparison between two graded barrier structures 1007 and the constant barrier structure 1001 under positive bias (a), and negative bias (b). At positive bias both the devices show a peak response around 2.7 μm, while under negative bias both devices have additional response peaks around 4.9 μm.

The activation energies calculated by an Arrhenius plot are shown in the Table 3-5. The activation energies are approximately 470 and 380 meV for 1001 and 1007, respectively. The n-DA graded barrier structure (1007) has activation energy close to the expected value. The constant barrier structure (1001) has higher activation energy than expected. The reason for the high activation energy observed for 1001 is not fully understood, but it can be due to carrier tunneling in the structure.

The responsivity of 1001 and 1007 at 78 K with +1 V and -1 V bias is shown in Fig.3-6 (a) and Fig.3-6 (b), respectively, and the responsivity values, at the wavelength 2.8 μm, are listed in Table 3-6. Even though activation energies are different in the 1001 and 1007 structures, the response thresholds do not show a significant shift in the two devices except for the ~0.1 μm red shift in the 1007 at positive bias. At negative bias, the threshold wavelengths are similar in both the devices. The 1007 device has a high responsivity of 2×10^{-5} A/W and 4.2×10^{-5} A/W under 1V and -1 V bias, respectively, compared to the 1001, with 1.9×10^{-6} A/W and 6.2×10^{-6} A/W under 1V and -1 V bias, respectively. The device 1007 has a high responsivity compared to the device 1001 under both the negative and positive bias. Comparison of responsivity of 1001 and 1007 indicates that the integration of graded barrier has enhanced the device response.

Under higher applied bias, even though the 1007 device has a high dark current causing the shot-noise to be higher, considering the dark current of 1001 and 1007 in the range from -1 V to + 1V are in the same order of magnitude with 1001 having a slightly lower dark current compare to 1007. Hence, the shot noise level of 1001 and 1007 are approximately of the same order of magnitude as can be seen in Table 3-6. Since the 1007 device has a high responsivity compared to the 1001, the D* is higher in 1007, as shown in Table 3-6.

Table 3-6: The shot noise power calculated by Eq. 3-1, responsivity, and the D* of the devices at 78 K under + 1V and -1V bias.

	Shot noise (A^2/Hz)		Responsivity (A/W)		Detectivity (D*) (Jones)	
	1V	**-1V**	**1V**	**-1V**	**1V**	**-1V**
1001	9.3×10^{-29}	9.3×10^{-29}	1.9×10^{-06}	6.2×10^{-06}	$5.2\times10^{+06}$	$1.7\times10^{+07}$
1007	9.6×10^{-29}	9.6×10^{-29}	2.0×10^{-05}	4.2×10^{-05}	$5.2\times10^{+07}$	$1.1\times10^{+08}$
0906	9.0×10^{-29}	2.0×10^{-28}	4.8×10^{-05}	7.8×10^{-05}	$1.3\times10^{+08}$	$1.4\times10^{+08}$

3.3.3 Analysis of digital alloyed "averaging" vs. non-digital alloying approaches

Even though the analysis in section 3.3.1 shows some defects in the graded barrier growth by the DA-A approach, the device 0906 with the DA-A graded barrier has shown an improved responsivity compared to 1007. Therefore, this section will present a comparison of the performance of the DA-A approach device (0906) and the n-DA approach device (1007), where the only difference in the structure is in the graded barrier growth approach.

As can be seen in I-V characteristics of the 1007 and 0906 in Fig. 3-5, the dark current at 78K is similar in the two devices in the range -0.5 V to 1.4 V. But as the bias increases, the dark current rapidly increases in 0906 compared to 1007. Hence the shot noise in 0906 is higher with a larger negative positive bias in 0906 compared to the 1007 as shown in Table 3-6. The lower breakdown voltages for 0906 indicate higher carrier conductivity in the structure compared to the 1007. The 0906 device also shows tunneling effects in the I-V curve and the tunneling feature occurs at lower voltage compared to the 1007. Additionally, the activation energy calculated for 0906 is ~ 280 meV which is smaller than expected value for the device (390 meV), which may be due to tunneling effects.

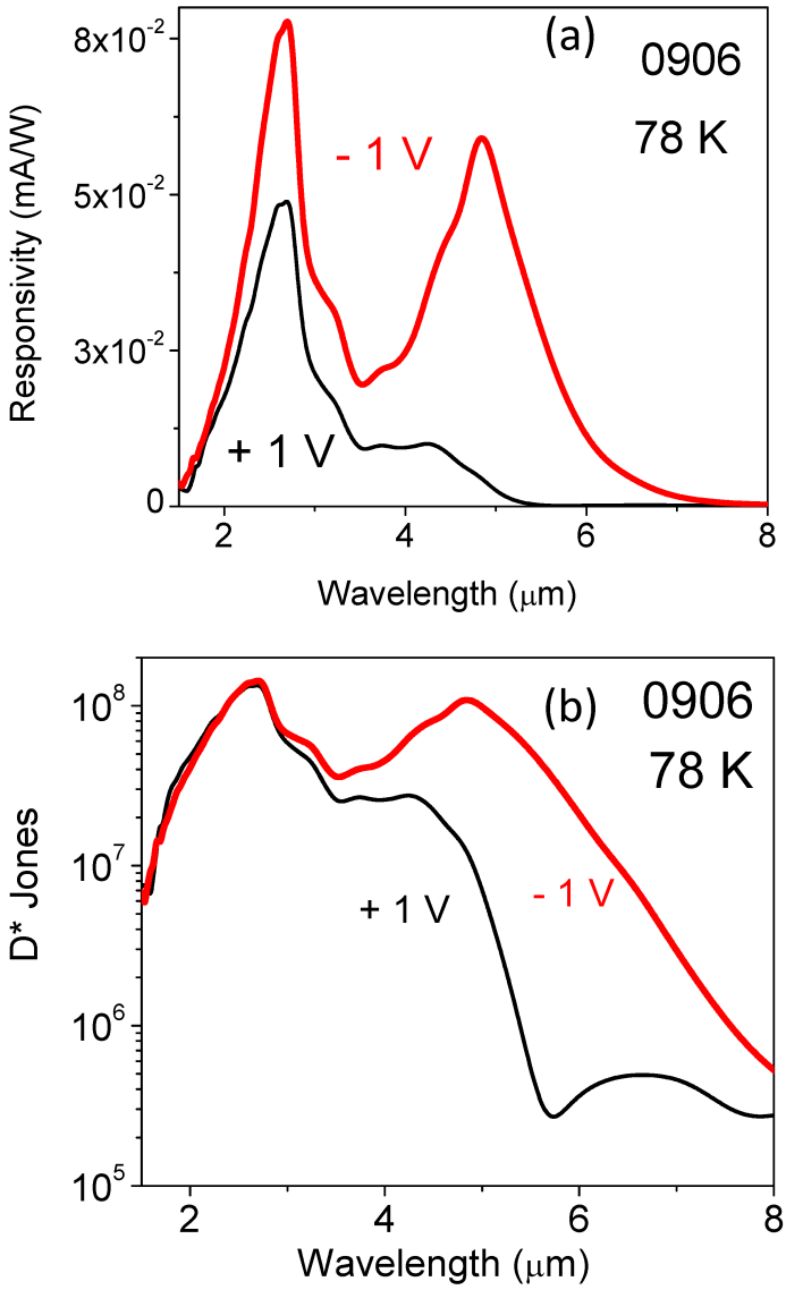

Figure 3-7: (a) Responsivity and (b) detectivity specter of 0906 at 78K, The 0906 gave the highest responsivity among the graded barrier structures.

The responsivity curves of 0906 under -1 V and +1 V bias are shown in Fig. 3-7(a), and the responsivity at 2.8 μm is shown in Table 3-6. The 0906 device has a higher responsivity compared to 1007. In contrast, the 0906 device has the highest responsivity out of all the devices with 7.8×10^{-5} A/W and 4.9×10^{-5} A/W at -1 V and 1V biases, respectively. This is approximately two times improvement compared to 1007 and around ~25 and ~10 times improvement compared to 1001 at the two bias voltages.

The D* of 0906 remains the highest out of all the devices with the values been 1.4×10^{8} Jones and 1.3×10^{8} Jones at -1 V and 1V biases respectively. The D* variation with the wavelength at +1 V and -1 V bias for 0906 are shown in Fig. 3-7(b).

3.3.4 Room temperature performance of the graded barrier devices.

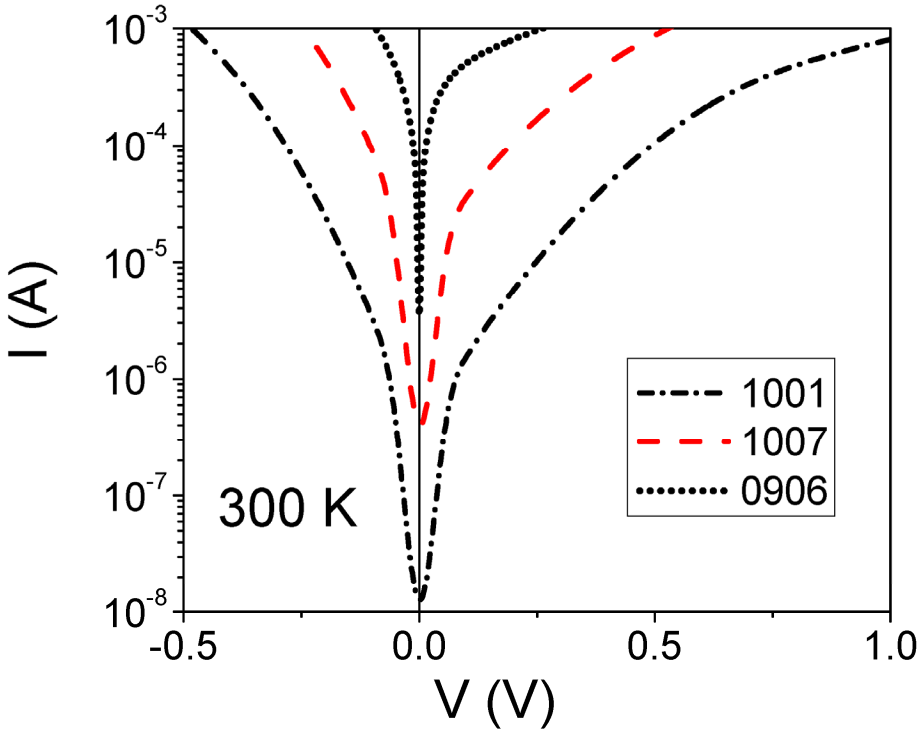

Figure 3-8: IV characteristics of the devices 1001, 1007 and 0906 at 300 K.

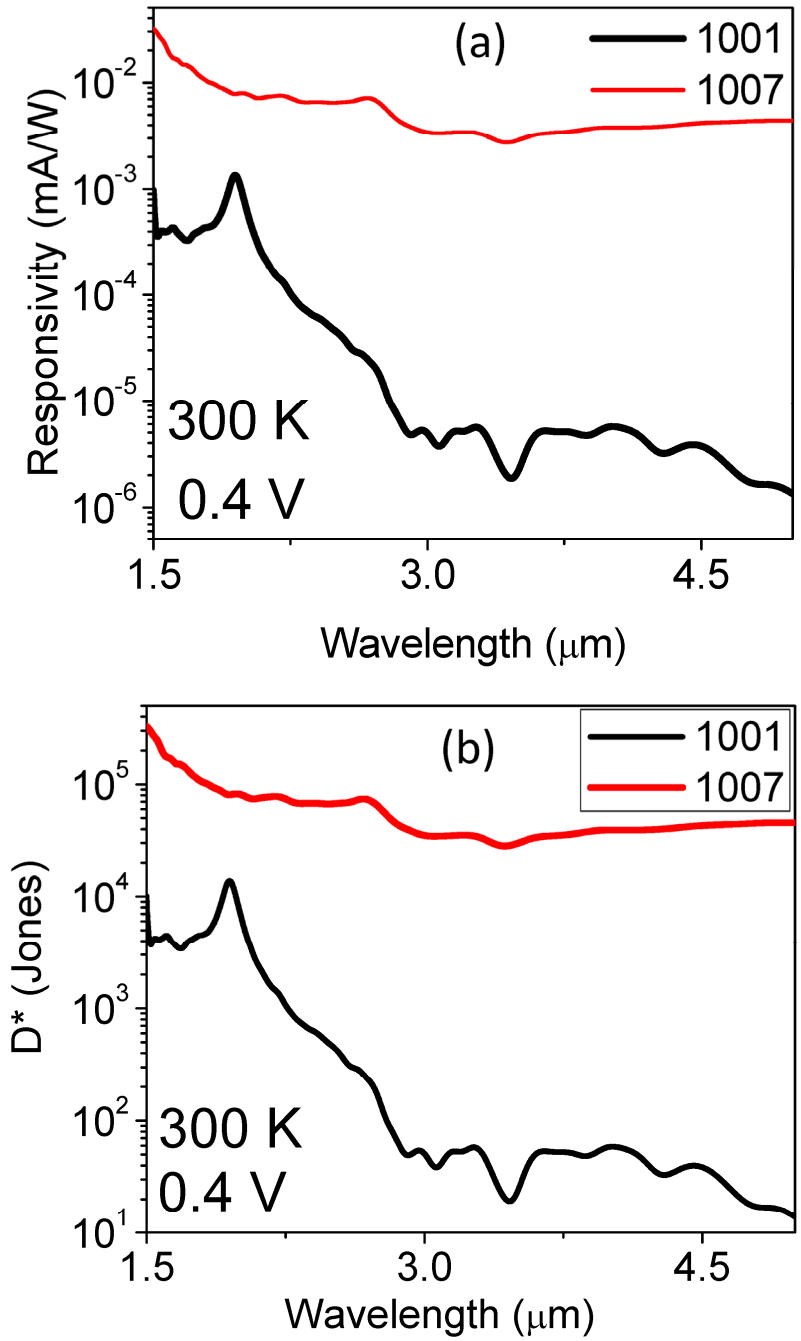

Figure 3-9 (a) The responsivity and (b) detectivity (D*) variation with the wavelength of the 1007 and 1001 at 300 K with +0.4 V bias. The clear response peaks observed at the low temperature has been dilated at 300 K. Additionally the 1001 shows a lower D* compared to 1007.

I-V curves of 0906, 1007 and 1001 at room temperature (300 K) shown in the Fig. 3-8 confirm a very large dark current in 0906 compared to 1007 and 1001, both under positive and negative bias. The asymmetry observed in the I-V curves at 78K (Fig. 3-5) is small at 300K, indicates depletion in thin graded or flat barrier in the device, providing similar current flow in the device under positive and negative bias as only the 400 nm flat barrier is active in each device.

Depletion in the barriers and emitters causes the reduction in photon assisted response in the graded barrier structures. At 300K, the photo response was very weak in 0906 due to very high dark current and the responses of 1007 and 1001 shows a non-zero constant response in spectrum, indicating they have a thermal response. Comparatively low dark current in 1001 and 1007, with respect to the 0906, have resulted in better SNR and show a small photoresponse in wavelengths < 3.5 μm, in addition to the thermal response in the response range. The thermal response observed in GaAs/AlGaAs heteojunction structures are discussed later in Chapter 5. The plot of D* variation with the wavelength for 1001 and 1007 under 0.4 V bias are also shown in Fig. 3-9(b).

3.4 Discussion

3.4.1 Effects on carrier transport in the graded barrier structures

The device response is caused by the split-off and heavy hole/light hole (hh/lh) transitions in p-doped GaAs [17]. The extended wavelength response beyond the barrier height (activation energy) is result of the hh/lh transitions [17]. The two peaks observed in the response spectrum are due to the split-off transitions (wavelength < 3.5 μm) and hh/lh transitions enable the long wavelength response. The response thresholds are shifted due to differences in effective barrier heights encountered by the carriers.

The high photoresponse and long wavelength response threshold observed in the devices at negative bias compared to positive bias can be explained by analyzing the possible carrier transport paths of the devices are shown in Fig. 3-10. As shown in Fig. 3-10(a), under negative bias, carriers will be excited from both the bottom contact (BC) layer and the emitter. Some portion of the carriers excited from the BC will be able to jump over the emitter region without trapping and a second stream of carriers will excite from the emitter resulting high photocurrent at negative bias. And the carriers excited from the emitter only encounters the low barrier resulting in the long wavelength response threshold.

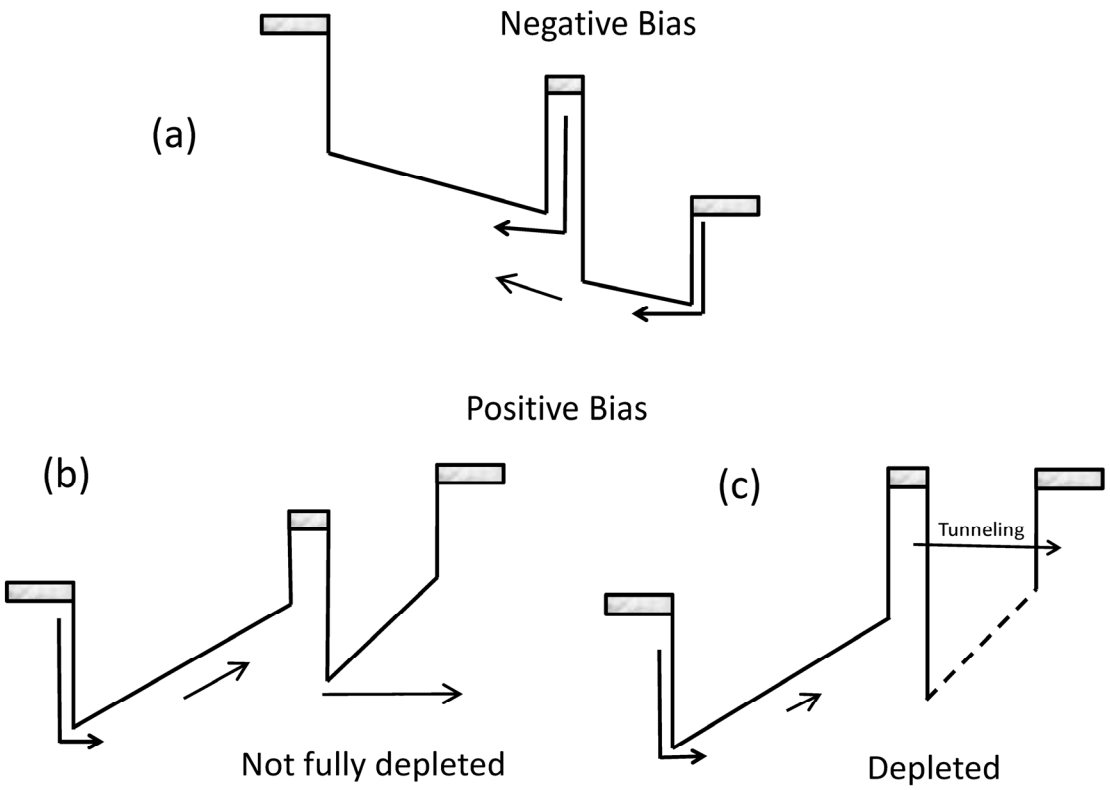

Figure 3-10: Carrier transition process in the graded barrier structures (a) under negative bias shows two excited carrier streams originated from the top contact and emitter, resulting two response peaks. (b) Under positive bias without emitter fully depleted, carriers excited from the emitter will contribute to the device response but the carriers excited from the top contact will be trapped at the emitter. (c) Under positive bias emitter can be fully depleted at high temperatures, hence carriers tunnel through the graded barrier.

Under positive bias, carriers excited from the top contact (TC) will be trapped at the emitter, and only the carriers excited from the emitter will contribute to the photocurrent, hence the photocurrent is low under positive bias compared to the negative bias as seen in the response spectra of all devices. Additionally, these carriers have to overcome the highest barrier edge, resulting in a shorter wavelength response threshold compared to negative bias response.

Depending on the applied bias and temperature, there can be relatively high depletion at the emitters of the graded barrier devices (1007 and 0906) compared to 1001. So the carrier transport across the graded barrier can be affected by tunneling depending on the extent of the depletion as shown in Fig. 3-10(b) and 3-10(c), As a result of the depletion, there can be tunneling through the graded barrier, causing the response to be weak. The response of the devices diminishes at 300K and is effectively observed in the graded barrier structures, implies that at high temperature the emitter is fully depleted specially in 0906. Hence the responsivity of 0906 is very low compared to 1007 at 300 K and cannot be observed. Even at 78 K, the emitter of the 0906 may have been partially depleted but, mat have been not to a significant level to reduce the response to be lower than 1007. This implies the possibility of archiving much higher responsivity via DA_A approach with modifications to reduce the depletion.

3.4.2 Effects of the graded barrier on performance of the devices.

Since the dark current is of the same order for 1001 and 1007 at -1V and 1 V at 78 K, the carrier transport rate should be same in the two devices. This indicates the low recapture of the excited carriers in graded barrier structure have been resulted in the response enhancement. Image charge forces will force the barrier bending and form a peak in barrier height at a distance x_m from the barrier edge given by Eq.3-2, where parameters q - charge, ε - permittivity and E- the electric filed.

$$x_m = \sqrt{\frac{q}{16\pi\varepsilon E}} \qquad \text{Eq.3-2}$$

The value for x_m is ~ 44 nm for 1001, and it is reduced to ~ 24 nm for the graded barriers due to the additional energy gradient in the graded barrier. Therefore, carriers in 1001 have a higher probability of recapture compared to the carriers in graded barrier structures as can be illustrated as in the Fig. 3-11(a) and 3-11 (b). The low recapture due to the graded barrier enables high collection rate, as more carriers will travel to the bottom contact. Furthermore, unlike in the 1007 the quantum wells like formation in the 0906 due to the alternating GaAs/AlAs thin layers in digital alloyed approach can trap photoexcited carriers in the recapture path. And the uneven layer layout of the barrier in the device 0906 can provide escape paths to these trapped carriers towards the contact layer with the assistance of an external electric field (Fig. 3-11 (c)). This can be the cause of the additional improvement achieved in 0906. This implies the digital alloying approach applied in 0906 a good method for graded barrier growth in the devices.

Since the response was enhanced with both the negative and positive bias the suppression of recapture may not be the sole cause of the result. One other possibility is the distribution of the electric fields in the structures. Even though the barrier widths are same in each structure, the 1001 has high effective barrier with 75% aluminum compared to an average 60% aluminum in the graded barriers (both 1007 and 0906). Therefore, the electric field across the h3 barrier can be smaller in 1001 compared to the graded barrier structures. As a result, under positive bias the combined effect of low recapture rate and high refilling of emitter produced a ~ 10 (25) times enhancement in response and in contrast to only ~ 6 (12) times improvement that is observed under negative bias when recapture is not suppressed and only the collection efficiency at top contact is better in the in 1007 (0906) compared to 1001.

The major difficulty in demonstrating the room temperature operation of the present graded barrier device is the high dark current in the structures. The 1007 has demonstrated a low dark current with compared to the 0906 at 300K. This implies a novel approach based on integrating both the “digital alloying” and “non-digital alloying” approach may result in further improvement in the performance of the split-off band inferred detectors operating at room temperature. One possible implementation is to have a low number of periods in the graded barrier DA-A approach, i.e. use a lower number of periods instead of 31 used in present structure, will assist lowering the dark current as AlAs layer thickness increases.

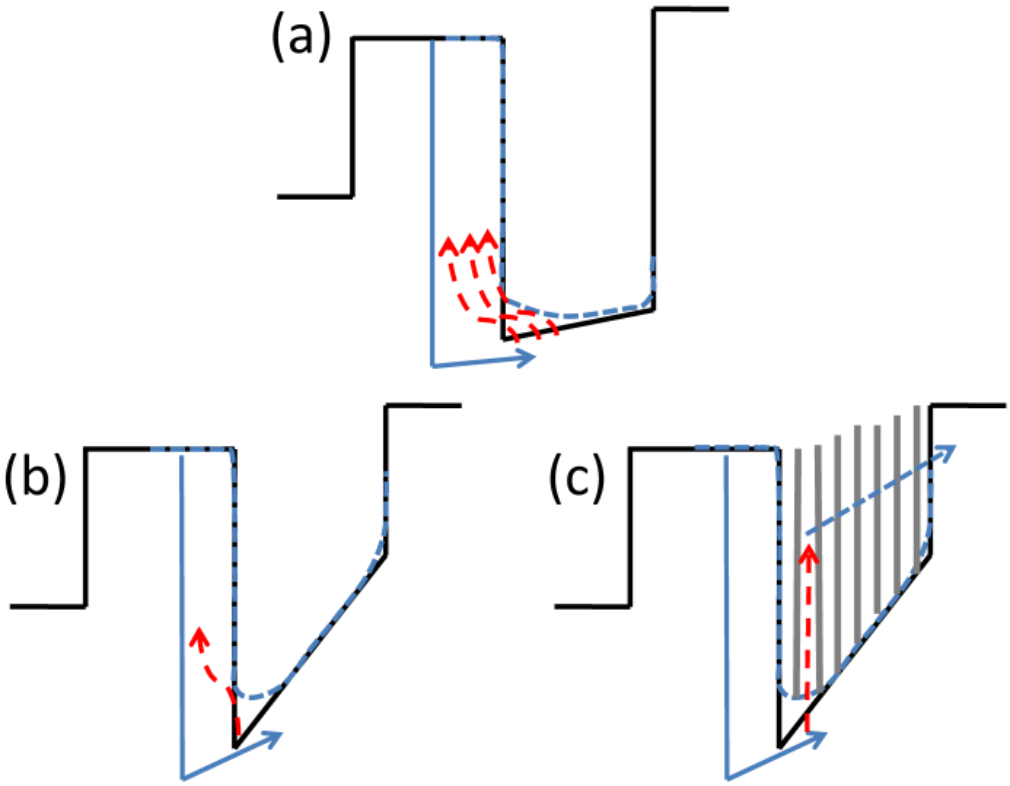

Figure 3-11 The excitation (solid arrow) and recapture (dash arrow) path of carriers in (a) flat barrier structure, (b) graded barriers structure, and (c) digital alloyed graded barriers structure. Due to the high gradient in the graded barrier structure the recapture probability is lower compared to the flat barrier structure, and is further suppressed in the digital alloyed barrier. The dash lines indicate the barrier lowering and barrier bending due to electric field.

3.5 Future work

Further improvements in the device performance can be expected by improving the layer separation in the digital alloying approach which can result in low dark current in the device. In contrast, the tunneling paths can support the responsivity enhancements by improving the collection efficiency as suggested for 0906. Therefore, improved layer quality can reduce the photoexcited carrier collection. So, further studies will need to identify possibilities to compensate each effect to archive optimum enhancement in photocurrent, and D* of the device by improved layer quality in digital alloying.

Additionally having multiple emitter/barrier periods in the structure instead of the single period demonstrated in this chapter will increase the photon absorption causing a increase in the response; furthermore, a multi-period structure can also assist in reducing the dark current and improve the detectivity.

3.6 Conclusion

The graded barrier structures have improved responsivity compared to the structure with constant barrier. Results indicates that response enhancement in the devices with the graded barrier grown by “averaging” approach and is only suited for operation under unidirectional bias to the device. The main effect on compromising bidirectional biased performance is the high Shot noise due to high dark current. Additionally, when the operation temperature is increased the SNR of the graded barrier structures degrade due to increase dark current caused by barrier depletion; therefore, at 300 K the response spectrum of the graded barrier structures with low barriers do not show clear response peaks. Results also indicate introduction of high resistive barriers can retain to improve the SNR of the devices at high temperature operations. Moreover, the single emitter in the tested structures resulted in the low responsivity in the devices under test; hence, implementing multilayer structure will result in increasing the responsivity, and also can result in lowering the dark current, causing a low Shot noise power and will lead to high D* in the devices.

4. NOISE SPECTRA OF UNCOOLED SPLIT-OFF BAND DETECTORS WITH A GRADED BARRIER

4.1 Introduction

Noise in a device resulted due to both internal and external sources have been observed in many optoelectronic devices. External noise is generated by outside sources such as power supply units, amplifiers and antenna effects in connecting wires and leads of the device. Internal noise can be generated by the device's material properties [58] and structure [59-62] . Noise is the primary limitation to, and often significantly degrading the performance of optoelectronic devices. Low noise is thus one of the principal requirements for obtaining a higher detectivity (D*) in infrared photodetectors, making it essential to study and identify the origins of all noise source.

Internal noise is mainly generated by dark currents, temperature fluctuations, and trap states in the structures. Material quality and the device structure could also play a role. When an electrical current passes through a material, fluctuation in the current give rise to Shot noise. Fluctuations in thermal motion of charged particles due to temperature and resistance result in Johnson noise. Scattering and trapping of carriers leads to generation-recombination (G-R) noise in devices, and are mostly observed in photoconductors. G-R noise can increase with the trap density in the material. 1/f noise is the least understood noise source but assumed to be caused by generation-recombination at near band edge traps.

High noise has been reported for AlGaAs based bipolar transistors [63, 64]. This has been attributed to a high volume resistance, combined with a large space charge region, which leads to trapping of carriers, and hence an increase in the G-R noise density. Highly doped emitters can also lead to excess noise owing to traps formed by clustering of impurities [65]. Such effects decrease the gain of optoelectronic devices. On contrast, a study by Williams et. al. [66]shows GaAs/AlGaAs based graded band gap avalanche photodiode to have low noise.

Split-off band detectors based on GaAs/AlGaAs heterostructures are recently demonstrated as an uncooled infrared detector [66]. Implementation of graded barriers have been proposed for p-type split-off band infrared detectors [44] to improve their responsivity and detectivity. However, the noise generated in these devices plays a major role in enhancement of the performance. Therefore, the effects on the devices' noise with implementing of the graded barrier on split-off band detector structures is investigated in this chapter.

4.2 Device structures and Experimental procedure

Two structures, 1001, and 1007 (which were introduced in the chapter 3, and device parameters are shown in the Table 3-1) are used in this chapter to study the noise contributions by graded barrier. In brief, the 1007 has the graded barrier, and the structure 1001 has the flat barrier in the place of the graded barrier. Except for the difference in barriers, these two devices have same structural parameters.

Noise current densities were measured using the Stanford Research System (SR785) dynamic signal analyzer connected through the SR-570 low noise current amplifier on to the sample. Devices are biased using the internal biasing in the SR-570. The capacitance-voltage measurements of the devices were measured using an HP 4284A LCR meter; devices are mounted on the cold finger in the closed cycle refrigerator for temperature variant C-V measurements.

The modeling data was calculated from Eq. 4-1 [64] ,

$$S(f) = \frac{AI^2}{f} + \sum_j \frac{A_j I^2}{\left(1 + \frac{f}{f_j}\right)} + 2qI + \frac{4K_B T}{R} \qquad \text{(Eq. 4-1)}$$

where *A*, and A_j are constants, *I* is the dark current at the given bias voltage, *f* is the frequency, and f_j *i*s the cutoff frequency of each generation-recombination (G-R) noise component. The first term in the equation represent the 1/f noise in the device, and the second term represents the G-R noise components. The last two terms are the shot and Johnson noise of the device, due to the dark current and thermal resistivity fluctuations, respectively. In Eq. 4-1, q is the charge of an electron, k_B is the Boltzmann constant, T is the temperature, and R is the resistance of the device.

The trap energy level was calculated from Eq. 4-2 [64]:

$$E_T = K_B T \, Ln(\frac{2\sigma v N}{\tau}) \qquad \text{(Eq. 4-2)}$$

where E_T is the hole trap level energy (measured to the valence band), σ the capture cross section, *v* the thermal velocity, N the density of states in the majority carrier band, and τ the time constant.

4.2.1 Decomposition of noise components

The measured noise current density, are decomposed to the different noise components as stated by different terms in Eq. 4-1 as illustrated in Fig. 4-1. The calculated curve (Th. Total) is the sum of all four noise components and the constants A, and A_j were selected to match the amplitude of the calculated curve to the measured noise spectrum. The value of f_j is chosen so that the inflection in the measured spectrum is replicated in the calculated curve. It clearly shows that the calculated spectrum lies well within the uncertainty in the experimental results.

4.3 Results

The IV characteristics of the devices at 300 K are shown in Fig. 3-9, in chapter 3. The device 1001 (which has the constant barrier) has the lowest dark current compared to the graded barrier devices. The tunneling and barrier depletion discussed in Chapter 3 have caused the high dark current in graded barrier structures.

The noise power S(f) under -50 mV for the devices 1001 and 1007 are shown in Fig. 4-1(a) and 4-1(b) respectively. The dotted and dashed lines represent the 1/f component and the G-R noise component in each device. The dash-dot and dash-double dot line represents Johnson noise and Shot noise levels respectively. The solid thick curve represents the sum of all noise components as represented by Eq. 4-1. The dip seen at high frequencies in the Fig. 4-1(a) is due to limitation in the signal amplifier at high sensitivity settings, required due to low noise power observed in 1001 compared to 1007. The lowering sensitivity setting in the amplifier makes it difficult to identify the G-R noise component in the 1001 device.

Table 4-1: The Shot and Johnson noise current density levels, and the current density at the plateau of the G-R noise, for 1001 and 1007 at -50 mV bias. The Shot and Johnson noise were calculated using the dark current and device resistance.

Device	**Shot Noise** A^2/Hz	**Johnson Noise** A^2/Hz	**G-R (1) Plateau** A^2/Hz
1001	5.7×10^{-25}	3.6×10^{-25}	2.5×10^{-25}
1007	8.0×10^{-24}	2.2×10^{-24}	7.9×10^{-24}

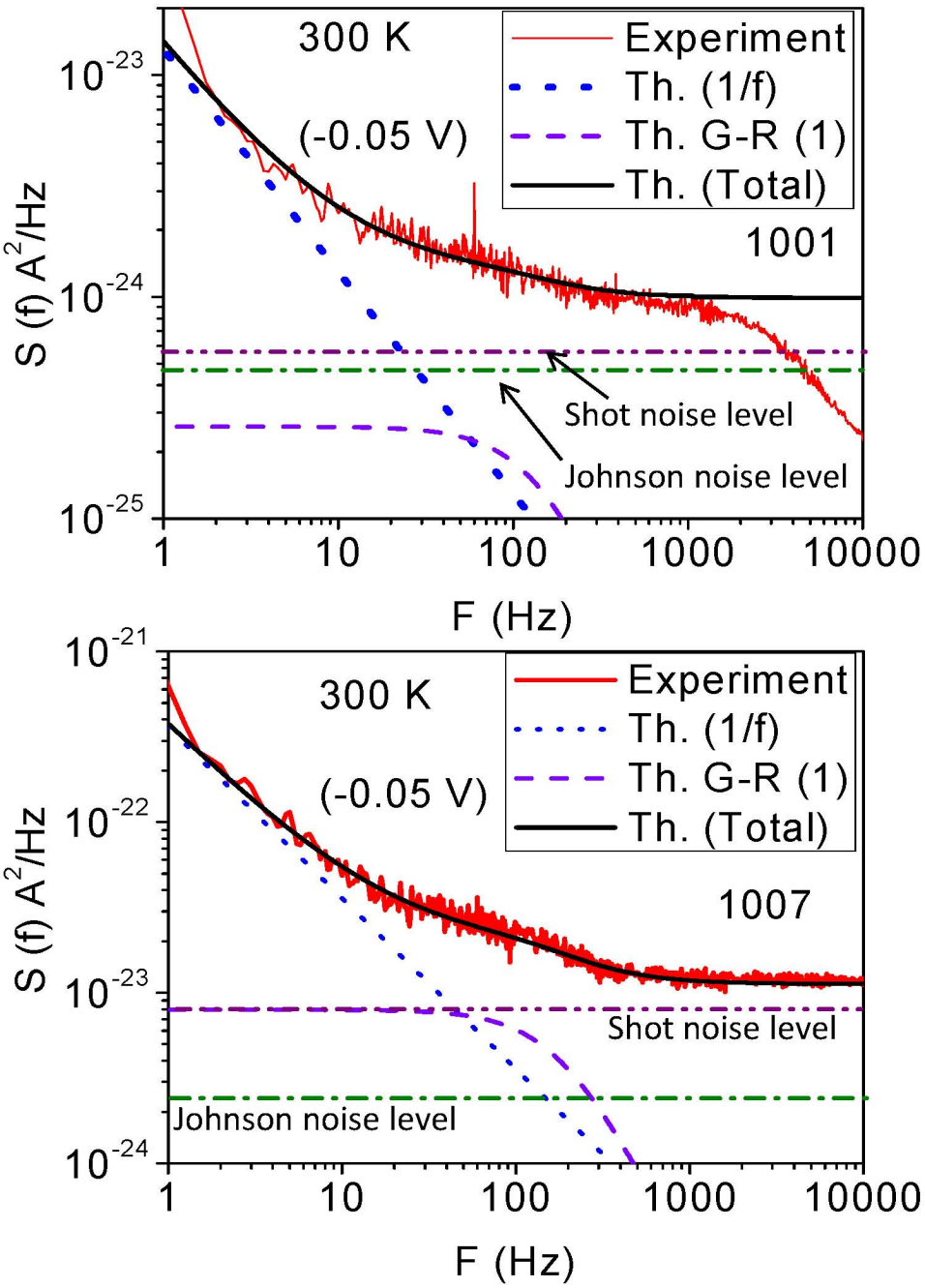

Figure 4-1: The noise power (Sf) of the devices (a) 1001 and (b) 1007 under constant bias of -50mV (Under the negative bias the hole current is from top contact to bottom contact). The dotted and dashed lines represent the 1/f component and the G-R noise component in each device. The dash-dot and dash-double dot line represents Johnson noise and Shot noise levels respectively. The total noise of the in each device (solid curve) decomposed according to Eq. 4-1.

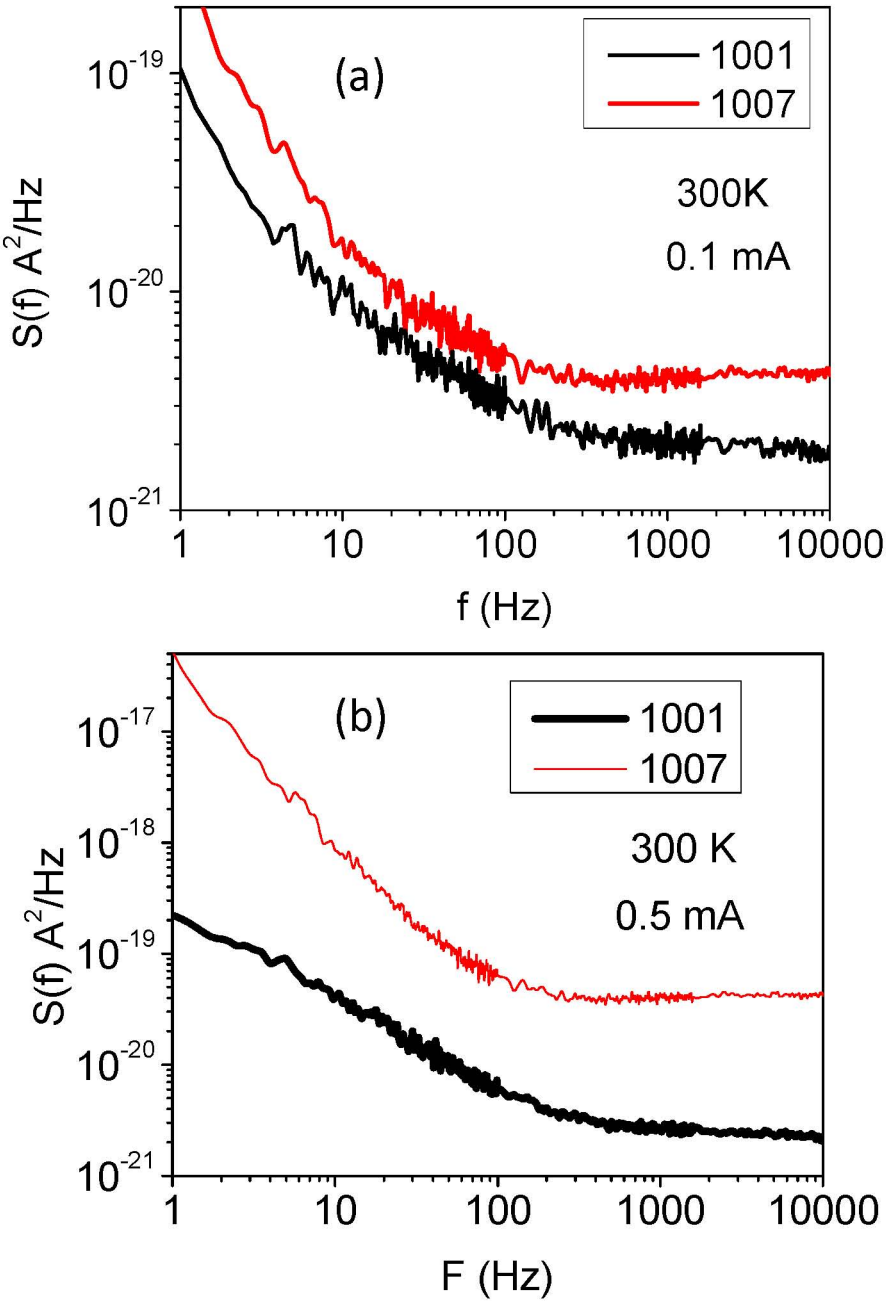

Figure 4-2: The noise power (S_f) of the devices under constant current flow of 0.1 mA and 0.5 mA for the devices 1001 and 1007. The difference in Johnson noise in the two devices is the cause of the shift observed at high frequencies, and this difference increase with the dark current, due to difference in change of dynamic resistance at different biases.

When a same bias voltage is applied across each device, they have different dark current flows due to the differences in device resistance. Hence, a noise measurement with equal dark current in the two devices will remain the shot noise in the two device same, hence allow a comparison of the Johnson noise variation at high frequencies. The noise power, S(f), under same current flow of 0.1 mA and 0.5 mA in 1001 and 1007 are shown in Fig. 4-2. As seen in the figure, the noise levels at high frequency are different in two devices due to the Johnson noise caused by the difference in the dynamic resistance at different bias voltages applied to archive constant current. It would have been interesting to observe the noise spectra with both the dark current and dynamic resistance are same in two devices, but unfortunately such a intersection point was not identified in the IV data.

4.3.1 Trap level energies in the structures

The capacitance-voltage (C-V) trace of devices shows a hysteresis in the capacitance, confirming the existence of a trap level in all structures. The C-V scan for 1001 is shown in Fig. 4-3. Four hysteresis loops (A, B, C, and D) were observed, and the hysteresis can be explained by the following mechanism. At zero bias the trap states will be empty and the Fermi level will lie below the traps. When sweeping the bias voltage, the Fermi level will sweep above the trap states and the trap states will be filled, hence changing the capacitance. When sweeping the bias voltage down, the Fermi level will fall below the trap state but, to empty the filled traps, a much higher voltage difference is required. Therefore, the step in the capacitance will occur at a different voltage, resulting is hysteresis in the C-V sweep.

An Arrhenius plot of the time constant from the C-V sweeps, shown in the inset of Fig. 4-3, reveals trap energy levels at 0.53 ± 0.01 eV and 0.39 ± 0.02 eV, confirming the trap levels observed in the noise spectra. Additional trap levels were also observed for other devices at 0.5 ± 0.02 eV, 0.22 ± 0.04 eV, 0.18 ± 0.03 eV and 0.14 ± 0.02 eV. The trap levels at 0.14 eV and 0.18 eV are likely to be the levels reported as H1 traps [67, 68] (0.14 eV) for AlGaAs films. The trap level at 0.5 eV could be either the trap

level in GaAs at 0.54 eV, the H4 trap level [67] in AlGaAs at 0.46 eV, or a collective effect of these two states. Similarly, two reported trap states can be assigned to the observed trap at 0.22 eV – these are two hole traps: the H1 trap level (0.14 eV), and the H3 trap level [69]at 0.3 eV of beryllium doped AlGaAs. These observed trap levels, and the corresponding trap levels reported in the literature with possible cause for the traps according to literature are summarized in Table 4-2.

Table 4-2 : List of observed trap energy levels, associated trap energy levels and the probable origins of the trap states as reported in literature.

Trap Energy (eV)	Traps reported in Literature (close to observed traps)		
	Material	Energy Level (eV)	Origin of the Trap according to literature
0.53	AlGaAs	0.55	Cu[69]
	GaAs	0.54	Unknown [65]
	GaAs	0.52	Fe[70]
0.5	AlGaAs	0.46	Unknown [67]
	GaAs	0.44	Cu[70]
0.39	AlGaAs	0.4	Unknown [67, 68]
0.22	AlGaAs	0.3	Unknown [69]
	GaAs	0.29	Ga vacancy [69]
0.14	GaAs	0.14	Unknown [67]

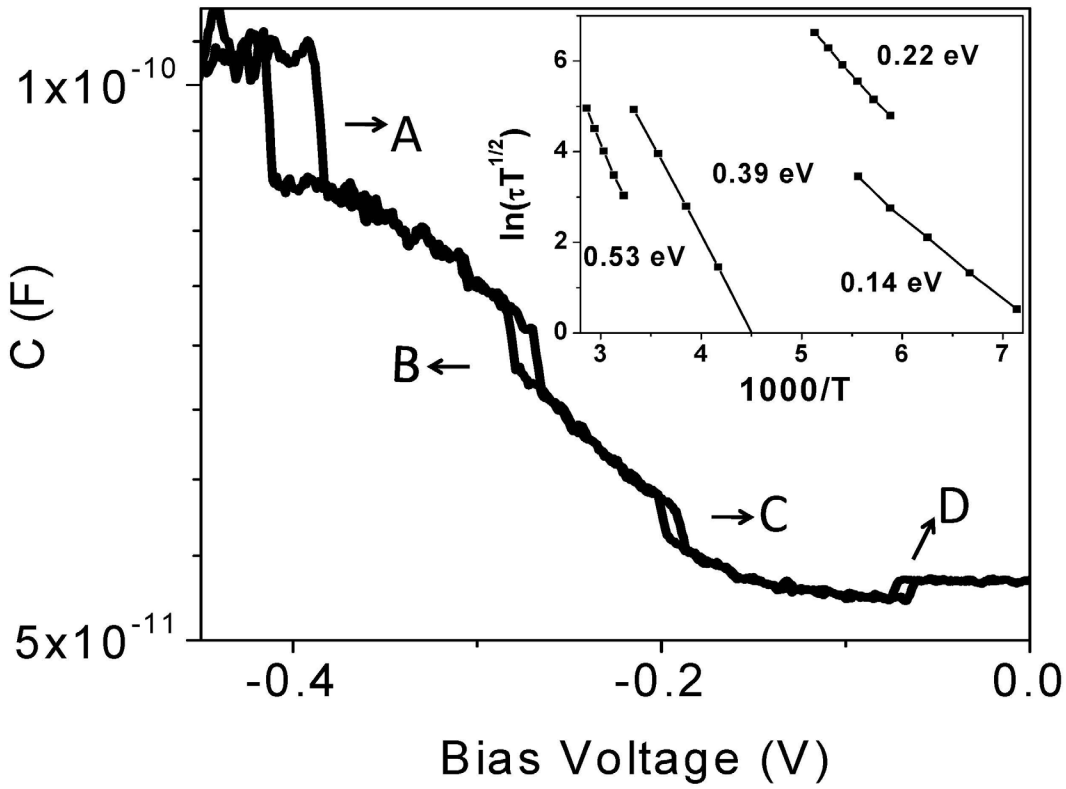

Figure 4-3: The C-V scan for SP1001. All the devices show a similar hysteresis in the capacitance, due to the existence of a trap in the materials. Four hysteresis loops (A, B, C, and D) were observed, and assumed to be result of different trap levels. Inset: The Arrhenius plot of time constant vs 1/T for a selection of devices. The Arrhenius plot reveals trap energy levels at 0.53 ± 0.01 eV, 0.36 ± 0.02 eV, 0.22 ± 0.04 eV and 0.14 ± 0.02 eV.

4.4 Discussion

4.4.1 1/f noise,

In 1001, 1/f noise dominates in low frequency range up to ~20 Hz, but in the 1007 1/f noise domination extends up to ~ 30 Hz. The α factor in $1/f^{\alpha}$ laid around 1±0.1 for both the devices at -50 mV bias. As the applied bias increase, α varies from 0.8 to 1.5 under both negative and positive bias. The α

increases rapidly in 1001 compared to the 1007 imply the 1/f noise is more susceptible in graded barrier devices.

4.4.2 G-R noise

The G-R noise component (G-R (1)) is vaguely appearing in the range from ~ 30 Hz to ~500 Hz. G-R noise component lays below the Shot and Johnson noise levels in 1001. Even for the 1007 the G-R component does not dominate the Shot noise level; therefore, the G-R component is not clearly visible in the noise spectra. But with identifying the Lorentzian components in the S(f) data[59], a G-R noise peak with characteristic frequency at 50 ± 10 Hz have been identified, which gives a time constant of ~ 3.2 ± 0.7 ms. This frequency corresponds to a trap level at 0.54 ± 0.01eV above the valence band (VB), which is in the range of the reported hole trap levels at 0.54 eV, for both beryllium doped and undoped films of GaAs [71, 72].

A weak, second G-R component (G-R (2)) have been identified in SP1007, with a characteristic frequency of 16.5 ± 1.5 kHz, corresponding to a trap level at 0.390 ± 0.005 eV above the valence band (VB). A clear cutoff frequency is not clearly visible in the measured noise spectrum or through the Lorentzian components, but a second G-R noise component has to be added to the calculated noise spectrum to have a good agreement with the experimental spectrum. The energy correspond to the G-R (2) agrees with the hole trap level reported in the literature at 0.4 eV for beryllium doped AlGaAs films [67, 68]. This implies possible dopants migration into the barrier layers from the highly doped emitters. The reason for the G-R (2) component to be very weak can be the low doping migration in the device. The C-V data confirms the existence of traps at 0.39 eV and 0.53 eV which closely agrees with the G-R noise observed in the devices.

4.4.3 Shot noise and Johnson noise

As expected by the observed high dark current and the change of the device dynamic resistance the Shot and Johnson noise in the flat barrier structure is lower than the respective noise levels in the graded barrier structures. The S(f) measured under the same dark current flowing in each device shows a difference in the S(f) level at high frequencies, where Johnson noise is different as the device resistances are different at each bias voltage applied across each device to generate 0.1 mA and 0.5 mA dark current.

4.4.4 Effects from the device structure

The average aluminum percentage in the X_1-X_2 barrier, 1001 has a larger percentage of aluminum compared to the 1007, which have graded barrier (average Al% ~ 60%); this give higher resistance in 1001 supporting the experimental observation of low shot and Johnson noise levels. The low average aluminum fraction SP08 series in compared to the SP1001 caused the higher dark current; therefore, the Shot and Johnson noise levels are lower in the SP1001.

Considering the plateau level of G-R (1) noise components, lowest G-R noise level is present in the structure with the constant barrier (1001) compared to the graded barrier device (1007). There are few possible reasons for this observation, a higher density of traps may be generated at the graded barrier in 1007 due to higher doping migration into the graded barriers with the material properties at the low barrier edge in graded barrier devices are much closer to the neighboring GaAs layer compared to the barrier with high aluminum fraction in flat barrier device. Another factor is, there can be a large variation in trap states in beryllium doped GaAs layer as a variation in hole trap densities from 8×10^{12} cm^{-3} to 1.6×10^{14} cm^{-3} have been observed in beryllium doped GaAs [73] . Furthermore, there can be defects generating in the barrier during the growth as the aluminum fraction and the chamber temperature is continuously changing in the graded barrier growth.

4.5 Conclusion

The noise levels in AlGaAs/GaAs/AlGaAs structures with a one barrier been graded were tested for noise. Under constant bias voltage applied across devices, or under constant current flow in the devices the lowest noise density spectrum is seen by the flat barriers device. It can be conclude that the main cause of the noise in the device is the shot noise and the Johnson noise due to the dark current and temperature variations respectively.

All the devices displayed two G-R noise components, caused trap states in the GaAs emitter and AlGaAs barrier. And more than one trap level identified in the devices through C-V measurements. In addition to the shot noise and Johnson noise, 1/f noise dominates in the low frequency domain. And the as the bias increases the 1/f noise becomes $1/f^2$ noise. The lowest noise levels in all devices are at frequencies higher than 500 Hz.

5. p-DOPED GaAs/AlGaAs HETEROJUNCTION SUPPERLATTICE STRUCTURE WITH HIGH TEMPERATURE COEFFICIENT OF RESISTANCE (TCR) AS A THERMAL DETECTOR

5.1 Introduction

A wide variety of thermal and photon techniques have been tested to detect IR radiation. Among them thermal detectors utilize the temperature-dependent properties of the detector material [10]. As an example, devices such as thermocouples and thermopiles use the thermoelectric effect; bolometers and microbolometers [74] response to changes in resistance; Golay cells [13] use the thermal expansion; and pyroelectric detectors [75] utilize the temperature dependent spontaneous electric polarization that generates electric charges upon incidence IR irradiation (known as pyroelectric effect). Bolometers utilize changes in the absorber temperature when irradiated with electromagnetic radiation. Change in temperature is usually measured as a resistance change in the semiconducting material. The change in the relative resistance per one degree of Kelvin (K) is defined as the temperature coefficient of resistance (TCR, β), and is the key parameter in determining the performance of the material.

The TCR (β) is defined as follows, where *R* denotes the resistance and *T* denotes the temperature. Additionally, *R* is proportional to the carrier concentration (*N*) hence; TCR is also proportional to carrier concentration.

$$\beta = \frac{1}{R}\left(\frac{\partial R}{\partial T}\right) \approx -\frac{1}{N}\left(\frac{\partial N}{\partial T}\right) \qquad \text{(Eq. 5-1)}$$

The maximum change in resistance for each degree of temperature difference and low noise characteristics are desirable to obtain the highest sensitivity in a thermal detector. Materials such as vanadium oxide (VO_x) or amorphous silicon (α-Si) were utilized in presently established bolometers. The main drawbacks of thermal detectors (bolometers) compared to other photon detectors are slow response time and high noise (such as 1/f noise, Johnson noise, thermal and background fluctuation

noise[76]) and low TCR values. With the advancement in micro-machining techniques, miniature micro-bolometer structures have been developed and often used in uncooled thermal cameras. Although VO_x has a good bolometer performance with TCR ~2% K^{-1}, this exotic material is not well suited for large-scale CMOS production, due to the high temperature process used in fabricating VOx for post-CMOS processes. On the other hand, amorphous Silicon (α-Si) exhibits better TCR (~2.8% K^{-1}) compared to VO_x and, Germanium Silicon alloy micro-bolometers have the best TCR around 5% K^{-1}. This paper presents a GaAs/AlGaAs heterostructure with TCR values higher compared to existing VO_x or α-Si bolometers and close to micro-bolometers of Ge/Si alloy. A properly optimized GaAs/AlGaAs heterostructure would be a competitive candidate**,** as a micro-bolometer with high detectivity due to the high TCR, especially compared to existing bolometers fabricated using VOx or Si. Results presented in this chapter show a competitive TCR value of 4% K^{-1} with detectivity (D*) 1.7×10^6 Jones for a 400×400 μm^2 pixel.

Table 5-1: List of detector structures used in TCR calculations and brief description of their parameters

Sample	Al %	Doping Density (p/n)	No. of layers in super lattice
HE0204	12	1×10^{18} (p)	12
HE0205	12	3×10^{17} (p)	12
HE0206	12	1×10^{17} (p)	12
1329	12	4×10^{17} (n)	12
SP001	28	3×10^{18} (p)	30
SP002	37	3×10^{18} (p)	30
SP003	57	3×10^{18} (p)	30

5.2 Experimental procedure

Samples considered in this study are multilayer heterojunction (HEJ) structures based on doped GaAs emitters and undoped AlGaAs barriers. The dependency of the TCR on several different detector parameters such as doping density and Al fraction are investigated. A summary of parameters of these device structures are shown in Table 5-1. These detector structures were measured for their current-voltage-temperature (IVT) characteristics with the variation of temperature and voltage in small steps.

Although there are thin layers of emitter/barrier regions sandwiched in these HEJ superlattice structures they will not form any discrete quantum states inside the barrier/emitter/barrier layers due to their thickness. These emitters are doped high enough to have a scattering length similar to the emitter thickness. The result is a bound 3D carrier distribution in the emitter region. The structures were grown on semi-insulating GaAs substrates and were processed by wet etching to form square pixels with $400 \times 400\ \mu m^2$ in area. Ti/Pt/Au was evaporated on to the top and bottom contact layers. All the sample structures are prepared by the same procedure.

A sample pixel from the structure SP003 was suspended in midair at the center of a regular sample holder using gold wire was measured for the bolometric response. Two of such samples were measured, and both of them have shown a similar response.

The IVT characteristics of each structure were measured using a KEITHLEY 2400 source meter, after mounting them on a cold finger of a closed cycle refrigerator. The temperature was controlled by a Lake Shore 300 temperature controller system. The noise current density of the device was measured using a Stanford Research SR785 Fourier Transform dynamic signal analyzer coupled with a low noise current amplifier, Stanford Research SR570. The IR response of the device was measured using a Perkin-Elmer 2000 FTIR system.

5.3 Results and Discussion

Initially, three structures (HE0206, HE0205 and HE0204) were used to study the dependence of TCR on the doping density. These three HEJ samples have identical structures except for the emitter doping densities, which are 1×10^{17}, 3×10^{17}, and 10×10^{17} cm^{-3} respectively. The results show a decreasing trend in the TCR with increasing doping density. The TCR of these three detectors (summarized in Table 5-1) were calculated at 50K. At higher temperatures the resistance of these devices becomes very small; hence, the safe current limit is reached upon applying few millivolts. Therefore, an accurate calculation of TCR is difficult at higher temperatures for those three detectors. The dependency of TCR with the emitter doping density, at 1V bias voltage across the top and the bottom contact, is illustrated in Figure 5-1. A maximum TCR of 33.4±0.3 % K^{-1} was observed for 1×10^{17} cm^{-3} doped sample (HE0206) at 50 K. The work published by Wissmar et.al. [77] shows a similar behavior in TCR with the doping density for quantum well structures.

A further study using an n-doped structure (Sample # 1329) with similar parameters as above structures except for the emitter doping density of 4×10^{17} cm^{-3}, shows a TCR value of 18.7±0.2 % K^{-1} at 50 K, with 1V bias applied across the detector (shown by the filled circle in Fig. 6-1). The p-doped structure having a doping density closest to 1329 is the HE0205 (3×10^{17} cm^{-3} (p)), and it shows a TCR around 31.5±0.2 % K^{-1} at 50 K. A TCR value of ~31% K^{-1} was estimated for a 4×10^{17} cm^{-3} p-doped device by interpolating the data in Figure 5-1 (TCR vs Doping). This observation predicts that the TCR of p-doped structures are higher compared to n-doped structures. A study by Sun et.al.[78]shows a low carrier density (N) and a steeper gradient in carrier density with temperature (dN/dT) for p-doped structures compared to the n-doped structure from temperatures around 300K down to 80K. This implies a higher variation in the resistance in p-doped structures compared to n-doped structures with variation of temperature. As a result, a better TCR is possible in p-doped structures compared to n-doped structures.

Table 5-2: The TCR of the devices at specified temperatures

Sample	TCR % (Temperature (K))
HE0204	30.6 ±0.2 (50K)
HE0205	31.5 ±0.2 (50K)
HE0206	33.4 ±0.3 (50K)
1329	18.7 ±0.2 (50K)
SP001	5.5 ±0.4 (140K)
SP002	6.6 ±0.3 (140K)
SP003	8.1 ±0.4 (140K) 4.0 ±0.5 (300K)

The inset to Fig. 5-1 shows a TCR variation with the Al fraction, in the barrier layer, of p-doped GaAs/AlGaAs structures SP001, SP002 and SP003. All three sample structures contain 30 periods of undoped AlGaAs barriers and 3×10^{18} cm^{-3} p-doped GaAs emitters. The Al fraction (x) in $Al_xGa_{1-x}As$ barrier layers are 28%, 37% and 57% respectively in these three devices respectively. For comparison of TCR values of these three samples, the measurements were carried at 140 K (maximum operating temperature of SP001). Above this temperature SP001 also shows very low resistance; hence exceeding the safe current limit. The sample with 57% Al fraction (SP003) shows the highest TCR value of 8.1±0.4 % K^{-1} at 140K. Additionally, the SP003 sample also shows a TCR of ~ 4 ±0.5 % K^{-1} at around room temperature. This value is 2 times of the TCR value of VOx bolometers (~2% K^{-1})[79]. This behavior (TCR vs Al%) implies a better TCR for samples with 100% Al (i.e. AlAs), but further studies are needed to confirm this conclusion. The TCR variation in SP003 near room temperature are shown in Fig. 5-2.

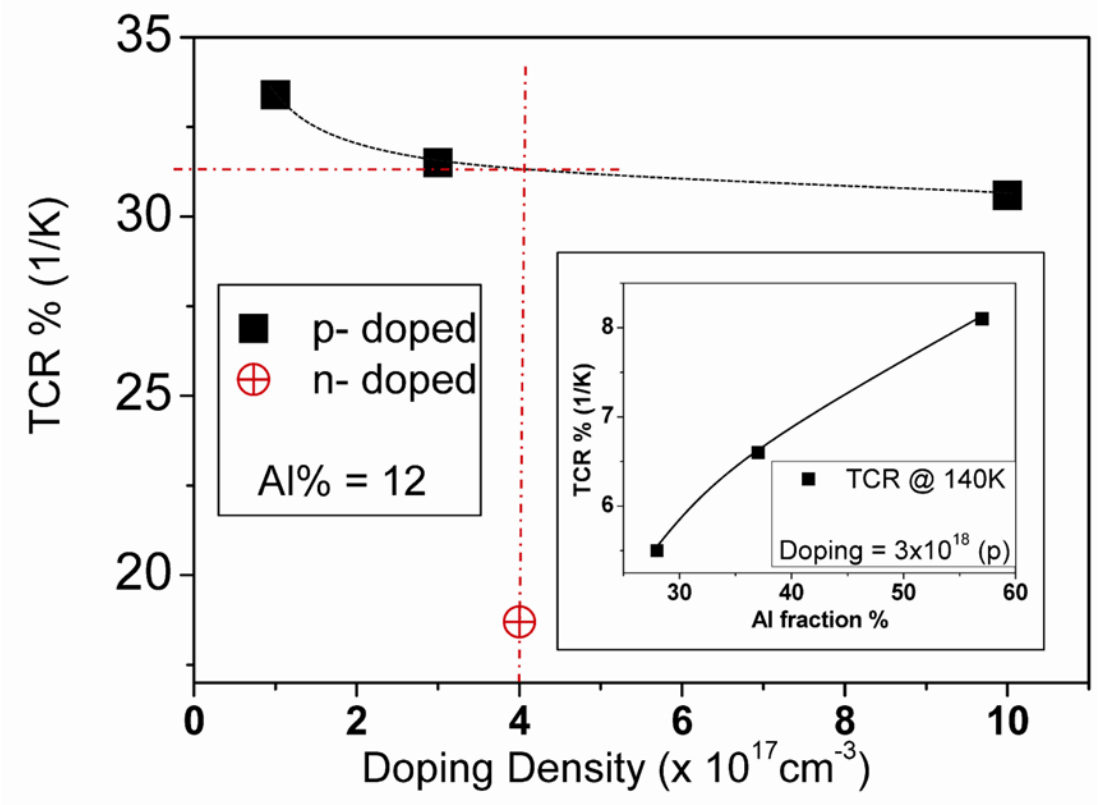

Figure 5-1 : Variation of TCR with doping density of a multilayer heterojunction structure. The structure consists with 12 layers of GaAs/AlGaAs emitter barrier regions (squire p- doped & circle n-doped). TCR values are calculated at the temperature 50K with 1V bias across the structure. The dotted lines (horizontal & vertical) show the intercept point of the TCR interpolated curve for a $4\times10^{17}cm^{-3}$ p-doped structure. Inset: Variation of TCR with Al fraction of a multilayer heterojunction structure. The structure consists of 30 layers of GaAs/AlGaAs emitter/barrier regions with $3\times10^{18}\,cm^{-3}$ p-doped emitter regions. TCR values are calculated at the temperature 140K with 1V bias across the structure.

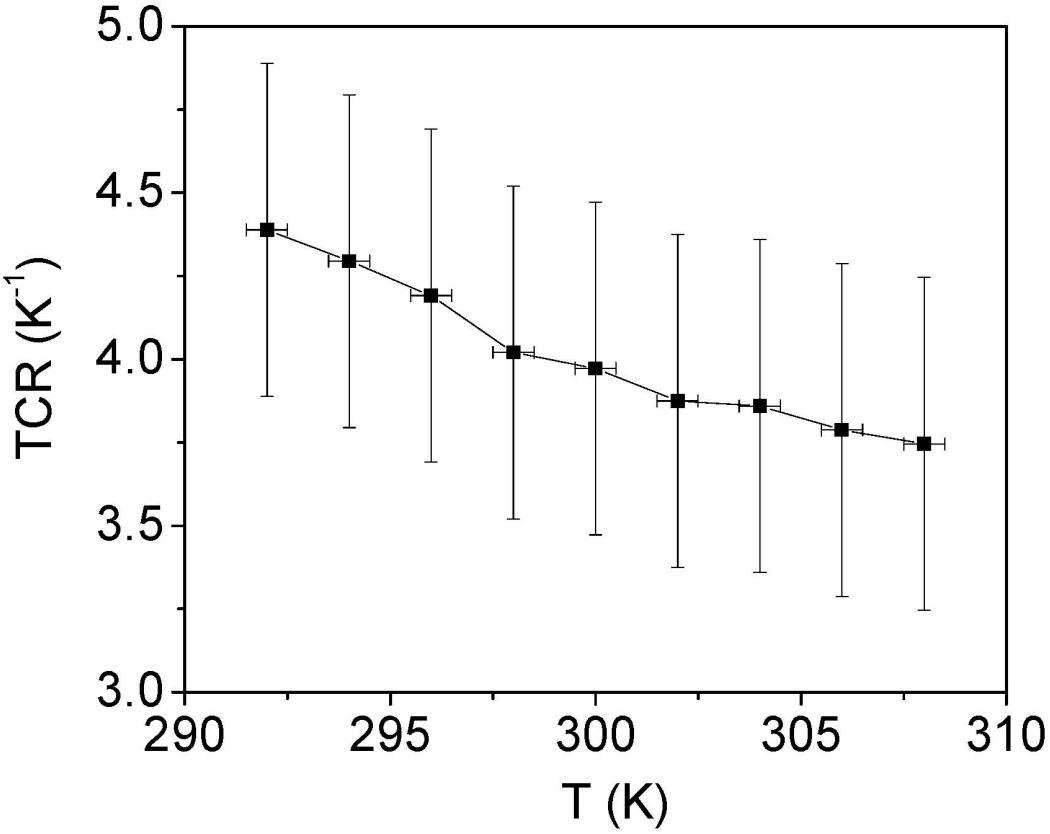

Figure 5-2: The temperature variation of TCR for SP003 near 300 k temperatures.

The specially mounted sample has the same structure as SP003 (the sample with 57% Al fraction). The noise current density of this device structure at two different bias voltages at 300K are shown in Fig.5-2. The device shows flat white noise with a noise current density < 10^{-22} A^2/Hz (~5×10^{-17} V^2/Hz) at higher frequencies (f > 1000 Hz). The theoretical limit in the Johnson noise for a device with similar resistance is 1.4×10^{-23} A^2/Hz (2×10^{-17} V^2/Hz) calculated by Nyquist equation, where k_B is the Boltzmann constant, T is temperature (300K) and R is the device resistance (~1.2 kΩ).

$$\frac{V_J(f)}{\sqrt{\Delta f}} = \sqrt{4k_B TR} \qquad \text{(Eq. 5-2)}$$

$$\frac{I_J(f)}{\sqrt{\Delta f}} = \sqrt{\frac{4k_B T}{R}} \qquad \text{(Eq. 5-3)}$$

The noise power density is around 5×10^{-22} A^2/Hz (~8×10^{-17} V^2/Hz) at the 10 Hz with 1V bias (~0.7mA) for the GaAs/AlGaAs (SP003) bolometer. This noise spectral density is very low compared to noise values reported for different materials including Si (~4×10^{-12} V^2/Hz at 1Hz), VO_x (~10^{-12} V^2/Hz at 0.1Hz) and Ge/Si (~7×10^{-13} V^2/Hz at 250 Hz) alloy [77, 80]. Inset to Fig. 5-3 shows the noise spectra after baseline correction. It shows 1/f noise dominating over the Johnson noise at low frequencies in the device.

The measured response spectrum of the specially mounted sample is given in Fig.5-4. It shows a wavelength independent (flat) response as expected for a bolometer. With a 2.25 V bias across the top and bottom contacts, the device shows a detectivity (D*) of ~ 1.7×10^6 Jones, with a responsively of ~ 3.7 mA/W at 10 µm, operating at room temperature. The 2.25 V is the maximum safe bias voltage that can be applied to the device. The IV characteristic curve shows a drastic increase in the dark current in the device, due to Joule heating, just above this voltage. The response peak appearing in the range 2 µm to 6 µm are believed to be cause by inter band transitions (heavy hole, light hole and split-off hole bands)[81, 82] due to photonic excitations of carriers. The response of the second structure is also showing a similar response, and the values lies within the uncertainty of measurements.

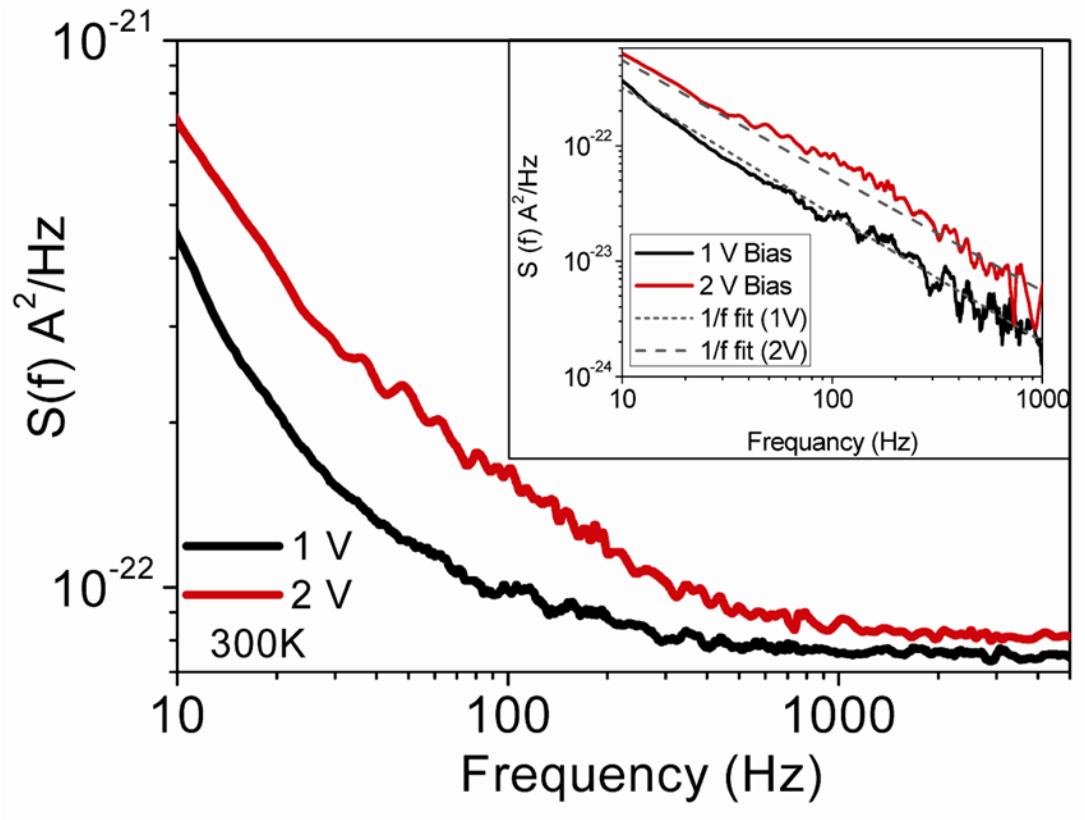

Figure 5-3: Noise current density (S(f)) and fitted data (for 1V and 2V bias) of the sample illustrated in the inset. Inset: The noise spectra after baseline correction. Dotted lines indicate the 1/f fitted curves for 1V and 2V biases.

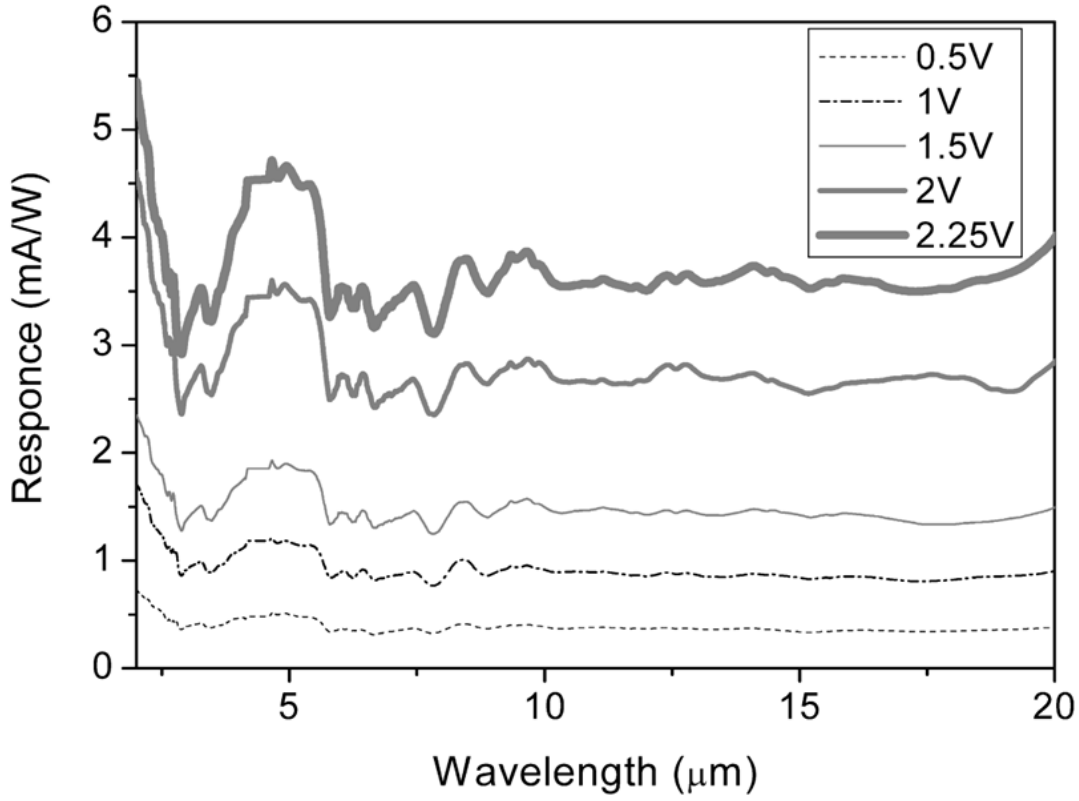

Figure 5-4: Responsivity of the sample consisting of 30 layers of GaAs/AlGaAs junctions with 3×10^{18} cm^{-3} p-doped GaAs regions and Al fraction of 57% (SP003), at different bias voltages.

5.4 Present available bolometer

The Table 5-3 summarizes performance of few of presently available bolometer.

Table 5-3 Performance of few of presently available bolometer

Type	Temperature	Responsivity	Noise power ($W/Hz^{1/2}$)
Golay cell	Room temperature	$10^3 – 10^6$ V/W	10^{-10}
Ge	300 K	8.7×10^7 V/W	10^{-16}
α-Si	Room temperature	10^6 V/W	7×10^{-13}
Si/Bi	100 mK	2.4×10^9 V/W	7.5×10^{-18}
Transition Edge (Mo-Cu)	220 mK	5×10^5 V/W	1.5×10^{-17}
(Ti-Al-Ti)	260 mK	5×10^5 V/W	1.1×10^{-17}
Superconducting bolometer	300 mK	--	3×10^{-19}

5.5 Future work

Based on the results observed above, the higher aluminum fractions and low doping in the GaAs/AlGaAs interface are leading to higher TCR. It will be interesting to have further studies with an undoped GaAs/AlAs superlattice structure. Additionally other material combinations where the band offset at the interface is greater than the band offset of GaAs/AlAs or the InAs/GaSb superlattice structure which have a broken gap band alignment (Type III) at the heterojunction will be interesting to study to understand and achieve possible improvements to TCR and responsivity of a heterojunction supperlattice thermal detector.

5.6 Conclusion

GaAs/AlGaAs multilayer heterojunction structures with different Al fractions and doping densities were tested for TCR values. Structures containing the p-doped GaAs emitter layers showed a better TCR compared to a similar heterojunction structure with n-doped emitters. Furthermore, a GaAs/AlGaAs multilayer structure with 57% Al fraction in the barrier layers showed a TCR value around 4% K^{-1}, at room temperature. This is a higher TCR value compared to that of VO_x or α-Si which is 2% and 2.8% respectively. Therefore with further research p-doped GaAs/AlGaAs heterostructures have the potential to be a competitive candidate in the future production of bolometers or microbolometers working at room temperature. Additionally, the device demonstrates a low noise spectral density, which is a requirement for good performance in a bolometer type detector.

6. EFFECTS OF INCIDENT PHOTON INTENSITY ON THE RESPONSE THRESHOLD OF p-DOPED $Al_xGa_{1-x}As$/GaAs SUPERLATTICE DEVICES

6.1 Introduction

The motivation of this work is to understand the effects of varying intensity of incident photons on p-doped superlattice type devices. Excited carriers alter the occupied energy band levels in conduction or valence bands of a semiconductor material. These alterations in the energy bands will affect the spectral response of type I or type II band alignment. For example, in highly doped semiconductors electrons are present in the lower levels of the conduction band (CB) prevent carriers from further transiting to those occupied energy states; As a result, carriers have to occupy higher energy states. An increase in the material's band gap is resembled when the band gap is extracted by optical methods such as absorption and photoluminescence (PL) spectra. This phenomenon is known as the Burstein-Moss (B-M) Shift [83, 84]. Furthermore, during carrier excitations in a p-doped semiconductor, an electron from a filled state in the valence band (VB) is injected in to an empty state in CB, while generating a hole in the VB as well as an electron occupying a state in the CB. As a result, a phenomenon similar to B-M effect can be observed as the energies of the highest occupied energy level and the lowest unoccupied energy level of the CB and VB will be at further apart from where they were under dark conditions. Optoelectronic devices, based on band gap excitations and CB offset is affected by B-M effect.

Many-body interactions caused by carrier occupancy in the CB and the holes generated in the VB result in band gap narrowing (BGN). Additionally, ionized dopants in doped materials also contribute to the BGN. As the occupancy of carriers in CB and VB are differ under different incident photon intensities, the BGN also rely on the incident photon intensity. This implies the occupied and unoccupied levels in CB and VB respectively will be shifted further apart or closer to each other, depending on the magnitudes of each shift (difference between B-M and BGN) and incident photon intensities. As a result, the effective band gap will either increase or decrease, resulting in a blue or red shift in spectral measure-

ments for inter-band transitions. BGN is affecting the response of optoelectronic devices based on band gap excitations and VB offset.

Studies have revealed energy shifts causing a red shift in the response spectra due to BGN on p-doped GaAs/AlGaAs quantum well structures [85]and other types of optoelectronic devices [86].The consideration of the B-M effect and BGN effect is critical when designing detector structures for far infrared (FIR) and terahertz (THz) detection, as the detection mechanism in these devices are based on inter band or intra band transitions of carries across small band offsets (barriers) or energy gaps. And B-M effect and BGN effect can cause a significantly larger shift in the detectors' response range from its intended response range. In the case of large shift in a FIR/THz detector, the device may be not functional by making the barrier extremely small and have increasing the thermal excitations.

6.2 Experimental procedure

Thin films were grown by molecular beam epitaxy on a semi-insulating GaAs substrate. Sample parameters are summarized in Table 6-1. Two GaAs thins films were p-doped with Beryllium to 5×10^{17} cm^{-3} and $8\times10^{18}cm^{-3}$ and are labeled as GA517 and GA818 respectively and the sample GA116 is an undoped GaAs thin film. The two AlGaAs thin films, labeled as AGA1 and AGA20, consist of aluminum fractions 1% and 20% respectively, and are p-doped to 3×10^{18} cm^{-3} with Beryllium.

The band gap of GaAs and AlGaAs thin film samples were calculated using photoluminescence (PL) spectra. These thin films were grown by molecular beam epitaxy on a semi-insulating GaAs substrate. Two GaAs thins films were p-doped with Beryllium to 5×10^{17} cm^{-3} and $8\times10^{18}cm^{-3}$ and are labeled as GA517 and GA818 respectively and the sample GA116 is an undoped GaAs thin film. The two AlGaAs thin films, labeled as AGA1 and AGA20, consist of aluminum fractions 1% and 20% respectively, and are p-doped to 3×10^{18} cm^{-3} with Beryllium. The PL spectra of the thin film samples were measured under varying temperatures and incident photon intensities after mounting on the cold finger of a closed cycle

refrigerator and excited with an argon-ion laser (488 nm) with different output photon flux intensities calibrated by a silicon photo detector. The 5% of the PL peak maxima were used to calculate the band gap in the material, and the low energy edge of the PL spectra give the lowest energy difference between CB and VB energy, while the higher energy edge gives the energy difference between the highest occupied level in CB and lowest unoccupied level in VB [87].

Table 6-1 Summary of thin film sample parameters

Sample	**Material**	**Aluminum fraction**	**Doping density (cm^{-3})**
GA116	GaAs	-	Undoped
GA517	GaAs	-	5×10^{17}
GA818	GaAs	-	8×10^{18}
AGA1	AlGaAs	1%	3×10^{18}
AGA20	AlGaAs	20%	3×10^{18}

The theoretical band gap of the thin film samples under different temperatures were calculated using the Eq. 6-1. [88].

$$\overline{E}_g = E_c - E_V - E_{BGN} = E_g(0) + \frac{\alpha T^2}{(\beta + T)} - E_{BGN} \qquad \text{(Eq. 6-1)}$$

Where $\bar{E}_g$ is the total energy gap and EC, EV, EBGN, are the CB, VB, and band narrowing energies respectively. $E_g(0)$ is the band gap energy at 0 K, and EF is the Fermi energy level in electron volts (eV) for AlxGa1-xAs. The two coefficients, α = -5.41×10^{-4} eVK^{-1}, and β = 204 K for GaAs [89]. $E_g(0)$ is the direct band gap of $Al_xGa_{1-x}As$, and is calculated using the equation 6-2. [89, 90]

$$E_g(0) = 1.519 + 1.155x + 0.37x^2 \quad \text{(Eq. 6-2)}$$

The temperature dependent Fermi Energy level is calculated by[14, 90]

$$E_V - E_F = kT\left(\ln\left(\frac{p}{N_V}\right) + 2^{-3/2}\left(\frac{p}{N_V}\right)\right) \quad \text{(Eq. 6-3)}$$

Where, E_V, E_F, k, p, and N_V are the valence band energy, Fermi energy, Boltzmann constant, doping density and the density of states in the valence band respectively. The temperature dependency of N_V, for $Al_xGa_{1-x}As$ was calculated by the equation 6-4 [89],

$$N_V = 4.82\times10^{15} T^{3/2}(0.51 + 0.25x)^{3/2} \quad \text{(Eq. 6-4)}$$

The band gap narrowing of a material primarily depends on four different parameters [91, 92]. The exchange interactions and carrier-impurity interactions affect the majority carrier band, and carrier-carrier or electron-hole interactions and carrier impurity interactions affect the minority carrier band. The band gap narrowing of p-doped AlxGa1-xAs is calculated by the following equation [91, 93], which gives E_{BGN} of 20.7 meV for GaAs with the doping density (p) of 5×10^{17} cm^{-3} at room temperature.

$$E_{BGN} = 9.71(1+0.09x)\left(\frac{p}{10^{18}}\right)^{\frac{1}{3}} + 12.19(1+0.42x)\left(\frac{p}{10^{18}}\right)^{\frac{1}{4}} + 3.88(1-0.23x)\left(\frac{p}{10^{18}}\right)^{\frac{1}{2}}$$

(Eq. 6-5)

The differences between the band gaps calculated using Eq. 6-1 and PL data were used to estimate the variations in B-M effects, and BGN narrowing effects due to changing intensity of incident photon intensities. Additionally, PL data was also used to analyses the band offsets at GaAs/AlGaAs interfaces and band offset variations due to incident photon intensities. Even though various ratios, from 10:90 up to 50:50 can be found in literature as the VB:CB energy offset ratio in GaAs/AlGaAs heterostructures [14] the 40:60 ratio is use in the calculations because the VB offset calculated by any other ratio will give a lower value for VB offset compared to the value given by a 40:60 ratio.

6.3 Results and Discussion

6.3.1 Burstein-Moss (B-M) and band gap narrowing (BGN) effects on GaAs

It is important to understand the B-M and BGN effects of doped GaAs, as in majority of GaAs/AlGaAs hetero-junction devices GaAs is used as the carrier emitter; therefore, the changes in the band gap of GaAs is directly affecting the device response. Band gaps calculated for GA517 using Eq. 6-1, and PL under different temperatures are shown in Fig. 6-1. The $PL_{(Low)}$ and $PL_{(High)}$ correspond to the band gap calculated by low and high energy slopes in PL spectra respectively. The E(T) and E(T)-BGN are the band gap calculated by Eq. 6-1, omitting and considering the BGN (E_{BGN} term in Eq. 6-1) respectively. As shown in the inset of Fig. 6-1, the low energy slope in the PL spectra correspond to the lowest band gap and the high energy slope defines the energy difference between the highest occupied and lowest unoc-

cupied energy levels in the CB and VB respectively. Therefore, PL spectra can be used to determine both the BGN and B-M effects in the material. As expected, due to B-M and BGN effects band gap calculated using the low energy slope of PL spectra shows the lower values, and high energy slope shows highest band gap compared to the band gap calculated by Eq. 6-1 without considering BGN (E(T) in Fig. 6-1).

The band gap shown in $PL_{(Low)}$ is smaller than the predicted value by Eq. 6-1 (the data set E(T)-BGN in Fig. 6-1), due to enhanced BGN caused by incident photon intensity during the PL measurement. The BGN will be affected by increasing the number of carries in the excited states of CB and reduction of carried in the VB, creating a greater coulomb attraction forces between the CB and VB states due to the intensity in illumination. The variation in the band gap calculated by low energy slope of PL spectra at 25K under illumination intensities of ~ 60 and ~250 $mWcm^{-2}$ are shown in Table 6-2. A reduction in the band gap with increasing incident photon intensity can be observed from the data in Table 6-1, especially under high temperature (T ≥100 K), which implies a temperature dependence in the BGN under illumination intensity. At low temperatures the intensity dependence is not prominent due to carrier freezing, as the number of excitations will be inadequate at low temperature to illustrate the intensity dependence.

But compared to dark, illumination have carriers in the excited states resulting the difference in PL(low) and E(T)-BGN data in Fig. 6-1. On the other hand, in Eq. 6-1 the temperature dependence of the BGN is not considered, this factor will also affect the large difference seen between the $PL_{(low)}$ and E(T)-BGN data. As observed by the PL data BGN will decrease at low temperatures. Additionally, The $PL_{(High)}$ data shows an increase in the energy with increasing temperature, i.e. increase the energy difference between $PL_{(Low)}$ and $PL_{(High)}$ data, caused by carriers in the CB occupying higher energy states due to thermal excitations.

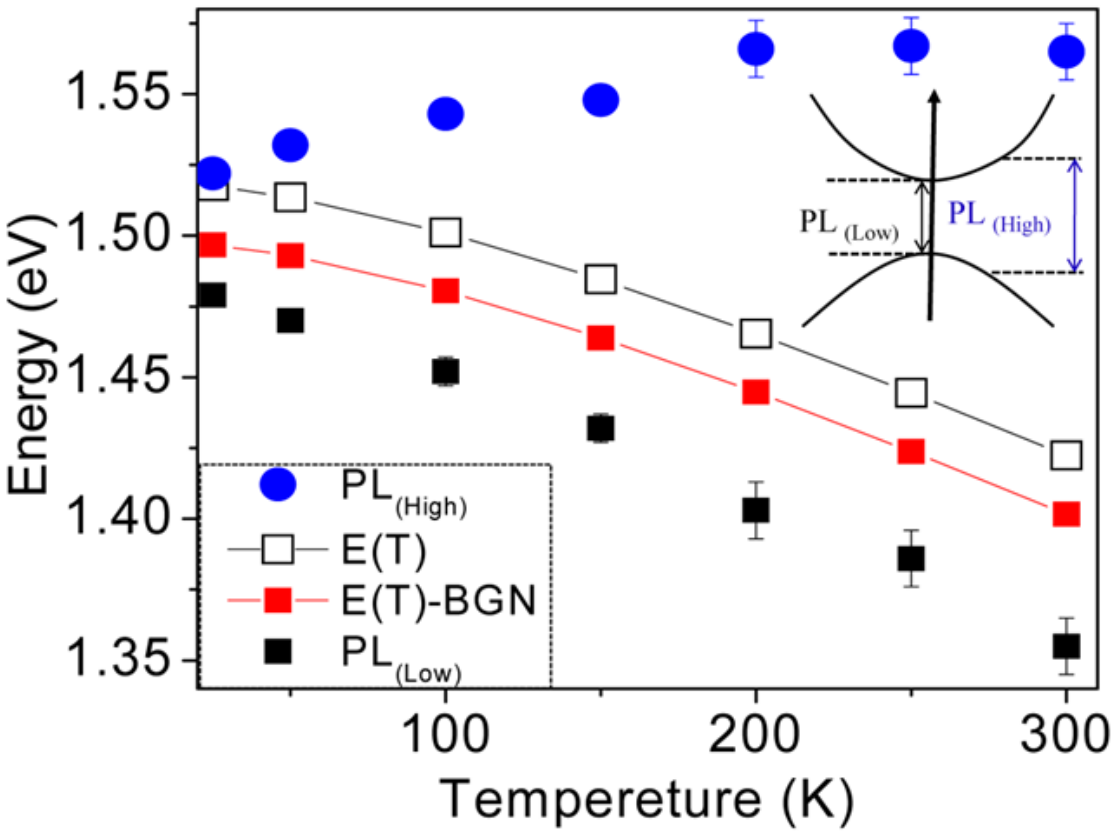

Figure 6-1: The comparison of the calculated and experimental band gaps at different temperatures for p-doped GaAs thin film with doping 5×10^{17} cm^{-3}. E(T) is the band gap calculated without considering band gap narrowing (BGN) in Eq.6-1. PL (low) and PL (high) are the band gap calculated using low and high energy slope of photoluminescence respectively E(T)-BGN is calculated band gap using Eq.6-1. Inset: Illustrate the calculated energies representations in a band diagram.When the sample is illuminated, carriers will be excited to the conduction band. An accumulation of charges in the CB and deprivation of carries in VB will results in a B-M shift, hence PL should have high energy emission. Similarly interactions of carriers in CB and VB will result in the BGN, hence also produce low energy photons correspond to lowest band gap in the material.

Table 6-2: The band gap calculated by PL for GA818, GA116, AGA20 and AGA1at 25 K under the illumination if 60 and 250 mWcm^{-2} and by Eq.6-1 with (E(T)-BGN) and without (E(T)) bang gap narrowing effects.

Sample	**Band gap at 25 K (eV)**			
	60 mWcm^{-2}	**250 mWcm^{-2}**	**E (T)**	**E(T)-BGN**
GA818	1.456±0.001	1.451±0.001	1.517±0.0005	1.466±0.0005
GA116	1.483±0.001	1.486±0.001	1.517±0.0005	1.496±0.0005
AGA 20	1.670±0.001	1.670±0.001	1.763±0.0005	1.752±0.0005
AGA 1	1.472±0.001	1.468±0.001	1.529±0.0005	1.492±0.0005

The band gap calculated for GA818, GA116, AGA1 and AGA20 at 25 K by PL subjected to 60 and 250 mWcm^{-2} illumination and calculated using Eq. 6-1 with and without considering BGN are presented in the Table 6-2. For all samples the band gap calculated by PL are lower than the band gap calculated mathematically. The GA818 has a lower band gap compared to the low doped samples, GA116 and GA517, where the difference is ~27 meV and ~25 meV at 25 K resulted by BGN due to high number of dopants and the band gap further decrease by ~ 5 meV with high intensity illumination. GA517 and GA116 shows increasing band gap as the dopants density reduces respectively. On contrast, the band gaps of the two doped samples only differ by ~ 2 meV. Interesting observation on the band gap of low doped samples is that both samples shows an increase (blue shift) in the band gap by ~ 2 - 3 meV under expose to 250 mWcm^{-2} intensity illumination compared to the 60 mWcm^{-2}, which is different from what is observed for the high doped GaAs thin film (GA818).These results shows BGN effects due to incident

intensity variation are dependent of doping density, and higher doped GaAs are more susceptible to BGN and effects of incident light intensity on BGN.

Furthermore, out of the two AlGaAs thin films the AGA1 with 1% aluminum fraction do show a decrease in the band gap by ~ 4 meV with illumination intensity of 250 $mWcm^{-2}$ compared with 60 $mWcm^{-2}$. And the band gap of AGA1 is smaller than the band gap of AG116 and AG 517 by ~ 11 meV and 9 meV respectively due to BGN caused by higher doping. On contrast, the band gap of AGA20 was not changed with the light intensity due to the high band gap in the AGA20, the band separation is too large and hence the coulomb interaction effects are too weak to alter the band gap.

6.4 Effects of light Intensity on valence band offset of optoelectronic device (p-GaAs/ AlGaAs)

Above results shows band gap alternations in materials under varying incident photon intensity resulting in barrier heights to differ from what is intended for optoelectronic devices, and hence a change in the response. Further examining the effects, the VB offsets was estimated for two p-doped AlGaAs/GaAs heretojunctions with, (a) 20 % aluminum and (b) 1% aluminum in respective barriers using the band gaps extracted from Eq. 6-1 and PL spectra, for the three thin film samples GA517, AGA20 and AGA1.

For the structure with 20 % aluminum barrier (i.e., assuming that the junction made with GA517/AGA20), the valence band offset calculated by PL is 76.4±1 meV and the band offsets calculated by Eq. 6-1 is 91.3 meV for the device at 25 K, rendering a difference of ~15 meV in the barrier offset estimated using PL and Eq. 6-1 as expected by earlier observations. This indicates that the devices will have a long wavelength threshold while operating at low temperatures. In the high barrier device, the tolerance may be in an acceptable range depending on the required operational accuracy.

But the predicament arises in the structure with 1% aluminum in the barrier (i.e., junction made with GA517/AGA1), as can be seen in the Fig. 6-2, the theoretical data by Eq. 6-1 shows a band offset of -1.8 meV (negative barrier height indicate the higher energy at the GaAs layer, caused by higher p-doping in the $Al_{0.01}Ga_{0.99}As$ thin film compared to GaAs) and the band offset calculated by PL is 2.4 ± 1 and 2.8 ± 1 meV for the temperatures 50 K and 25 K respectively. But, at higher temperatures the structure do not show a significant band offset (VB offset < 0.5 meV). Hence the device will not have expected photo response, and can only function as a resistor under bias. This illustrates the importance of considering the effects of photon flux intensities on band alignments in the device. This result clearly indicates of devices with small band offsets are required to operate at low temperature.

Table 6-3: The variation in the band gap for GA517, at 25K, 50 K and 100 K calculated by low energy slope of PL spectra under illumination intensities of ~ 60 and 250 $mWcm^{-2}$

Incident Intensity	**Band gap (eV)**		
	25K	**50K**	**100K**
60 $mWcm^{-2}$	1.481±0.001	1.472±0.001	1.469±0.002
250 $mWcm^{-2}$	1.483±0.001	1.471±0.001	1.461±0.002

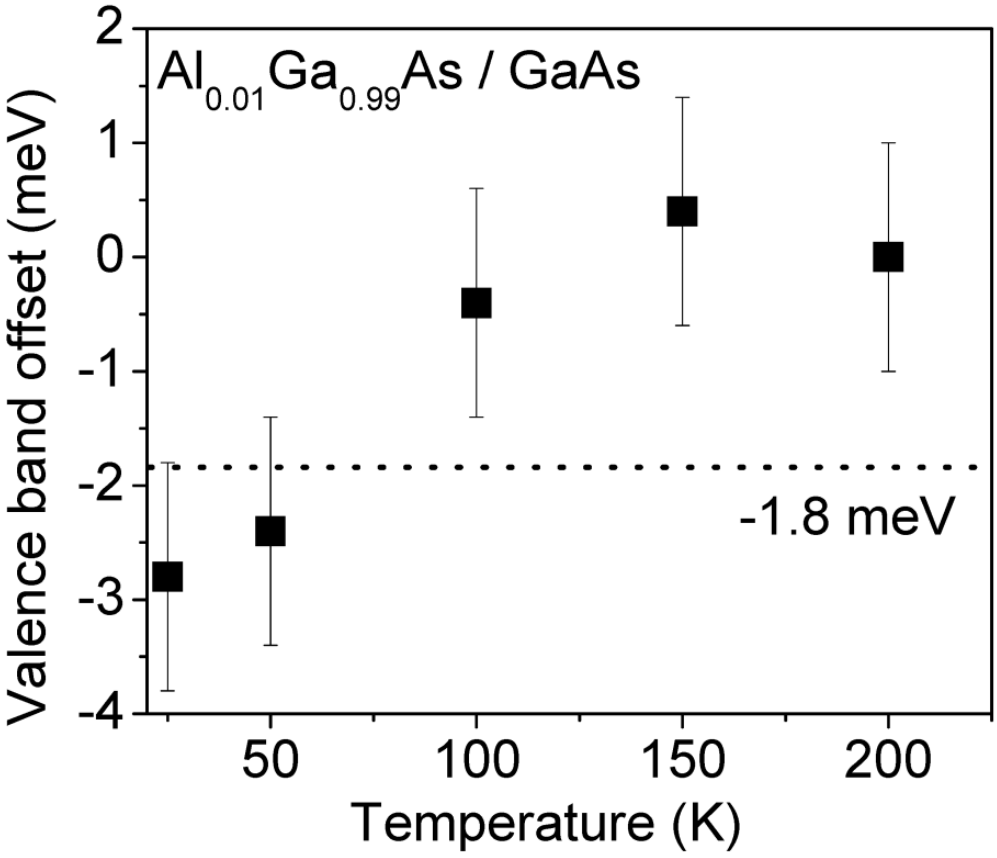

Figure 6-2: The variation of valence band offset for p-doped AlGaAs/GaAsheretojunctions assuming 60:40 band alignment at AlGaAs:GaAs interface and band gap extracted by PL spectra with 250 $mWcm^{-2}$ incident photon intensity. Dotted line represent the band offset 1.8 meV, extracted from Eq. 6-1. Negative band offset indicated GaAs layer have the higher energy.

6.5 Comparison of valence band offset on optoelectronic device with low barrier (GaAs/p-AlGaAs)

On comparison of the band offset calculated by PL and in a device with very small barrier, a terahertz (THz) detector consists of undoped GaAs barriers and p-doped $Al_{0.01}Ga_{0.99}As$ emitters operating at 4.2 K is successfully demonstrated by Matsik et. al. [94]. The expected band offset obtained by response threshold for the device is 15±0.1 meV as reported by Matsik et. al. The band off set at the GaAs/$Al_{0.01}Ga_{0.99}As$ interface in the device is ~ 5.3 meV (x*530 meV) and the deficit of ~ 9 meV is resulted by the residual doping in the GaAs barrier [94]. The band gap calculated by PL(Low) for p-$Al_{0.01}Ga_{0.99}As$ and undoped GaAs thin films at 25 K shown in Table 6-2 gives the VB band offset for a p-$Al_{0.01}Ga_{0.99}As$ - undoped GaAs interface as ~5.8±0.2 meV (PL spectra at 4.2 K is not available due to instrument limitations). The residual doping effect observed in the undoped GaAs barrier of the device reported by Matsik et. al. can be the cause of observed band gap increasing for GA116 and GA517 in the PL measurement under increased intensity. This implies that the materials used for FIR and THz detectors should be with low doping densities. Furthermore, the data shown in Fig. 6-2 indicates an increase in band offset with the decreasing temperature from 50K to 25K. This trend can also be expected for the p-$Al_{0.01}Ga_{0.99}As$/undoped GaAs interface; hence the VB offset will be greater than 5.8 meV (at 25 K) when the temperature decreases to 4.2 K.

Additionally, the band gap of both the undoped GaAs (GA116) and p-doped $Al_{0.01}Ga_{0.99}As$ (AGA1) shows an increase approximately by similar amount, i.e., by ~ 3±1 meV and 4±1 meV respectively under illumination of 250 $mWcm^{-2}$ compared to 60 $mWcm^{-2}$. This implies BGN under varying incident photon intensity is similar for both GA116 and AGA1, hence the barrier offsets at the undoped GaAs / p-doped $Al_{0.01}Ga_{0.99}As$ interface should not have a significant difference under varying illumination intensities. Since the effects on BGN due to carrier excitations by photon flux intensity is similar for both the materials it can be conclude that the material combination p-$Al_{0.01}Ga_{0.99}As$ and undoped GaAs using as emitter and barrier will be more reluctant to the barrier height alternations caused by photon intensities at

low temperatures. Therefore, a sustainable band offset can be present in the device at low temperature. And this low sensitivity to the incident photon intensity may be the cause of successful operation of the device presented by Matsik et. al., in addition to the effective barrier height increase due to residual doping in GaAs barrier can be high as 13 meV, as described by Rinzan et. al. [95]. The residual doping effect in the structure will also defy the decreasing of effective band offset under illumination.

6.6 Conclusion

The effects caused by alternations in highest occupied and lowest unoccupied energy levels in CB and VB due to carrier excitations of p-doped GaAs/AlGaAssuperlattice structures are demonstrated using response threshold of the device. Superlattice structures with multiple periods of GaAs/$Al_{0.57}Ga_{0.43}As$ emitter/barrier regions have demonstrated a red shift in the infrared response due to the band renormalization effect. The response threshold shift was caused by illumination intensity; due to carrier confinements in narrow layered structure. The B-M effect in p-doped materials was further confirmed by absorption and PL measurements on a p-doped GaAs thin film. The GaAs thin film has shown a red shift in the band gap calculated theoretically and using optical methods, such as absorption and PL. The VB offsets and causes on the offsets due to illumination intensities are also demonstrated using hypothetical hetero junctions. Due to the presence of threshold shifts in the visible and infrared response of the superlattice structure, it is important that the B-M effects and band renormalization effects to be taken into account when designing narrow band detector structures, especially for long wavelength response such as terahertz and far infrared detectors when operating at temperatures > 50K. Results also show possibility of using the combination of undoped GaAs as barrier and p-doped AlGaAs as the emitter to inhibit the illumination intensity effects.

7. EXCITON TRANSPORT AND ELECTRON MOBILITY OF ORGANIZED AGGREGATES OF CATIONIC DYE THIOCYANATES

7.1 Introduction

Light absorbed by organic solids creates Frenkel excitons diffusively transported until they decay via recombination or decompose into free carriers at an interface [96, 97]. Transport of excitons is greatly facilitated in organized molecular assemblies, notably J- aggregates where the transition dipole moments are strongly coupled [98-102]. The properties of J-aggregates of organic molecules, especially those of dyes have been extensively investigated, both experimentally and theoretically, opening up novel optoelectronic device concepts. The possibilities of adopting J-aggregates in solar cells [103-105], photon detectors[106], electroluminescent devices [107, 108], excitonic transistors [100, 109] and switches [110], lasing systems and microcavity devices [108] continue to attract much attention. Familiar photovoltaic and photoconductive photon detectors are based on inorganic semiconductors. Versatile low noise low cost devices sensitive even to a single low energy photon may be deviced adopting dyes and other organic compounds via molecular assembly-solid interface engineering [106, 111, 112].

Thin films of organized aggregates of small molecules, exhibiting fast exciton transport and mobility of one type of carrier (electron or hole) receive much attention as promising materials for development of excitonic solar cells and photon detectors [102, 113, 114]. The basic operation mechanism of these devices is diffusion of photogenerated excitons, their decomposition at the boundary of another material with mobile carriers of the opposite sign (hole or electron). Most J-aggregates have large exciton diffusion coefficients but low carrier mobilities while the H-aggregates exhibit the opposite behavior [115]. The reason for low carrier mobility in J-aggregates seems to be the tendency for accumulation disorder in the film casting process than a fundamental constraint. Chromopore molecular assemblies with large exciton diffusion lengths and a high mobility for one type of carrier are desirable systems for many optoelectronic device applications.

In most studies, J-aggregated thin films of long range order are formed by Langmuir Blodgett technique, spin casting in a polymer matrix or via layer-by-layer deposition [116-119]. In this note we describe a simple technique for deposition of highly organized J-aggregated thin films of cationic dye thiocyanates exhibiting large exciton diffusion lengths and enhanced electron mobilities on copper based substrates, CuSCN, CuI and Cu_2O. Mechanism involved is explained as strong S-bonding of the SCN- ions to the copper substrate and templated self-assembling of dye cations and thiocyanate anions to form a repetitive organized structure. Construction of a model solar cell of the configuration n-Cu2O/J-aggregated Rhodamine B /p-CuI is described.

7.2 Experimental procedure

Commercial (Aldrich) Rhodamine B in the chloride form (RhBCl) was converted to the thiocyanate (RhBSCN) by boiling the dye powder in a saturated aqueous solution of KSCN. The large excess of KSCN ensures that the reaction RhBCl + KSCN → RhBSCN + KCl proceeds in the forward direction. RhBSCN insoluble in cold aqueous KSCN, is separated, dissolved in ethanol and recrystallized. Recrystallized samples are subjected to the previous process few times to purify the dye and eliminate all chloride. p-CuSCN was coated on copper plates (1 × 1.5 cm^2) electrolytically from an aqueous solution of KSCN containing propan-2-ol (~ 1 v %) [120]. n-Cu_2O was coated on copper plates (1 × 1.5 cm^2) by boiling the plates in a 10^{-4} M solution of $CuSO_4$ for several hours[121]. Fluorine doped conducting tin oxide (FTO) glass plates were coated with TiO_2 by spraying a solution of titanium isopropoxide in propan-2-ol and sintering at 450^{o}C.

RhBSCN was deposited on p-CuSCN and n-Cu_2O coated copper plates by keeping the plates suspended in 0.05 M solution of RhBSCN containing 5% (volume) ethanol at 25^{o}C. A large volume of dye solution (100 ml) was kept magnetically stirred so that the effect of dilution due to dye adsorption is negligible. The amount of dye adsorbed was determined by extraction of the dye into ethanol and spec-

trophotometric estimation. (As the linear dimension of the RhB molecule is ~ 1.7 nm, 1 monolayer in 1 cm^2 = $5x10^{11}$ moles. The spectrophotometric detection limit of RhB ~ 10^{-8} mol/litre, enables detection of ~ 1 monolayer in 1 cm^2 extracted into 1 cm^3 of ethanol. Optical microscopic examination of the film indicated that the film is uniform and aggregated dye grains embedded on the surface are absent.)

The white light (tungsten filament lamp at 250 Wm^{-2}) photoresponse of the RhBCSCN dye films deposited on different substrates were recorded by measuring the short-circuit photocurrent (Isc) in photoelectrochemical cells (PECs) in 3-electrode configuration with a Pt counterelectrode and SCE standard, in an iodide/tri-iodide electrolyte.

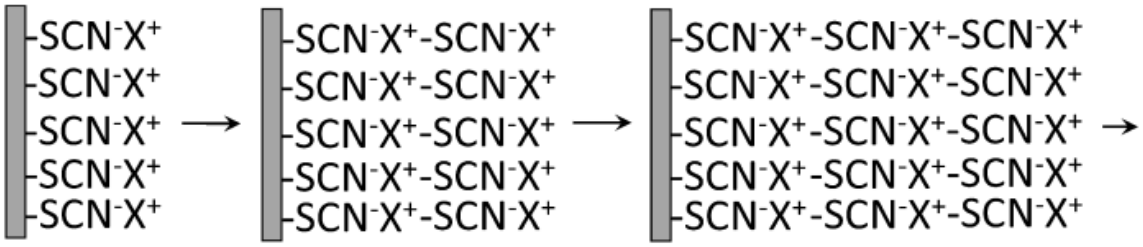

Figure 7-1: Schematic representation indicating growth organized self-assembled thin film of the cationic dye XSCN (X+ = chromopore cation) on a copper based substrate

Heterojunctions of the configuration n-Cu_2O/J-aggregated RhBSCN/p-CuI were fabricated as follows. A film of RhBSCN was deposited on n-Cu_2O coated copper plates by the method described above. Counterelectrode was prepared by coating ~ 4μm layer of CuI from a 0.3 M solution of acetonitrile containing ~ 10^{-4} M guanidinium thiocyanate acting as a CuI crystal growth inhibitor. The cell was formed by pressing and clamping the counterelectrode against the dye coated surface painted with CuI to establish contact. Heterojunctions n-TiO_2/J-aggregated RhBSCN /p-CuI were fabricated by growing a RhBSCN film

on CuI deposited on FTO glass and pressing the TiO_2 coated FTO glass plate against the dye surface. The IV characteristics and the photocurrent action spectra were measured using a source meter and a monochromator set-up.

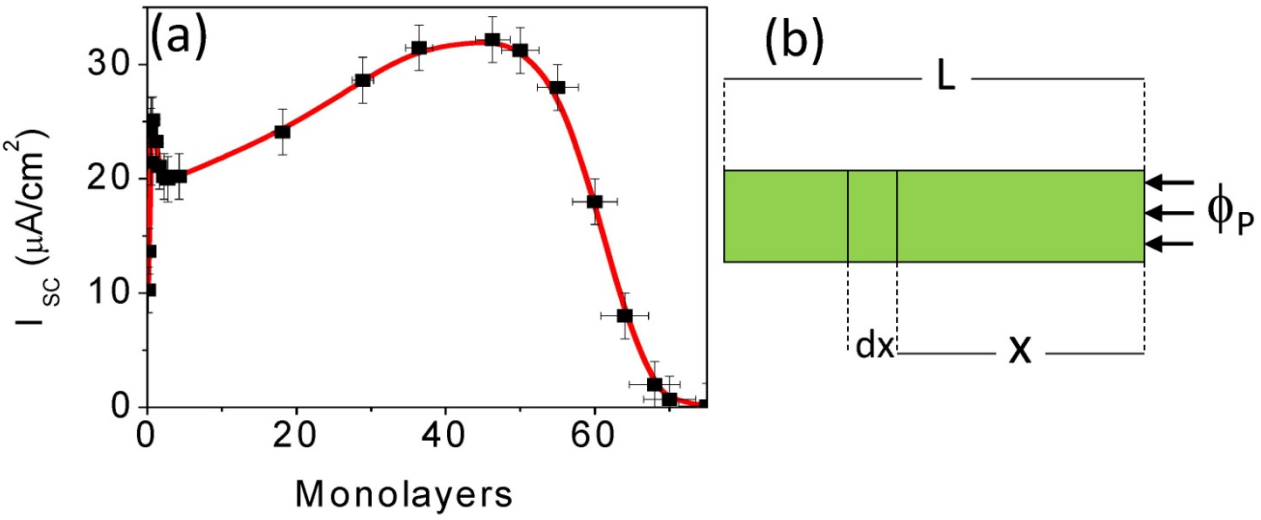

Figure 7-2: *(a)* Variation of the short-circuit photocurrent (I_{sc}) of RhBSCN coated p-CuSCN photocathode in iodide/tri-iodide electrolyte (Illumination 250 Wm^{-2}, Tungsten filament lamp). *(b)* Sketch explaining the dye film geometry used in derivation of eqn.(1). Photon flux ΦP is incident on dye film/electrolyte interface (x = 0), other interface (x = L) is CuSCN/dye

D.C electrical conductivities of solid RhBCl, RhBSCN were determined by two probe measurements using compacted pellets. The conductivity of the RhBSCN film deposited on copper based substrates was estimated by measuring resistance of the plates before and after deposition of the dye film. Electron mobilities of RhBCl, RhBSCN, RhBSCN films deposited on Cu substrates were estimated by measuring space charge saturated current using the Mott-Gurney equation. Organic materials have very low mobilities in general. Grain boundaries also play an important role and purity is even more important. Additionally, the Mott -Gruney measurement can be effected by moisture and thermoelectric

injection; hence it is not a refined measurement. But, the Mott -Gruney measurement are frequently used in estimating mobilities of organic semiconductor materials.

7.3 Results and Discussion

A peculiar phenomenon observed in adsorption of RhBSCN and many other thiocyanates of cationic dyes (XSCN) on copper based substrate (Cu, CuSCN, CuI, Cu_2O) plane surfaces is continuous increase of the thickness of the dye layer provided the dye solution is constantly homogenized maintaining a constant concentration . For a given solvent composition (vol. % ethanol) and temperature, the film continues to grow if the dye concentration in the solution exceeds a critical value. The process of film growth can be understood as follows. Thiocyanate ions are strongly adsorbed on the surface via S-bonding to the Cu sites [122, 123]. Subsequently, the dye cation X^+ bonds electrostatically to adsorbed SCN- forming an organized monolayer of SCN^-X^+. The monolayer with X^+ lying at the surface exposed to the solvent acts as a template, the dipolar forces attach SCN- ion to SCN^-X^+ to form $SCN^-X^+SCN^-$ and an electrostatic bond with X^+ built two layers $SCN^-X^+SCN^-X^+$ and the processes continues indefinitely as represented schematically in Fig. 7-1. The initial strong bonding of SCN^- ions onto the Cu based surface followed by electrostatic bonding of the dye cation is the crucial condition that leads to formation of an organized J-aggregate of the dye, spread over a large area. In most familiar situations of J-aggregate formation of dye films on a surface, all the dye molecules are not identically oriented to form the first monolayer which acts as an template for the progressive growth of the dye film. The monolayer thickness of the film is estimated on basis of linear dimension of the dye molecule (RhBSCN ~ 1.7 nm).

Variation of the short-circuit photocurrent (I_{sc}) of a RhBSCN coated p-CuSCN photocathode with the monolayer thickness of the dye film similar to shown in Fig. 7-2 was previously observed and published in a studies on dye sensitization, although the mechanism involved was not elaborated and explained [124]. According to Fig. 7-2, photocurrent sharply increases, reaching a maximum at a dye cov-

erage corresponding to a monolayer, then declines and gradually increases reaching a much higher second maximum at dye coverage of approximately 46 monolayers, corresponding to a film thickness of ~ 78 nm. On further increase of the film thickness, photocurrent decreases and beyond ~ 75 monolayers, it is too small for resolution against noise. The similar variation of I_{sc} with monolayer film thickness was seen in RhBSCN films deposited by the same procedure on CuI and Cu_2O surfaces but not on TiO_2. The absence of this behavior in RhBSCN deposited on TiO_2, clearly indicate that the template effect of SCN- bonding to Cu based substrate has been the essential initial condition for the growth of an organized molecular assembly in this dye.

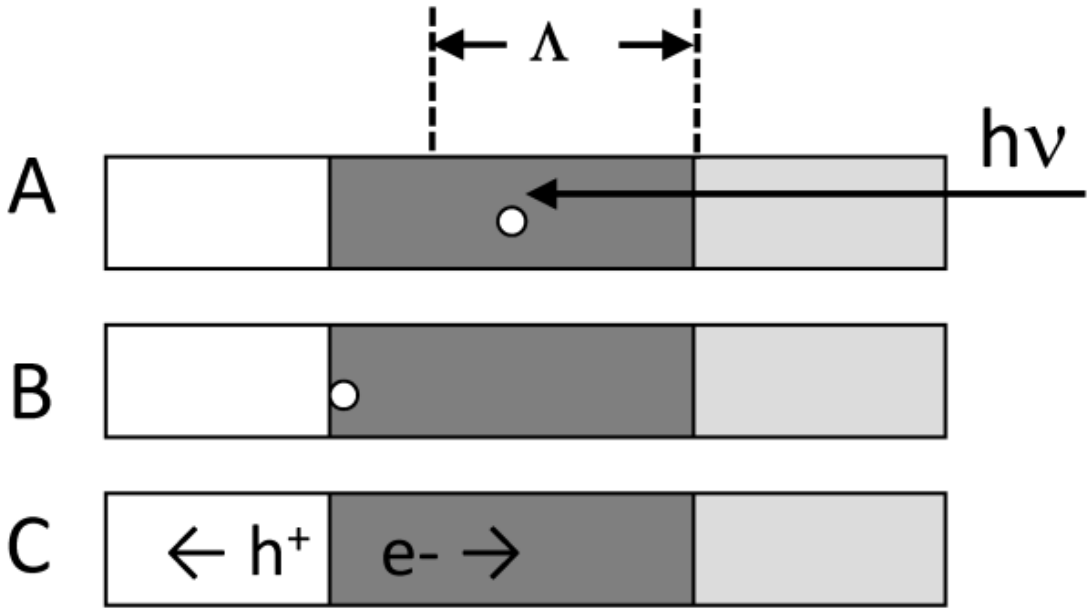

Figure 7-3: Mechanism of photocurrent generation by in p-CuSCN (or p-CuI) photocathode deposited with RhBSCN J-aggregate (A) *exciton creation by an absorbed photon* (B) exciton diffusing to the CuSCN /RhBSCN boundary (C) hole and electron release to CuSCN and RhBSCN respectively (white rectangle – CuSCN, dark grey rectangle-RhBSCN, grey rectangle – aqueous electrolyte). The extent marked as Λ is the exciton diffusion length.

In familiar dye-sensitization, only the monolayer of molecules attached to the semiconductor surface inject carriers to a band. Generally, the excess dye molecules randomly agglomerated over the surface has a deleterious effect because of concentration quenching, while J-aggregation sometimes contribute favorably to the sensitized quantum efficiency [125, 126] The unusual effect of enhanced sensitization by the significantly thick dye layer can be understood as follows: The absorption spectrum of an aqueous solution RhBSCN is peaked at ~ 543 nm and the peak of the photocurrent action spectrum of a RhBSCN monolayer coated p-CuSCN photocathode which corresponds to the first peak of Fig.7-2, occurs at ~ 554 nm. A red-shift of ~ 11 nm is a consequence of bonding the dye to the substrate surface. However, the peak of the action spectrum of the photocathode of the optimally thick film (46 monolayers) appears at ~ 632 nm. The large red shift (78 nm) indicates J-aggregation and such structures have large exciton diffusion coefficients. The mean free path of light (λ, in the dye film calculated using the extinction coefficient of Rhodamine B (1.06×10^5 mol cm^{-1}) is ~ 30 nm. At monolayer coverage, injection of holes from the excited dye molecules anchored to the CuSCN surface generates photocurrent. When the thickness of the dye film exceeds mean free path of light (λ), light cannot reach the CuSCN/dye interface and the photocurrent is generated by the following process (Fig. 7-3). Photons absorbed by the bulk of the dye create excitons which diffuse and decompose at the CuSCN/dye interface releasing holes to p-CuSCN and electrons to the dye. The positioning of HOMO of Rhodamine B and the valence band edge of CuSCN permits the above process. Rhodamine B being an electron mobile (n-type) material [127] transports the electron to the electrolyte interface where it is accepted by tri-iodide.

The variation of photocurrent with the dye film thickness (as shown in Fig. 7-1) can be understood as follows. As dye coverage increases from zero, excited dye molecules anchored to surfaces, inject electrons increasing the photocurrent until a monolayer thickness is reached. When next 1-2 monolayer begin to form, light cut-off from first monolayer reduces the photocurrent , as thickness further increase exciton process takes over until limited by the exciton diffusion length. A simple one-

dimensional model presented below explains the variation of the excitonic photocurrent with the film thickness.

If Φ_P = photon flux incident on film surface [Fig. 7-2(b)], the flux at a distance x in the film is Φ_P exp(- x/λ) (λ = mean free path of light) and light absorbed in an element of the film the of thickness dx = (Φ_Π /λ)exp(- x/λ)dx . In a one-dimensional model a half of excitons created in the element will travel forward and other half in the backward direction and getting reflected at the front (dye/electrolyte) interface. Thus photocurrent element *dI* generated from the excitons created in the dye and incident on the dye/p-CuSCN interface can be stated by,

$$dI = \frac{e\Phi_P \Pi_P \Pi_D (1+r)}{2\lambda} e^{-x/\lambda} [e^{-(L-x)/\Lambda} + re^{-(L+x)/\Lambda}] \qquad \text{(Eq. 7-1)}$$

Where, Λ = exciton diffusion length, Π_P = probability of exciton creation by light absorbed , Π_D = exciton decomposition probability at the CuSCN/dye interface, r = exciton reflection fraction at the dye/electrolyte interface. Integrating Eq.7-1, for $\Lambda > \lambda$.

$$I \approx \frac{e\Phi_P \Pi_P \Pi_D}{2} e^{-L/\Lambda} [1 - e^{-L/\Lambda}] \qquad \text{(Eq. 7-2)}$$

The Eq. 7-2 is maximum when L= Λln2 and giving $\Lambda = 112.6$ nm. Thus the existence of a second maximum in the curve of Fig. 7-2 (a) is explained enabling estimation of the exciton diffusion length. As the photocurrent reaches a negligibly small value when the film is ~ 75 monolayers, corresponding to a film thickness of ~ 128 nm, the value of Λ estimated from the model agrees reasonably well with the photocurrent measurement.

The D.C electrical conductivities and electron mobilities of RhCl, RhBSCN and a J-aggregated film of RhBSCN measured at 25^{o}C are given in Table 7-1. Conductivity and electron mobility are nearly three orders of magnitude higher in the organized film. Molecular arrangement as in Fig. 7-1, greatly enhance the exciton diffusion length as well as the electron mobility.

Table 7-1: D.C electrical conductivities and electron mobilities of Rhodamine B Chloride (RhBCl), Rhodamine B Thiocyanate (RhBSCN), and a J-aggregated film of Rhodamine B thiocyanate grown over a CuSCN surface.

	σ /Scm^{-1}	μ_e /cm^{2}V^{-1}S^{-1}
RhBCl	~ 10^{-8}	~ 10^{-6}
RhBSCN	3 x10^{-7}	~ 10^{-6}
RhBSCN(J-aggregate)	7x 10^{-4}	8 x 10^{-2}

The photocurrent action spectrum of the heterojunction n-Cu_2O/J-aggregated RhSCN /p-CuI obtained by transmitting light through CuI is shown in Fig. 7-4. The narrow profile of the photocurrent action spectrum peaked at 632 nm and red-shifted 89 nm from the absorption peak of the dye solution, indicate J-aggregation. The curve C of Fig. 7-4 is action spectrum of n-Cu2O/p-CuI. It is interesting to note that the photocurrent arising from Cu_2O band gap excitation (the broad profile peaked at 480 nm in the curve A of Fig. 7-4) is greatly enhanced in presence of the dye. This can be understood as suppression of surface recombination by the absorbed dye which passivates the Cu_2O surface. In dye-sensitized solar cells, the dye plays a key role in suppressing recombination via passivation of the surface[128].

Table 7-2: IV characteristics of different heterojunctions

Heterojunction	**Isc ($mA\ cm^{-2}$)**	**Voc (mV)**	**FF**	**η %**
n-Cu_2O/p-CuI	2.1	370	0.41	0.32
n-Cu_2O/RhBSCN (monolayer) /p-CuI	3.2	390	0.50	0.62
n-Cu_2O/RhBSCN (J-aggregate) /p-CuI	3.8	423	0.56	0.90
n-TiO_2/RhBSCN(J-aggregate)/p-CuI	0.4	486	0.43	0.08

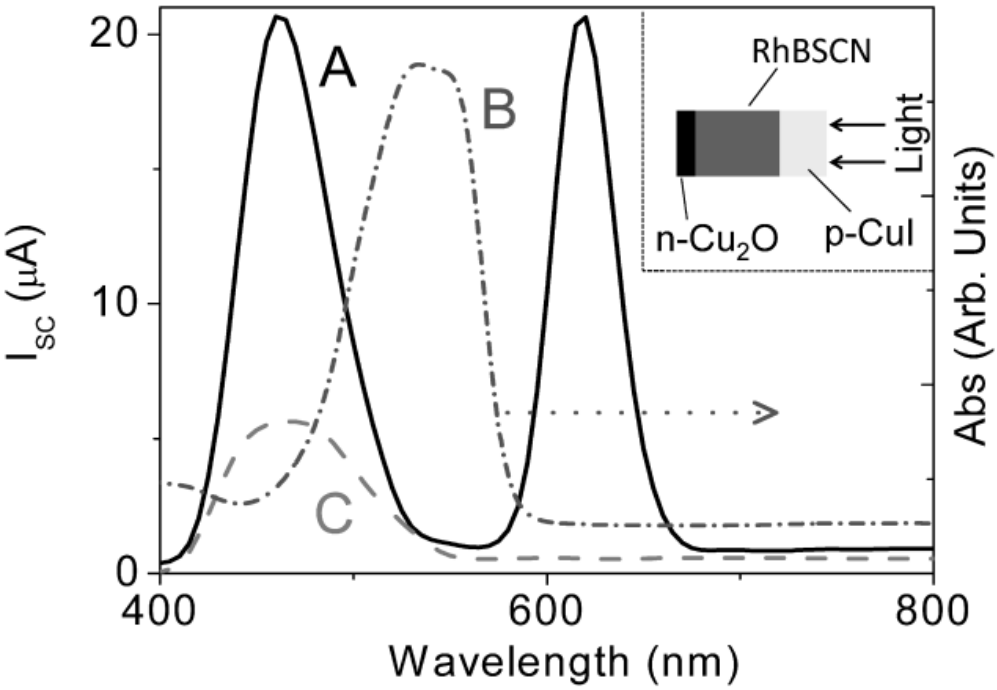

Figure 7-4: A- Photocurrent action spectrum of a n-Cu_2O/J-aggregated RhBSCN/p-CuI heterojunction shined with light as indicated in the inset (for clarity contacts to cell are not shown). The narrow peak to left in the curve A originate from light absorption by the dye and the broad peak is Cu_2O band gap excitation. B - Absorption spectrum of aqueous RhBSCN. C - Photocurrent action spectrum of n-Cu_2O/p-CuI.

Current-Voltage characteristics of different heterojunctions examined are summarized in Table 7-2. The highest I_{sc} and η are obtained for the cell n-Cu_2O/J-aggregated RhBSCN/p-CuI with a RhBSCN film approximately ~ 29 monolayers thick. The monolayer thickness here is less than the optimum film thickness in the PECs with J-aggregated RhBSCN coated CuSCN photocathode. The reason for this behaviour appears to be the difference in the interfaces where exciton decomposition and reflection take place. However, quantitative analysis of problem has not been successful. In the n-Cu_2O/J-aggregated RhBSCN/p-CuI system excitons decomposing at the RhBSCN/p-CuI interface contribute to the photocurrent injecting electrons to RhBSCN and holes p-CuI and excitons decomposing at n-Cu_2O /RhBSCN interface cannot contribute to the photocurrent as RhBSCN is n-type . The low Voc of all the heterojunctions based on n-Cu_2O is due to interference of the Cu/n-Cu_2O contact as n-Cu_2O is deposited on metallic copper. The cell n-TiO_2/J-aggregated/RhBSCN/p-CuI delivers a higher Voc, but the I_{sc} is low due to poor contact at the interface n-TiO_2/RhBSCN formed by pressing a TiO_2 coated FTO glass plate onto to the dye film.

Thiocyanate of Methyl Violet and several other cationic dyes demonstrated the same behavior in forming highly organized J-aggregated films on copper based substrates[129]. A notable exception is Acridine Orange thiocyanate (ACSCN) deposited on CuSCN surface by the same procedure as RhBSCN. The absorption spectrum of an aqueous solution (~10^{-3} M) of ACSCN peaks at ~ 490 nm. However, the photocurrent of an ACSCN coated CuSCN phtocathode reaches the maximum at 460 nm, indicating this dye forms H –aggregates when adsorbed on CuSCN. Again when the variation of the short-circuit photocurrent with monolayer thickness was examined, the optimum occurred at monolayer coverage, thereafter decreasing very rapidly with the increase of the monolayer thickness [124]. The variation of the short-circuit photocurrent with ACSCN film thickness (i.e. the equivalent of Fig. 7-2 for the dye ACSCN) is shown in Fig. 7-5. Generally H-aggregates do not facilitate exciton transport[130] and the cathode with a thick ACSCN film cannot deliver photocurrent via the exciton mechanism

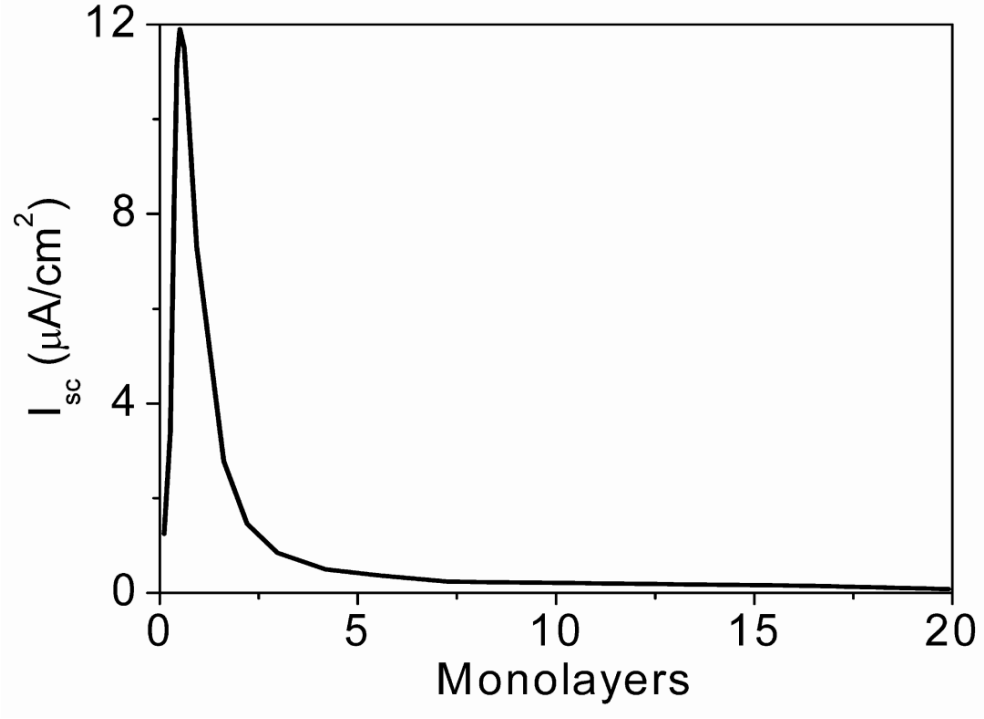

Figure 7-5: Variation of the short-circuit photocurrent (Isc) of ACSCN coated p-CuSCN photo-cathode in iodide/tri-iodide electrolyte (Illumination 250 Wm^{-2}, Tungsten filament lamp)

7.4 Conclusion

The above study demonstrates that highly organized films of thiocynates of cationic dyes can be deposited on copper based substrates by controlled absorption from a solution. The mechanism involved is strong S-bonding of SCN- ion to Cu sites and repetitive attachment of dye cations and SCN- ions alternatively to yield a thick film of organized structure. Thiocyanates of Rhodamine B, Methyl Violet and several other dyes deposited in this manner exhibited J-aggregation behaviour with widely red-shifted

narrow absorption bands. Large exciton diffusion lengths of the order of 100 nm were evident from photoelectrochemical measurements and molecular organization has also enhanced the electron mobility. The purity of the dye and absence of imperfections in the molecular architecture are important to achieve large exciton diffusion lengths and high mobilities. These parameters may be further increased by improving the purification technique and carrying out the deposition at a lower temperature. Dyes used in this study are not the best, much higher efficiencies are expected when alternative dyes of high carrier mobilities are used. Efficient exciton and carrier transport depend on dye molecular structure and organization of molecules in the film, alternative dyes and optimized film deposition techniques are expected to yield higher photocurrent quantum efficiencies. Heterojunction structures constructed indicated the potential of dye films in solar cell application as both exciton diffusion length and electron mobility are enhanced by molecular organization. Probably the system is effectively one-dimensional and such structures could exhibit directional exciton transport [131]. The above strategy of growing organized molecular films may be extended other organic cationic (anionic) dyes by appropriate choice anionic (cationic) moieties to render strong bonding to the surface of a selected material. Thiocyanate bonded to Cu sites readily act as an electron conduit. The problem establishing electronic coupling to the counterelectrode could be achieved by adhering polymer brush[132] terminated with a ligand that binds to moiety in the dye or by other similar strategies. Solar cells, NIR and IR detectors and sensors are potential applications. Chromopores absorbing in different regions of the spectrum could be organized by the same procedure to achieve panchromatic photoresponse. If the absorption and emission spectra of adjacent molecular layer overlaps, excition transport through structure is possible via Förster energy transfer.

8. CYANINE DYE-INORGANIC SEMICONDUCTOR EXCITONIC HETEROJUNCTION SOLAR CELL: SPECTRAL BROADENING VIA SIMULTANIUS H- AND J- AGGERGATES.

8.1 Introduction

Organic- inorganic hybrid nanostructures have been studied extensively as potential systems for solar cell and other opto-electronic device applications. The prototype examples of photovoltaic devices of this category are: dye-sensitized solid-state solar cells[133, 134] (DSSSCs), extremely thin absorber (ETA) cells[135] and organic-inorganic hybrid (OIH) heterostructures[89, 136]. In a DSSSC, the excited molecules in a dye monolayer sandwiched between high band-gap n- and p-type semiconductors inject electrons and holes to respective regions, generating a photocurrent. In the analogous ETA cell, where the dye monolayer is replaced by a thin film of a low band-gap semiconductor, electrons and holes created in the thin film are efficiently transferred to n- and p-type regions, provided film thickness does not exceed the carrier diffusion length [113, 137]. Organic-inorganic hybrid solar cell is basically a heterojunction of these two types of materials, where light absorbed by the organic component creates excitons that decompose at the interface, separating the charges [138]. In a thin film heterojunction, thickness of the organic film is limited by the exciton diffusion length. As the limitation of the thickness of light harvesting component restricts the overall light absorption cross-section, the performance of all the above systems are greatly improved by making the inorganic semiconductor, nanostructured to acquire a large surface area. Dye-sensitized and bulk heterojunction solar cells resorts to this strategy optimally[139]. Furthermore in excitonic solar cells, the exciton diffusion length increases greatly if the organic film has an organized molecular arrangement. Generally, an organized molecular structure in the organic film will also enhance its carrier mobility, imperative for proper functioning of the cell. An advantage of organic-inorganic thin film systems is that, they more readily afford organized molecular as-

sembly in the exciton transporting material compared to bulk heterojunction solar cells. Obviously, it is easier to build an organized molecular arrangement on a preset solid substrate (inorganic semiconductor) than to achieve such structure in a blend of two materials. This note describe an organic-inorganic hybrid solar cell of configuration n-TiO_2-[DDD----D]-p-CuSCN, where [DDD----D] is a molecularly organized thick film of a hole conducting cyanine dye electronically coupled to both TiO_2 and CuSCN. The cell exhibits photocurrents originating from exciton dissociation as well as direct dye-sensitized injection at TiO_2/dye, and dye/CuSCN interfaces. The dye assembly [DDD-----D] is found transport excitons over long distances of the order of 30 nm.

8.2 Experimental procedure

Films TiO_2 (1x1 cm^2) were deposited on fluorine conducting tin oxide (FTO) glass plates (1x 1.5 cm^2) by the method described previously for fabrication of DSSSCs [133]. Briefly, the procedure is hydrolysis of titanium isopropoxide (5 ml) in 75% propan-2-ol (15 ml) and acetic acid (5 ml) mixture to form a colloidal TiO_2 suspension. The hydrolyzed product is mixed with Degussa P25 TiO_2 powder and the viscous slurry spread over the FTO plate. The plate is heated to 120^oC for 10 min and after blowing off the loose crust of TiO_2 particles not adhered to the FTO surface, film is sintered at 425^oC for 10 min. By repetition of the process, TiO_2 film can be grown to a desired thickness. Such films are largely devoid of interconnected void channels leading the FTO surface, preventing short-circuiting at the FTO interface when a heterojunction is formed. The roughness of an 8 μm thick film estimated by adsorption of a standard dye is of the order of 500.

The cationic cyanine dye named E-65 (shown in Fig. 8-1a) was synthesized by Dr. Henary's group (Georgia State University, Department of Chemistry). The scheme shown in Fig. 8-1(a), illustrate the E-65 synthesis procedure, which admits ready variation of the auxiliary ligands[140, 141]. The polymethine precursor **1** is synthesized by reacting mucobromic acid with aniline in warm ethanol. In parallel, the

heterocyclic moiety is prepared by alkylation of 2,3,3-trimethylindolenine using bromoethanol to generate the cationic intermediate **2**. The condensation reaction between **1** and **2** proceeds effectively in the presence of acetic anhydride and sodium acetate which also affords the acylation of hydroxyl groups to yield the final compound **3** (E-65).

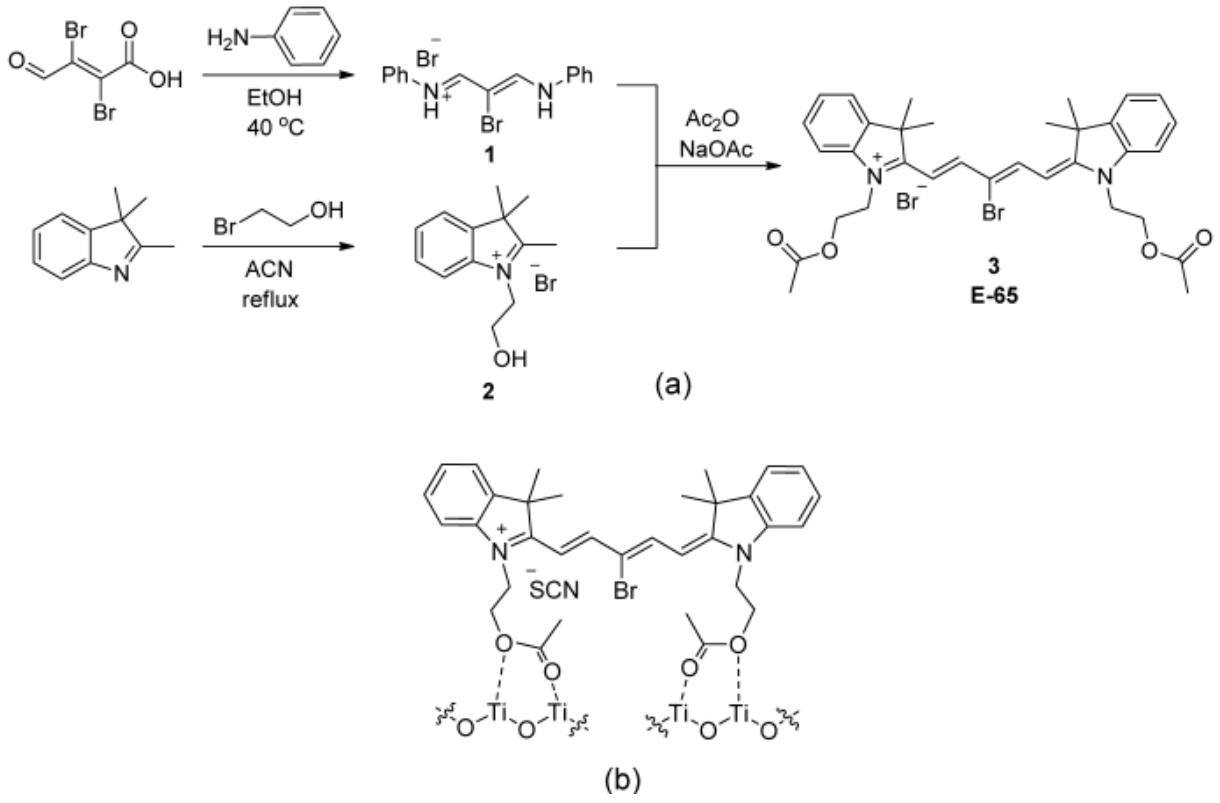

Figure 8-1: (a) The synthesis scheme of the dye E-65 and (b) its bidentate bonding to TiO2.

The dye in the bromide form is converted to the thiocyanate by boiling the dye powder in saturated solution of KSCN and separation of the dye thiocyante precipitating on cooling the solution. Dye was coated over the TiO_2 film by the following procedure. The TiO_2 film is thoroughly cleaned with alkaline 50% propan-2-ol followed by water and 99% propan-2-ol and plate dried at 120^{o}C. Dried plate is positioned vertically at the bottom of a glass tube (diameter ~ 1. 3 cm) and the dye solution (M in 90% ethanol) is poured over the plate to a height of about 4 cm. The vessel was left in a constant temperature (15 ^{o}C) environment for several days to adsorb the dye.

The monolayer thickness of the dye film was estimated by extracting dye from sample films and spectrophotometric estimation of the dye content. The film is dried in air at ambient temperature and p-CuSCN deposited over its surface from a solution in n-propyl sulfide. The back electrode is formed by pressing a FTO glass plate to secure the contact. Painting graphite over the CuSCN surface improves the back contact. However, for comparison of the cell performance in front-wall (light incident on TiO_2) and back-wall (light incident on CuSCN) modes of illumination, graphite painting was avoided. Photocurrent action spectra and I-V characteristics of the cells were recorded using a source meter and a monochromator set-up.

The carrier mobility of the dye was determined by measuring the space-charge limited current. For this measurement, vacuum dried dye is pressed into a thin pellet between two stainless steel electrodes in a glass tube and connected to a d.c voltage, sufficient to obtain a measurable current avoiding degradation of the material due to heating. Mobility is calculated from the Mott-Gurney equation,

$$J = \frac{9\varepsilon\mu V^2}{8L^3} \qquad \text{(Eq. 8-1)}$$

where J = current density, μ = mobility , ε = dielectric constant, V = applied voltage , L = pellet length.

The sign of the charge carrier was ascertained by field-assisted thermoelectric tests using the same experimental set-up. Alternative heating of two electrodes and noticing direction of biasing which yields a higher current in the circuit enables determination of the sign of carrier. Method does not require heating of the electrodes to an excessive temperature as in direct thermoelectric tests. FTIR spectra of dye lightly coated to TiO_2 and the non-adsorbing substrate GaAS were recorded to ascertain the mode bonding the dye to TiO_2.

8.3 Results and Discussion

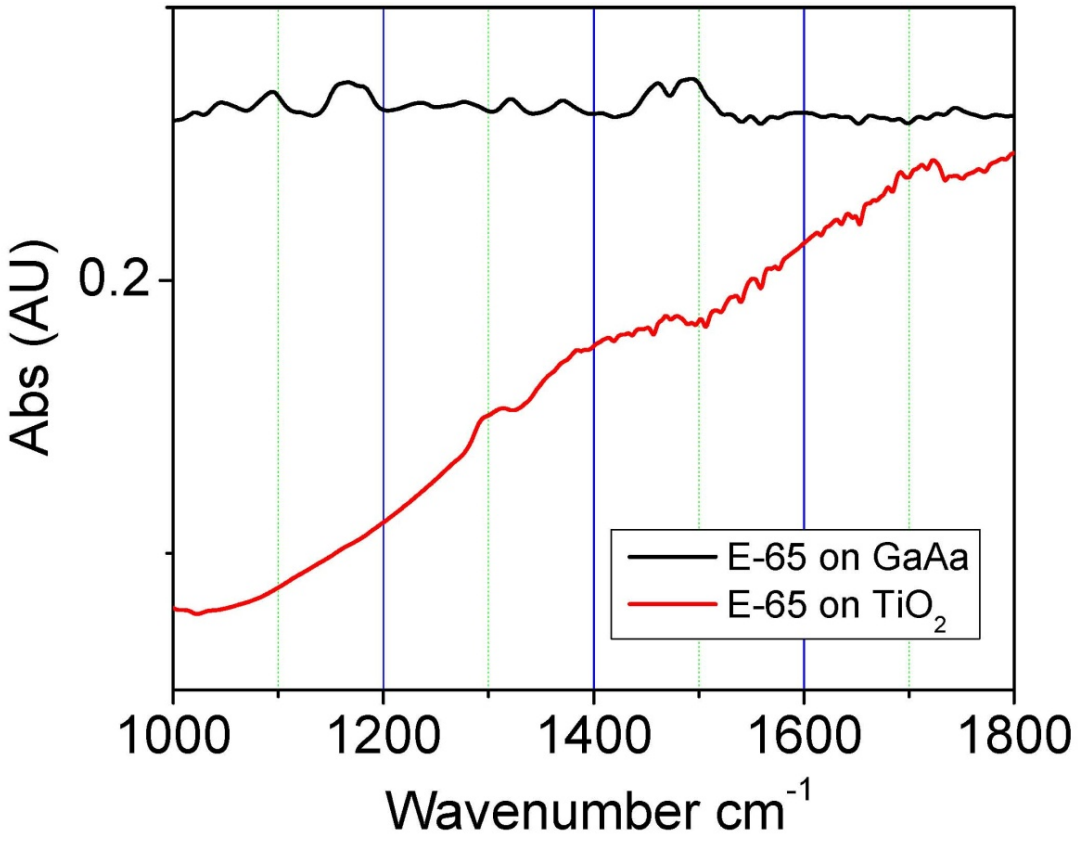

Figure 8-2: The FTIR spectrum of the dye deposited on GaAS wafer, nanocrystalline TiO2 film are shown in the Fig.4 below. The annihilation of absortion peaks in the range 1000 cm-1 to 1250 cm-1 with E-65 adsorbed on TiO2 implies bidentate bonding of E-65 on to TiO2.

When the TiO_2 film is exposed to a relatively dilute (~ 10^{-3}M) solution of the dye for 30-45 min, the dye coverage approximates to a monolayer formed by chelation of dye molecules to the TiO_2 surface. The two functional groups in the dye anchor bidentately to TiO_2 as shown in Fig. 8-1(b). Comparison of the FTIR spectra of the dye adsorbed TiO_2, bare dye and bare TiO_2 shows changes in the characteristic C-O-H bending and C-O-H stretching vibrations[142] in the region suggestive of dye binding to TiO_2 in this manner. The absence of the C-O-H bending band at ~ 1100 cm^{-1} and drastic reduction in the C-O-H stretching band at 1738 cm^{-1} in the dye adsorbed onto TiO_2, as can be seen in Fig. 8-2, indicate bidentate bonding of the dye.

In more concentrated solutions (> 0.05M), the first monolayer forms almost instantly by surface chelation of dye cations and electrostatic bonding of the SCN anions (Fig. 8-3(a)). The subsequent slower growth of dye film proceeds as consecutive bonding of dye cations and SCN anions via dipole-ion and electrostatic forces respectively (Fig. 8-3(b)). An initial fast absorption to form a monolayer and subsequent slow assembly has also been observed in J-aggregate formation on metallic[143] and other semiconductor substrates[139].

The firm anchorage of the first monolayer serves as a template for growth of an organized film. Slow evaporation of the solvent during storage (determined by ambient temperature and height of the air column and diameter of the tube) assist maintenance of dye concentration at a sufficient level to continue the film growth via forward progress of dye adsorption, i.e.

$$X^+ + SCN^- \leftrightarrow [XSCN]_{ab}$$

where X^+ denote the dye cation and $[XSCN]_{ab}$ dye molecules adsorbed onto the substrate. Obviously incorporation of SCN^- into the solution by addition of KSCN, accelerates the film growth via common ion effect. Highly organized J or H aggregated films of ionic dyes can be deposited by the above technique.

Nature of the dye and substrate and deposition conditions determines the type of the aggregation (i.e. J, H or a mixture of J and H) and extent of disorder.

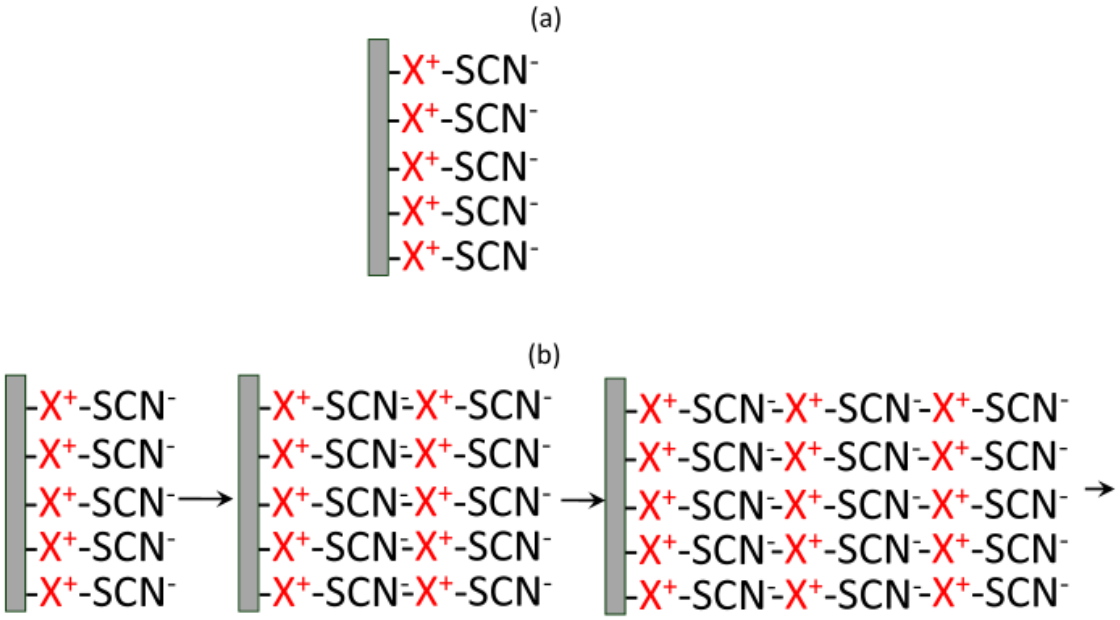

Figure 8-3: (a) Formation of the first monolayer of dye on TiO2 by surface chelation of the dye cation X+ and electrostatic bonding of SCN- (b) subsequent growth of the film via bonding of dye cations and SCN anions by ion-dipole and electrostatic forces.

A schematic diagram illustrating construction of the cell and an element of the heterojunction interface are shown in Fig. 8-4. Bonding of the functional groups of the dye, anchors it firmly to TiO_2, facilitating the necessary electronic coupling. As sulfur in SCN readily binds to Cu sites in solid copper compounds [122, 123, 139], the electronic coupling of the organized dye film to the hole collecting CuSCN is also secured.

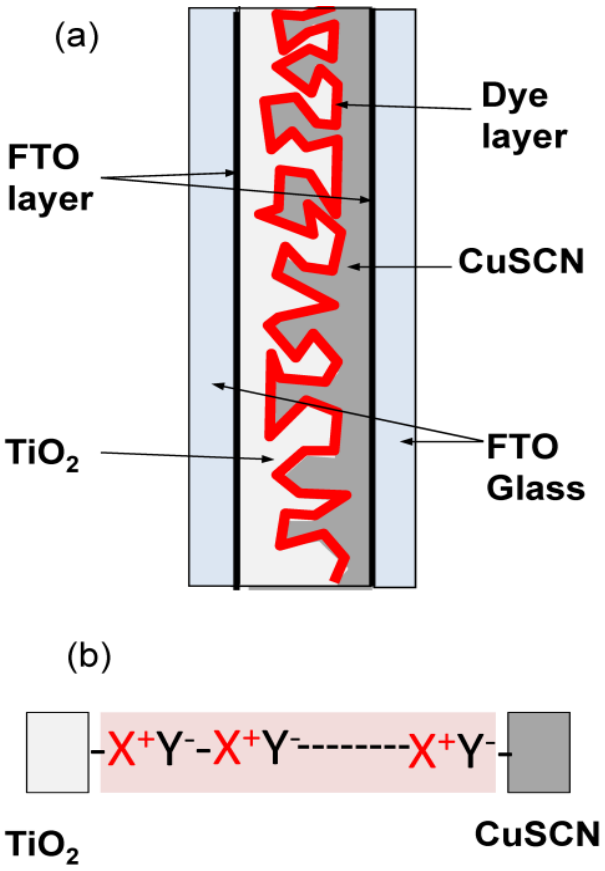

Figure 8-4: Schematic diagram indicating (a) construction of the cell and (b) an element of the TiO2/dye/CuSCN interfaces schematically depicting coupling of the organized dye aggregate to TiO2 and CuSCN.

The short-circuit photocurrent density (J_{sc}) depended on the thickness of the dye film and in both front and back wall modes of illumination, J_{sc} was found to be optimum in films much thicker than one monolayer, contrary to familiar dye-sensitized solar cells where the best photo-response is generally seen at monolayer coverage of the dye. The observed effect in the thick film can be understood as a result of a significant excitonic contribution to the photocurrent.

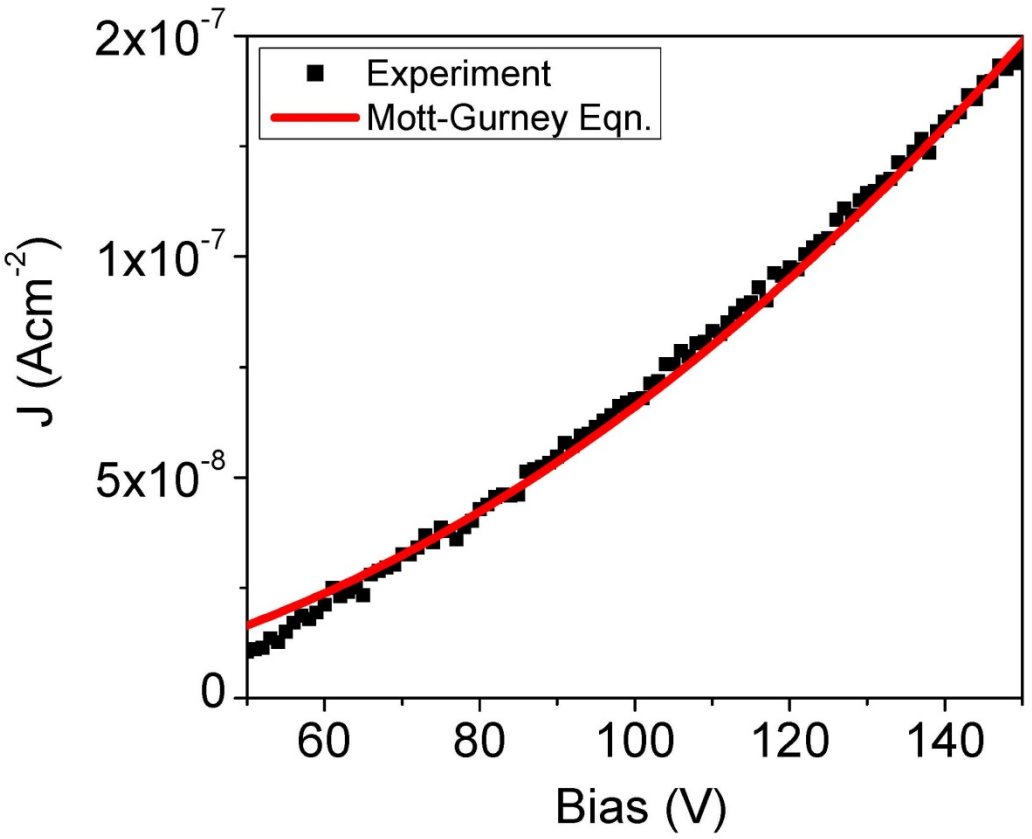

Figure 8-5: J-V characteristic curve and Fitted line of Mott-Gurney Eqn. Mobility is calculated from measurement the space charge limited current using solid dye pressed between stainless steel electrodes (pellet length L = 1.1 mm, diameter = 1 mm). The dye powder used for this experiment was dried in vacuum at ~100 ^{O}C for 24 hours. The plot of current density J vs applied bias V

Like most cyanine dyes solid E-65 exhibits hole conduction[127], with a carrier mobility significantly high compared to familiar dyes. Possibly, the Br atom in methane chain acts as an electron acceptor realizing holes. The measurement of the variation of the space charge limited current with voltage bias is in good agreement with eq. 8-1, as shown in Fig. 8-5, giving a mobility $\mu = (7.2 \pm 1.4)$ x 10^{-3} cm^2 V^{-1}s^{-1}. Mott - Gruney measurement is highly sensitive to moisture and thermoelectric injection, hence they can ob-

scure the measurement. The errors can be greater at higher voltages, and at low voltages the parabolic curve looks like linear. The Mott-Gruney measurement is not a refined measurement, but very frequently used in organic electronics for estimating mobilities. The chi-square value with a quadratic fit is 0.99; while a linear fit gives 0.96 implies quadratic fit (Mott-Gurnay Equation fit) is more accurate.

When the cell is illuminated, HOMOs of dye molecules bonded directly to TiO_2 excite electrons to LUMOs and transfer them to conduction band of TiO_2 as in a normal DSSSC. As the dye is a p-type conductor, the hole released is transported along the thick dye layer to CuSCN. Again the excitons generated in the bulk decompose at the TiO_2/dye interface separating electrons and holes to TiO_2 and dye respectively and holes are transported across the dye layer to CuSCN. The photocurrent action spectra of a cell with thick (~ 11 monolayers) dye film, in front and back wall modes of illumination are presented in Fig. 8-6. Both spectra have profiles extending from 500-775 nm with distinct differences. The front wall spectrum has a peak at 681 nm red-shifted from the absorption spectrum of the dye solution by ~ 31 nm. The cause of this peak is more intense direct sensitization at the TiO_2/dye interface combined with the excitonic contribution from light adsorbed in the bulk of the film. Whereas the back-wall spectrum displays a peak at ~706 nm with a narrow profile red-shifted by 56 nm and a largely broadened blue-shifted peak structure at ~ 579 nm. It is interesting note that the back wall spectrum also displays a peak at ~ 635 nm corresponding to direct sensitization at the dye/CuSCN interface. The back-wall mode spectrum could be understood as an effect originating from presence of J and H aggregated domains in the dye film. J-aggregates have narrow and red-shifted absorption peaks compared to the monomer[144]. H-aggregates display the opposite behavior with broadened and blue-shifted absorption peaks[144]. In the front-wall mode, this effect is partly masked by the contribution to the photocurrent from direct sensitization by the monomer anchored to the TiO_2 surface. In the back wall mode, light incident on TiO_2/dye interface is not sufficiently intense to mask the photocurrent generated by excitons produced in the bulk of the thick film and decomposing at the TiO_2/dye interface and injecting electrons

to TiO_2 and conducting holes to CuSCN. A cell with a monolayer thick dye film shows no distinction in front and back wall action spectra, both have peaks at ~ 650 nm , almost same as the peak absorption of dye in solution (Fig. 8-7). Again if the thick dye film of similar thickness is deposited by drop coating of the dye over the warmed TiO_2 film instead of slow growth as in the previous experiment, the photo-current action spectra in front and back wall modes do not demonstrate conspicuous distinction and the observed photo-response is weaker. Clearly the organized molecular assembly of the dye has been cause of the observed distinction in front and back wall action spectra and the enhanced photo-response. Fig. 8-8 shows the I-V curves of cells with organized and disorganized thick dye layers and a monolayer. I-V parameters and peak wavelengths of the action spectra of different cells are summarized in Table 8-1.

Table 8-1: I-V parameters and peak photoresponse wavelengths of different cells (Front–wall illumination). Grown organized- TiO_2 film soaked in the dye allowing the dye layers to grow slowly by interaction forces in the molecules. Drop coated- Thick dye layer is spared on the TiO_2 film (dye layers will be disorganized). η-efficiency.

Dye Film	I ($mAcm^{-2}$)	V (mV)	η %	λ_{Max} (nm)
Organized Dye	2.3	374	0.4	687
Drop coated (disorganized)	1.1	331	< 0.15	675
Monolayer	0.3	350	< 0.05	658

A severe problem in conventional DSSSCs is recombination at the points where inorganic n- and p-type semiconductors are in direct contact. Imperfections in the dye monolayer frequently lead to this situation lowering the efficiency. In the present system, the thick dye layer naturally resolves this prob-

lem. It is important to note that distinction in the charge transfer processes originating from light absorbed by the first monolayer anchored to TiO_2 and those in the bulk of the thick film. The bonding of the dye to TiO_2 creates a charge transfer complex and kinetics of electron transfer from a dye molecule in the monolayer is a characteristic of the entirety of dye molecule and the charge transfer complex. Whereas light absorbed by dye molecules in the bulk emit exctions which decompose at the TiO_2 /monolayer interface. There is evidence that such interfaces involving charge transfer couplings efficiently decompose excitons and the mobility of the hole in the J-aggregate suppresses back electron transfer[145].

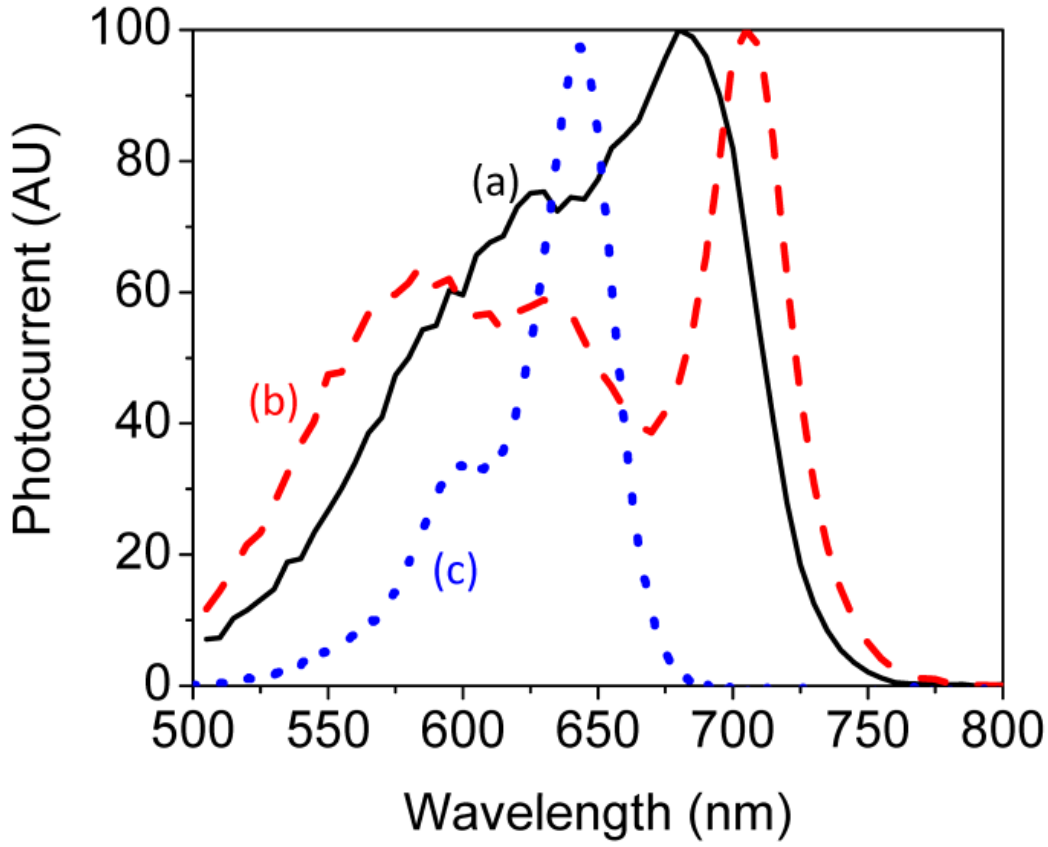

Figure 8-6: Normalized photocurrent action spectrum of the cell with a thick dye film (a) front-wall illumination (b) back-wall illumination and (c) absorption spectrum of 0.001M solution of the dye.

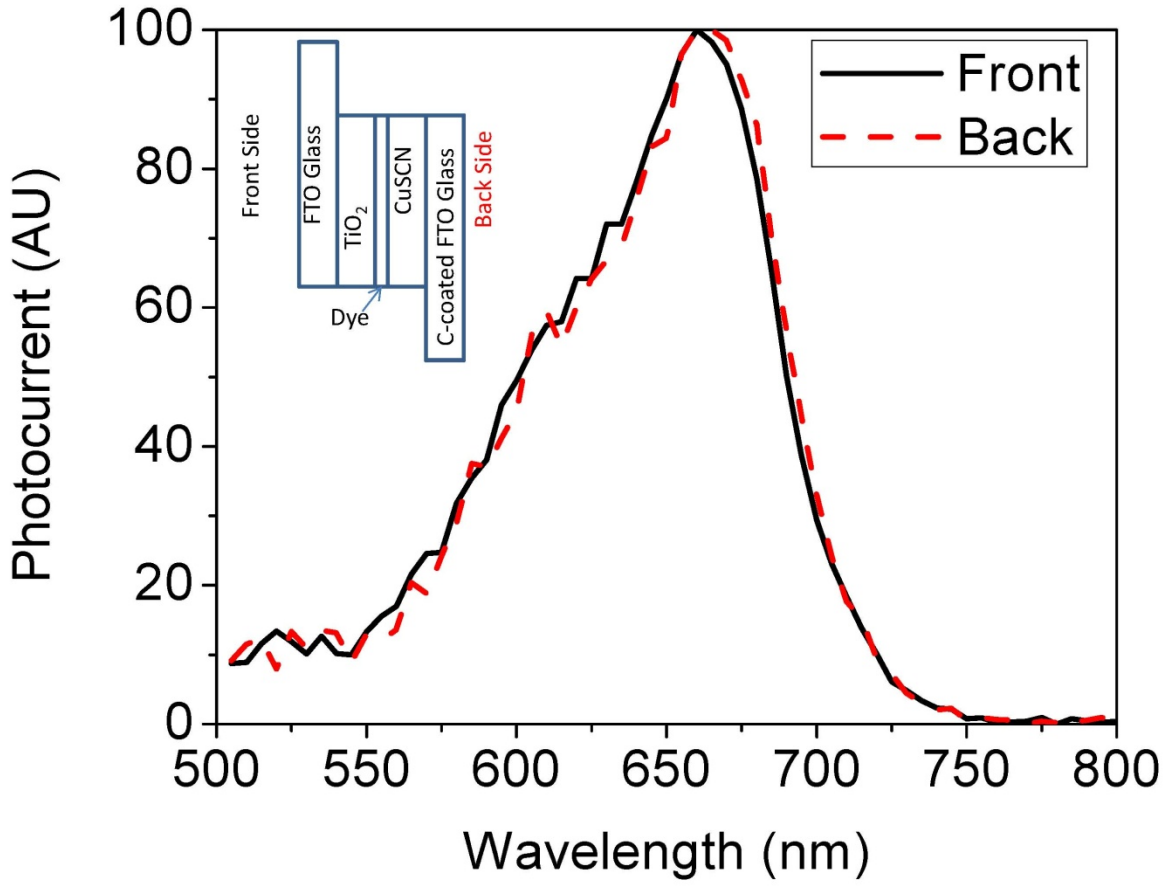

Figure 8-7: Normalized photocurrent action spectrum of a cell with a dye-monolayer in front and back wall modes. Front: Device illuminated from TiO_2 side. Back: Device illuminated from CuSCN side.

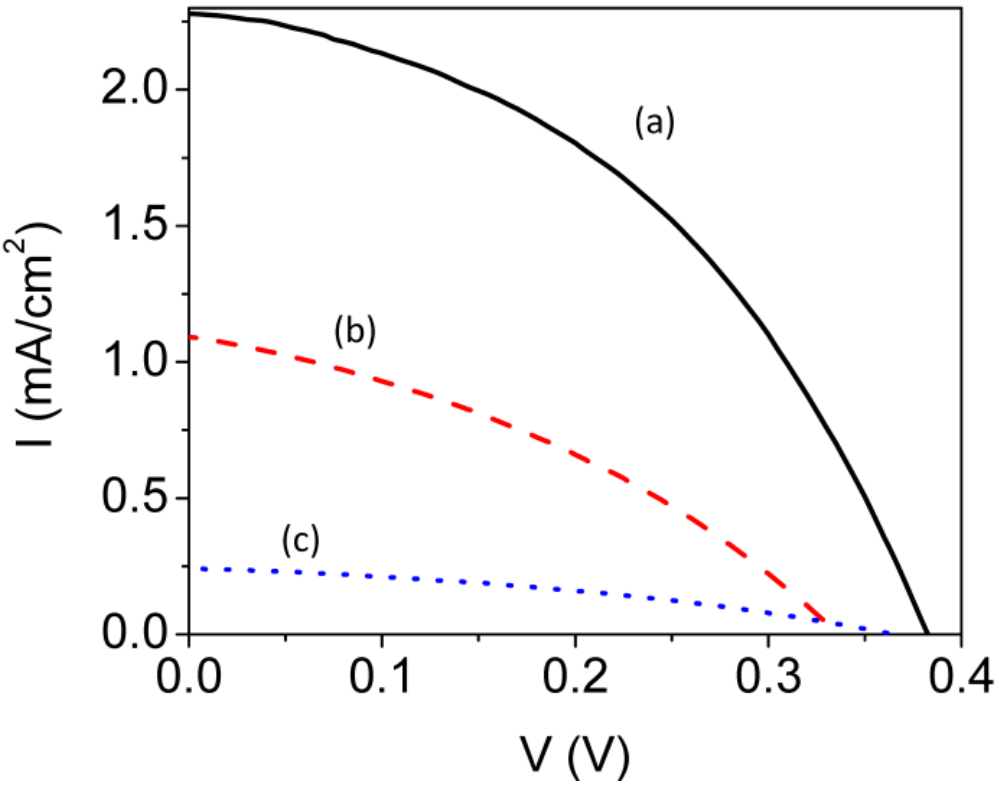

Figure 8-8: I-V curves of the cells with (a) organized thick dye layer (b) disorganized thick dye layer (c) dye monolayer (Front wall illumination)

We have not yet succeeded in elucidating the morphological arrangement of J and H domains in the dye film. The simultaneous occurrence J- and H-aggregates has been reported in solid films with other dyes[146]. Two possibilities exist, i.e. regions composed entirely of either J or H aggregates connecting the two surfaces (TiO_2 and CuSCN) or separated distributions across the thickness of the film. The latter morphology is somewhat detrimental to cell performance, for the following reason. During J-aggregation HOMO is moved upwards and LMUO downwards relative to their positions in the monomer, agreeing with observed red-shift in absorption spectrum [105, 147]. The opposite would happen in an H-

aggregate, as this form molecular assembly leads to a blue-shift in absorption [105, 147]. Consequently, electron or hole transfer from an H to a J-region is permitted, but not the reverse. Thus an H-aggregated region in the middle of J-aggregate connecting TiO_2 and CuSCN would impede carrier transport. The dye E-65 deposited on TiO_2 is predominantly J-aggregated. The Br atom in the methine chain seems to enhance J-aggregation by facilitation of appropriate molecular stacking. A cyanine analogous to E65 without a halogen atom in the methine chain was found to prefer H-aggregation when deposited on TiO_2 by the same procedure. The fact the action spectrum display greatly blue shifted broad peak confirms that excitons generated in the H-aggregated regions also participate in photocurrent generation, implying the presence of H-aggregated domains connecting TiO_2 and CuSCN interfaces.

The film thickness dependence of the photocurrent can be understood as: If, Φ_p = photon flux incident on TiO_2/dye interface (front-wall mode), flux at a distance x from the interface is $\Phi_P \exp(-\xi/\lambda)$, where $\lambda =$ mean free path of light. The exciton flux emanating from light absorbed in this element is $\lambda^{-1}\Pi_P\Phi_P \exp(-x/\lambda)dx$, where Π_P = probability that an excited dye molecule will emit an exciton (Fig. 8-9).

If a one dimensional model is assumed[138], half of excitons generated will travel in the backward direction and strike TiO_2/dye interface. The other half of excitons travelling in the forward direction will get reflected at dye/CuSCN and the strike back on the dye/TiO_2 interface. In contrast, instead of reflection, excitons could also decompose at this interface injecting holes to CuSCN. Therefore, the photocurrent dI generated by the light absorbed in the element dx can be written as,

$$dI = \frac{\Phi_P \Pi_P \Pi_D}{2\lambda} \exp\{-x/\lambda\}[\exp\{-x/\Lambda\} + R.\exp\{-2L/\Lambda\}]edx \qquad \text{(Eq. 8-2)}$$

Where $\Lambda =$ exciton diffusion length, L = thickness of the dye film, e = electronic charge, Π_P = probability of an exciton created by absorbed light, and Π_D = probability of an exciton decomposing and injecting electrons to TiO_2 and holes to CuSCN, R= excition reflection coefficient at the dye/CuSCN interface.

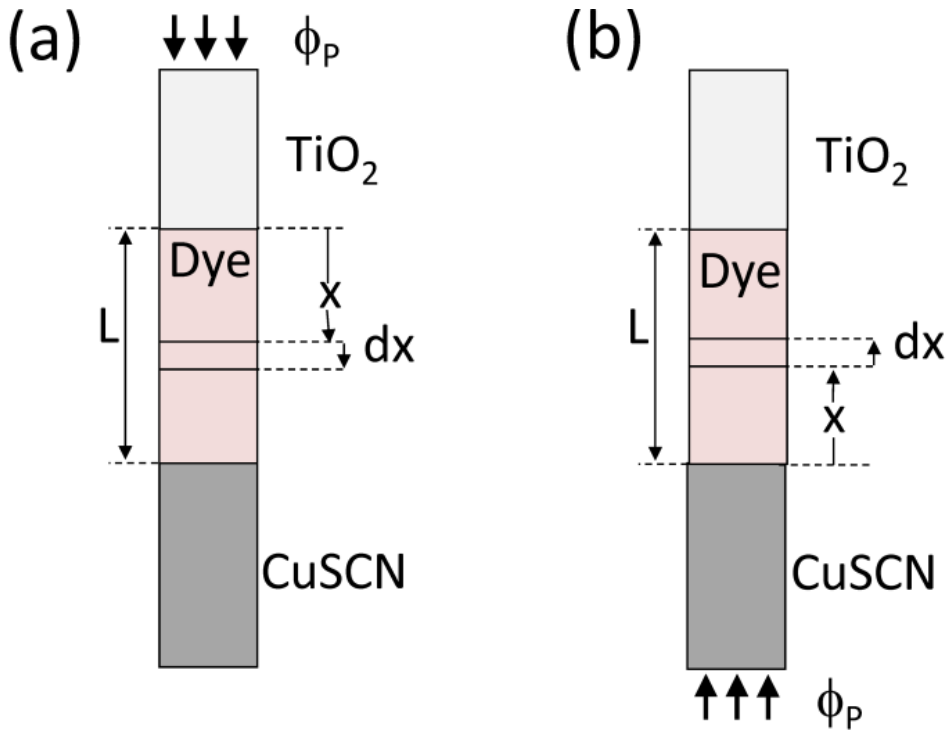

Figure 8-9: Geometry of the (a) front and (b) back wall illumination

However, as the dye is not conducting electrons, holes will recombine with electrons residing in the dye at the interface. Integrating (8-2), the photocurrent (*I*) is calculated as,

$$I \approx \frac{\Phi_P \Pi_P \Pi_D}{2}[1 + R.\exp\{-2L/\Lambda\}][1 - \exp\{-L/\Lambda\}]e \qquad \text{(Eq. 8-3)}$$

In the approximation $\Lambda > \lambda$. Total photocurrent is obtained by adding the contribution from direct sensitization by dye monolayer anchored to TiO_2, which is independent of L. Similarly, the back wall mode photocurrent (Fig. 8-9b) can be expressed as,

$$I = \frac{\Phi_P \Pi_P \Pi_D}{2}(1 + R)[\exp\{-L/\Lambda\}][1 - \exp\{-L/\Lambda\}]e \qquad \text{(Eq. 8-4)}$$

Here, the photocurrent decrease more rapidly after film thickness reaches a maximum when $L \sim \lambda[\ln(\Lambda/\lambda)]$. Knowledge of the extinction coefficient dye yield $\lambda \sim 16.6$ nm and as the photocurrent is found to be optimum when the film is 11 monolayers corresponding to film thickness of ~11 nm, we obtain $\Lambda \sim 32$ nm.

8.4 Other dyes tested for J-/H- aggregations.

During the study 15 additional dyes were tested for their I-V characteristics and response to test the J- or H- aggregation effects. Figures 8-10 to 8-13 show absorption spectrums, response spectrums, and I-V characteristics of few of the dyes with promising results leading to further studies. A clear broadening and red shift in the response spectrum compared to the dye absorption spectrum can be seen in the results. Further experiments with the mobility calculations and study with varying multi-layers are needed to study the performance variations with J and H aggregates of the compounds, and it will lead to understand possible modifications needed in the dye molecules for further improvements to utilize them as a feasible photon detector or a solar cell. Furthermore, a study on improving the stability of the device is also important.

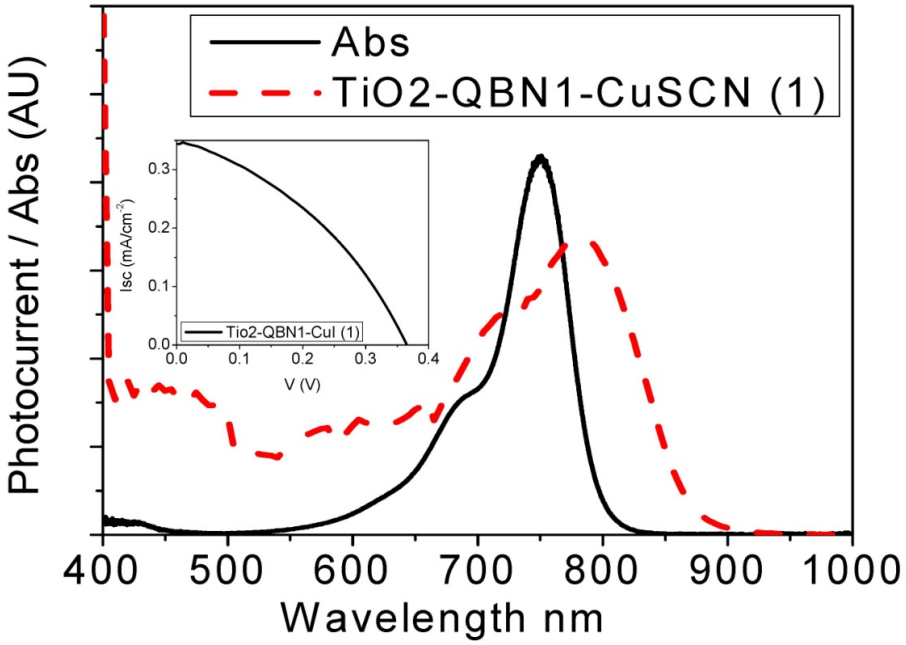

Figure 8-10: Absorption spectrum (solid line), response spectrum (dashed line) and I-V curves (inset) of the dye QBN-1

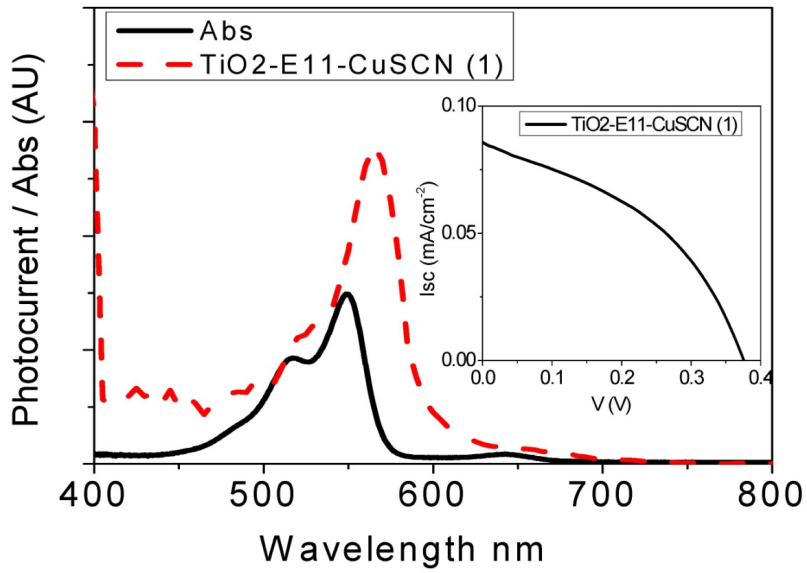

Figure 8-11: Absorption spectrum (solid line), response spectrum (dashed line) and I-V curves (inset) of the dye E11

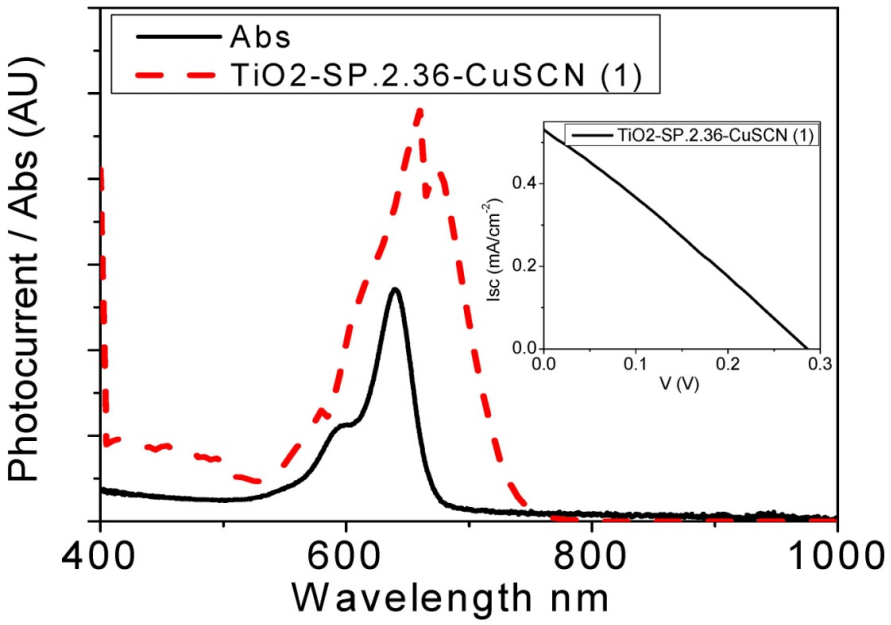

Figure 8-12: Absorption spectrum (solid line), response spectrum (dashed line) and I-V curves (inset) of the dye SP.2.36

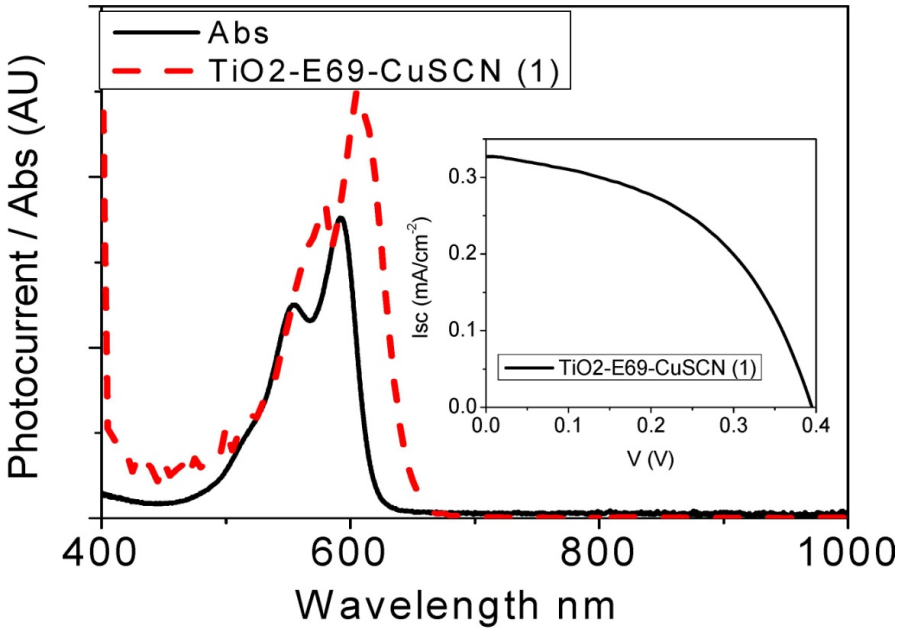

Figure 8-13: Absorption spectrum (solid line), response spectrum (dashed line) and I-V curves (inset) of the dye E69.

8.5 Future work

As can be seen in the Fig. 8-14, the difference in the structure E-11 (IV, response and absorption data shown in Fig. 8-11) and E-65 is the –[CBr=C]- group in the center of the molecule. This difference in the two compounds has resulted in lower photocurrent in the DSSC sensitized with E-11, ~ 80 μAcm^{-2}, compared to ~ 300 μAcm^{-2} observed with E-65. It will be interesting to study the mobility and effects of the extra –[CBr=C]- group on the performance of a photon detector.

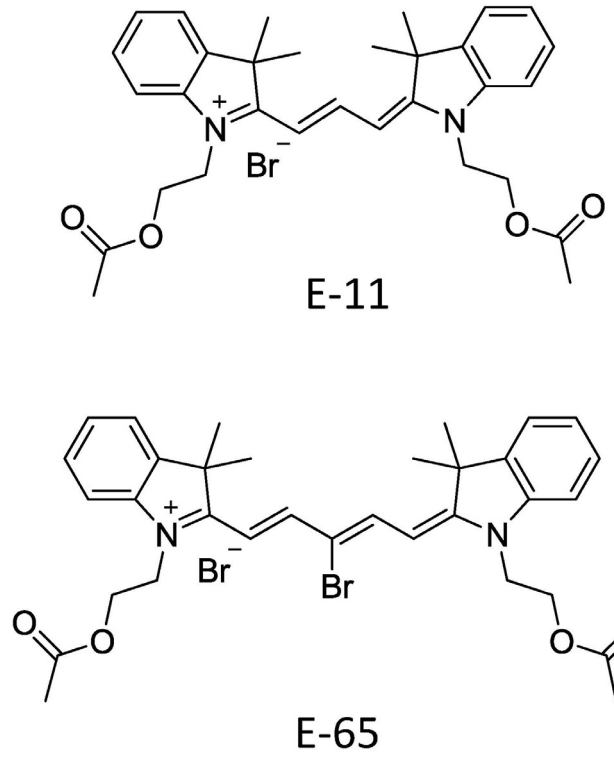

Figure 8-14: The molecule structure of the dye E-11 and E-65.

Additionally, new set of compounds, named as PTN-11, PTN-12 and PTN-13, shown in Fig. 8-15, with the modified heterocyclic units compared to E-11 and E-65, expect to increase the hydrophobicity of the dye hence expected to change the aggregation properties. Additionally, the extra rings in the compounds red-shifts the maximum absorption wavelength by approximately 20 nm. Comparison of the DSSC performance with these compounds will provide further information on effects of the halogen group in the dye molecule, on the DSSC performance and excitonic transport in the compounds.

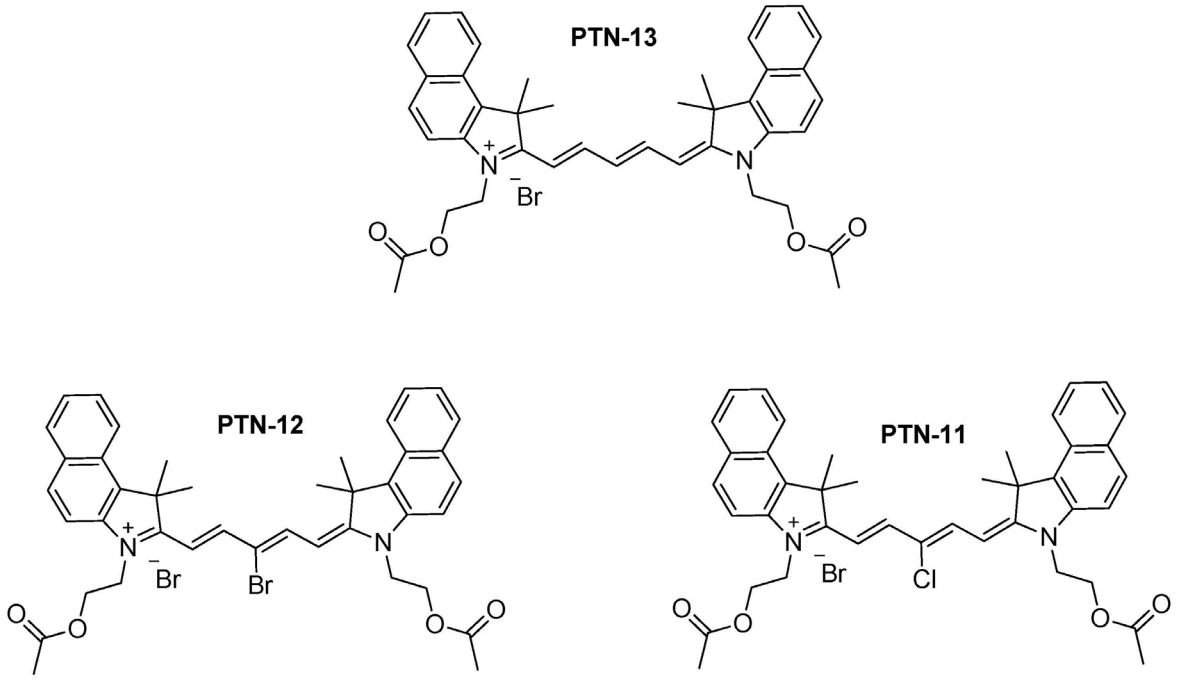

Figure 8-15: The molecule structure of the dyes PTN-11, PTN-12 and PTN-13.

8.6 Conclusion

A pentamethine cationic cyanine dye with two functional moieties binding to TiO_2 and a Br atom in the methine chain is synthesized. The functional moities surface chelate bidentately to n-TiO_2 establishing strong electronic coupling to the conduction band states. Bonding of dye to p-CuSCN is facilitated by replacement halide anion by thiocyanate. Nanocrystalline TiO_2 films exposed to a solution of dye under ambient conditions by mere control of solvent evaporation rate, admits deposition of predominantly J-aggregated thick films exhibiting fast exciton diffusion and detectable hole mobility. Model solar cell of the configuration n-TiO_2-[DDD---D]-p-CuSCN with the thick organized dye film [DDD----D] demonstrate contributions to the photocurrent originating from excitons generated in bulk of the thick film and direct sensitized injection at the TiO_2/Dye interface. Low efficiency of the cell is attributed to insufficient hole mobility of the dye and/or exciton recombination at the interface. More stringent purification of the dye and improvement of film deposition technique to eliminate H – aggregated domains will improve the efficiency. However, in order to attain orders of magnitude enhancement of the mobility, understanding of the mechanism of hole conduction and how it relates to the dye structure would be necessary to aim synthesis of more prospective dyes.

9. PbS QUANTUM DOT EMBEDED NANOSTRUCTUR WITH UV-IR RESPONSE

9.1 Introduction

Possible strategies to broaden the spectral response of a DSSC would be to use a mixture of dyes with different chromospheres covering the required spectral range [148, 149] or use J- or/and H aggregate of dyes with organized accumulation (as shown in Chapters 7 and 8). However, all dyes do not have the organized accumulation properties required for application in above methods, hence will lead to thick layer of disorganized aggregations resulting insulation or concentration quenching. Use of semiconductor material quantum dot particles to absorb photons is another method can be used in broadening the spectral response of DSSCs. Nanocrystalline films of wide-band-gap oxide semiconductors, for example TiO_2, ZnO and SnO_2, can be sensitized by quantum sized semiconductor particles such as PbS, CdS, Ag_2S, Sb_2S_3, Bi_2S_3[150]. The electron transport mechanism involved in this structure is analogous to the sensitization of wide band gap semiconductors with dyes. Size quantized band-gap modulation of QDs of low effective carrier mass enable the sensitization of wide band-gap materials from UV to far IR region [151]. Furthermore, a carrier injected in dye-sensitization can travel some distance ballistically [152] or can travel by tunneling across a thin layer of insulators or semiconductors [153-155]. Furthermore, literature states the electrons released in photo excitation of dye molecules coated on a 10-50 nm gold film, move ballistically across and enter the CB of the n-type semiconductor [156]. It also has been shown that photo-excitation of dye molecules anchored to an ultra-thin (thickness $\leq$ 1 nm) outer shells of insulators or semiconductors on a semiconductor crystallites results electron transfer to the inner core material [154, 155].

Photoconductivity of TiO_2 sensitized with PbS-QDs was reported by Hoyer et. al. [157] and ZnO is also an appealing wide-band gap semiconductor, which can be grown by MOCVD[158] or low cost sol-gel techniques[159], or spray-pyrolysis to form nanoporous films. This chapter presents two studies, (1) a ZnO film sensitized by to PbS Quantum Dots (PbS-QDs) and a dye to use as a dye sensitized solar cell

(DSSC) and (2) use of interband transitions in the PbS-quantum dot (PbS-QD) embedded ZnO as a UV-IR dual band detector.

9.2 Experimental procedure: Material Preparations

The ZnO films were prepared as briefly described below. Approximately 5g of Zinc oxide powder is ground with 0.05g of Zinc Acetate while adding few drops of acetic acid and adding sufficient ethanol to form a paste. A surfactant Triton X-100 (few drops) was added during the vigorous grinding in to the paste. More ethanol is added upto 50mL and the mixture was put in a sonicator bath for 20mins. The suspension was spread on to a preheated (150 °C) fluorine doped conducting tin oxide glass plates (1.5 x 1 cm^2, sheet resistance 12 ohm/sq) by spray pyrolisis. The film was dried at 150 °C and thereafter sintering in air at 450 ^oC for 30min, and allowed cool down to room temperature. For dye coating the ZnO films were soaked in a solutions of Acriflavine (AC, i.e., 1,6 diamino-10-methylacridinium chloride, structural formula shown in Figure 9-1) in ethanol (1M) for 24 hours.

The ZnO/PbS-Dye electrodes were made by growing a thin film of PbS quantum partials using following criteria before immersing in the dye bath. The ZnO film is wetted using a drop of (50 µl) lead (II) acetate ($Pb(CH3COO)_2 \cdot 3H_2O$) in aqueous ethanol solution and the film was exposed to H_2S gas for 30 minutes at room temperature. The film acquires a brownish-black tint due to the formation of PbS QDs. Concentration of the lead acetate and the flow rates of H_2S were adjusted to control the density and size of the PbS quantum dots. Photoelectrochemical cells (PECs) were made by clamping the dye coated (or PbS-QD embedded) film against a platinized counter electrode and filling the capillary space between the two electrodes with the I/I^-_3 electrolyte (0.6M dimethyl-propyl-imidazolium iodide + 0.5M t-butyl pyridine in methoxy-acetonitrile). Figure 9-1 shows a schematic diagram of the cross section of the device.

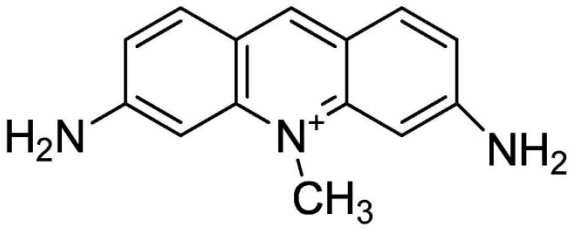

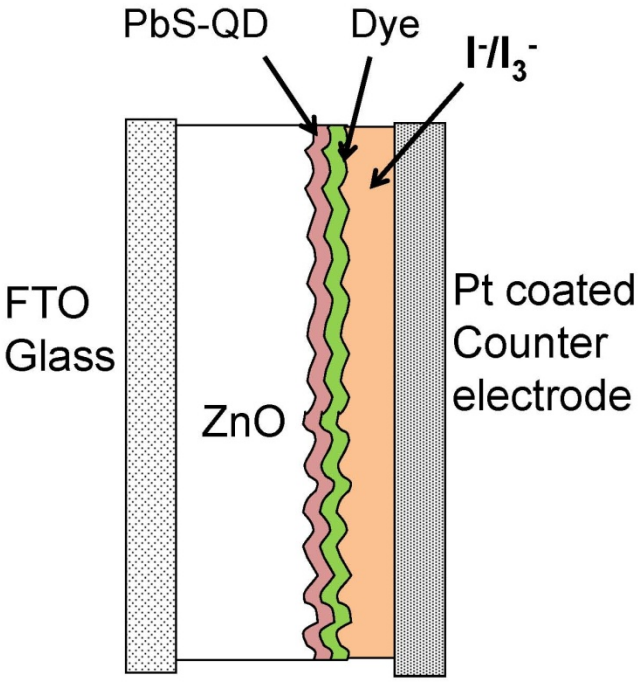

Figure 9-1: Schematic diagram of Acriflavine (AC, i.e., 1,6 diamino 10 methylacridinium chloride). And a schematic diagram of the cross section of the Dye Sensitized Solar Cell fabricated on a ZnO film and sensitized by a thin film of PbS quantum dots and Acriflavin dye.

SEM images of FTO glass plates coated with ZnO and ZnO/PbS-QDs were obtained using a Hitachi S-4800 SEM at 2 kV. The IV characteristics of the samples were measured using a KEITHLEY 2400 source meter. A UV-VIS-NIR monochromator, lock-in amplifier and a chopper system with higher order cutoff filters were used to obtain the spectral response. The intensity of the monochromatic light was determined using a calibrated Si and an InGaAs photodiodes

A custom-designed Kratos Axis Ultra X-ray photoelectron spectroscopy system [160] was used to obtain the X-ray photoelectron spectroscope (XPS) spectra of the PbS-QD embedded ZnO film. All XPS spectra were calibrated using the adventitious Carbon (C) 1s peak, at 285.0 eV. A Shirley-type background was subtracted from each spectrum to account for inelastic scattered electrons that contribute to the broad background. The CasaXPS software was used to process the XPS data[161].

9.3 Results and Discussion

SEM image of a ZnO film is shown in Figure 9-2(a) and the Figure 9-2(b) shows the ZnO films with PbS-QDs on it. The average diameter of the QDs in Fig. 9-2(b) is estimated to be 14 ± 2 nm. The results are in agreement with the absorption spectra of PbS-QDs in polymer films, reported by Wang et al [42], and band gap energy of PbS-QDs calculated using the finite depth potential model[162].

XPS spectra do not show any shift in binding energies Zinc-2p and Oxygen-1s upon deposition of PbS-QDs on ZnO, indicating that PbS-QDs are not chemically attached to the ZnO surface. Therefore, it is assumed that PbS-QDs are anchor on to ZnO surface via Van der Waals forces. In ZnO/PbS-QD samples, two XPS peaks appear at 161.5 and 160.3 eV that corresponds to S 2p region (Fig. 9-3(a)). These peaks assigns to the Sulpur-$2p_{1/2}$ and Sulpur-$2p_{3/2}$ transitions respectively[163]. The low binding energies of these two peaks suggest that Sulpur exists as sufide, i.e. as PbS but not as either sulfate or sulfite, i.e. $PbSO_4$ or $PbSO_3$, which routinely have Sulpur-2p binding energies above 167.0 eV. XPS spectra taken at

the beginning (Fig. 9-3(a)) and after one week (Fig. 9-3(b)) indicated oxidation of PbS into $PbSO_4$ and $PbSO_3$. Response degradation with time is observed due to this oxidation process of PbS.

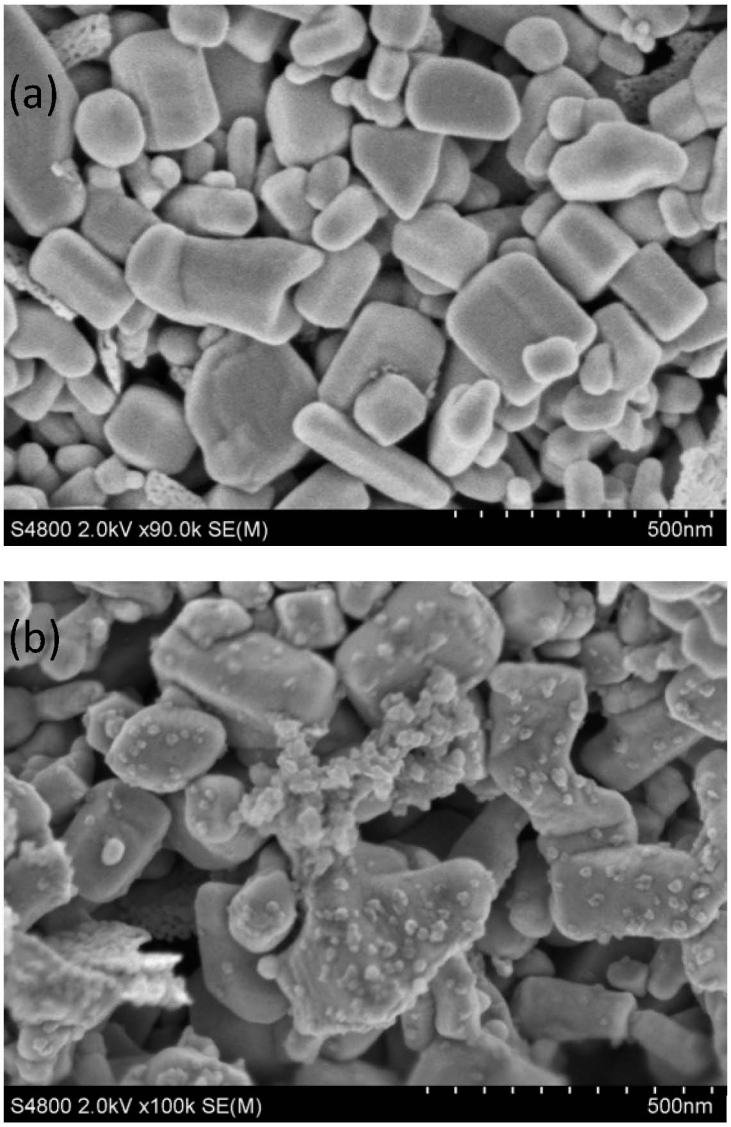

Figure 9-2: SEM images of (a) CTO plate coated with ZnO and (b) CTO plates coated with PbS-QDs. Average QD size was estimated as 14±2 nm.

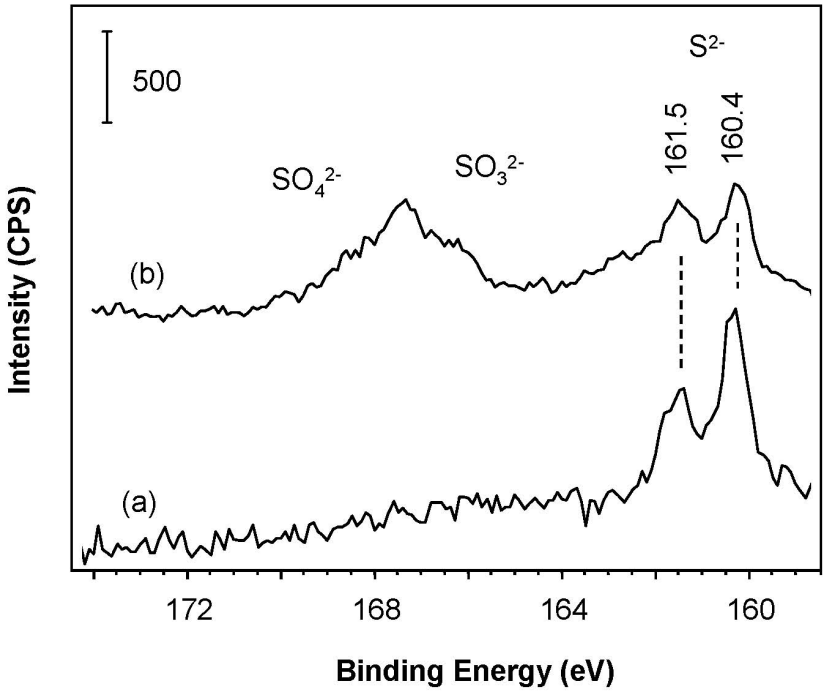

Figure 9-3: The XPS spectra of the ZnO/PbS-QD sample (i) Freshly prepared sample (ii) After expo-sure of sample plate to ambient atmospheric conditions for one week.

The XPS spectra, not showing any evidence of having $Pb(OH)_2$ or $Pb(CH_3COOH)_2$. Since we are using $Pb(CH_3COOH)_2$ and H_2S to make PbS-QDs, it is highly unlikely to form $Pb(OH)_2$, but it is possible to form when exposed to humid conditions for a long time. It is theoretically possible to have some unreacted $Pb(CH_3COOH)_2$ on the surface too, however in our experimental conditions a very dilute $Pb(CH_3COOH)_2$ solution is used and the surface was expose to H_2S gas for a fairly long time, to make sure that almost all the $Pb(CH_3COOH)_2$ are converted to PbS. Hence it is unlikely to contain unreacted $Pb(CH_3COOH)_2$ on the surface or $Pb(OH)_2$. The XRD Spectra did not show any significant difference between the ZnO powder and the PbS-QD embedded ZnO powder. There were literature reporting that,

the XRD peaks of nanocrystalline PbS particles are week and broad[164], therefore we were unable to observe any evidence of PbS via XPS spectra. However, the appearance of light brownish color on the ZnO film confirms the formation of PbS on the ZnO film.

9.3.1. ZnO/PbS-QD composite as a dye sensitized Solar cell

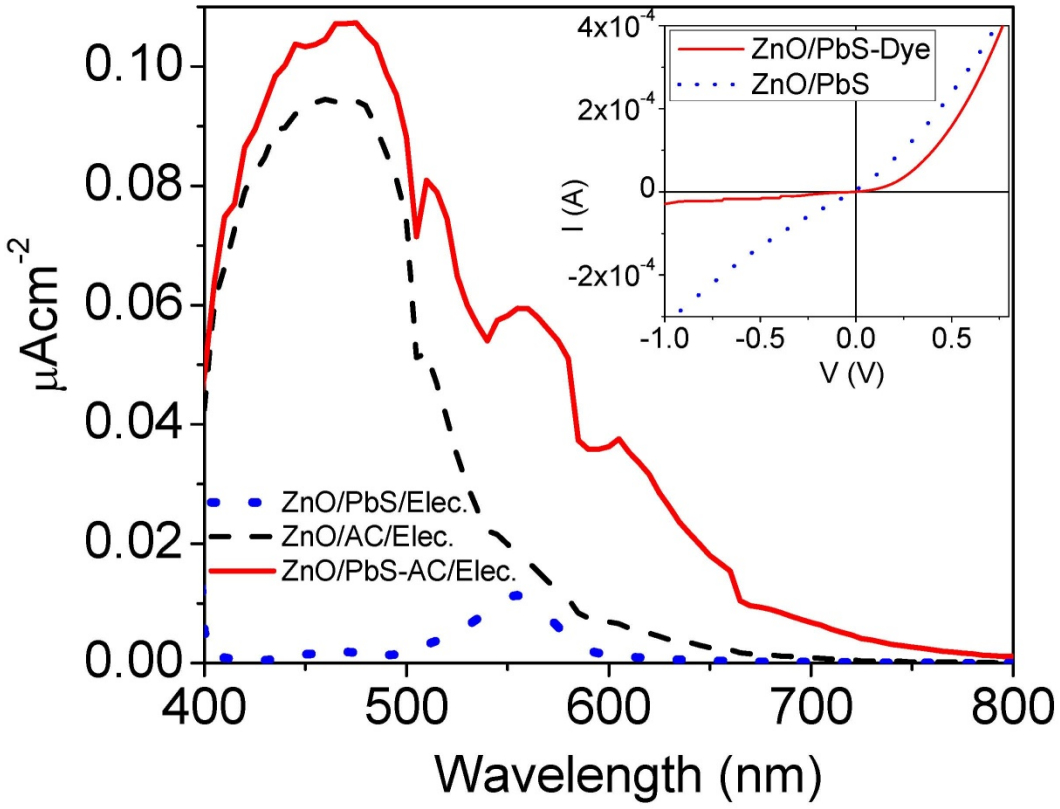

Figure 9-4: The action spectra of the three DSSC device structures (i.e., ZnO/Dye, and ZnO/PbS-Dye). Inset: The dark IV characteristics of the device structures made with combinations of PbS and Acriflavin., (i.e., ZnO/Dye and ZnO/PbS-Dye).

Inset in the Figure 9-4 shows the dark IV characteristics of the two device structures, (i.e., ZnO/Dye, and ZnO/PbS-Dye). It can be clearly seen, an improvement in the rectification factor of the device ZnO/ PbS-Dye, compared to the device with only the dye layer (ZnO/Dye). The higher dark current in the system indicates a faster combination of electrons at the interface in the ZnO/Dye structure compared to the ZnO/PbS-Dye structure. The ZnO/PbS structure showed very high leakage current in the dark IV characteristics, which may be due to the lack of uniform coverage of PbS on the ZnO film which allows short circuit paths in the junctions enabling a larger leakage current.

The action spectra of the DSSC with configurations ZnO/Dye, ZnO/PbS, and ZnO/PbS-Dye are shown in Figure 9-4. The response spectrum of device configuration ZnO/PbS-Dye, has increased in the region around 500 nm to 800 nm due to the photoexcited carriers injected by the PbS-QDs. The response of the ZnO/PbS configuration is weak as a result of ZnO been opaque to NIR; hence, the amount of NIR radiation falling onto the PbS-QDs is blocked by the ZnO film. Furthermore, the enhancement in the response in the ZnO/PbS-Dye configuration in 400- 500 nm region (compared to ZnO/Dye configuration) with the presence of PbS quantum dots is a result of the suppression of recombination of excited carriers of dye due to PbS layer acting as a barrier, and r providing a fast carrier injection path onto the ZnO film. Due to this suppression of recombination, the enhancement in photocurrent in the device configuration ZnO/PbS-Dye is larger than the total of individual photocurrents of each ZnO/Dye and ZnO/PbS configurations.

The I-V characteristics of the DSSCs under illumination with ~100mW/cm^2 Halogen light source are shown in Figure 9-5. The device with ZnO/PbS-Dye shows the maximum short circuit current of 3.2 mA/cm^2 with an open circuit voltage of ~410 mV. In the comparison, the device with only Dye and only PbS, as the absorbent, showed 2.6 mA/cm^2 and 0.32 mA/cm^2 short circuit currents and 340 mV and 380 mV open circuit voltages respectively. Table 9-1 gives a summary of the results obtained from IV characteristics.

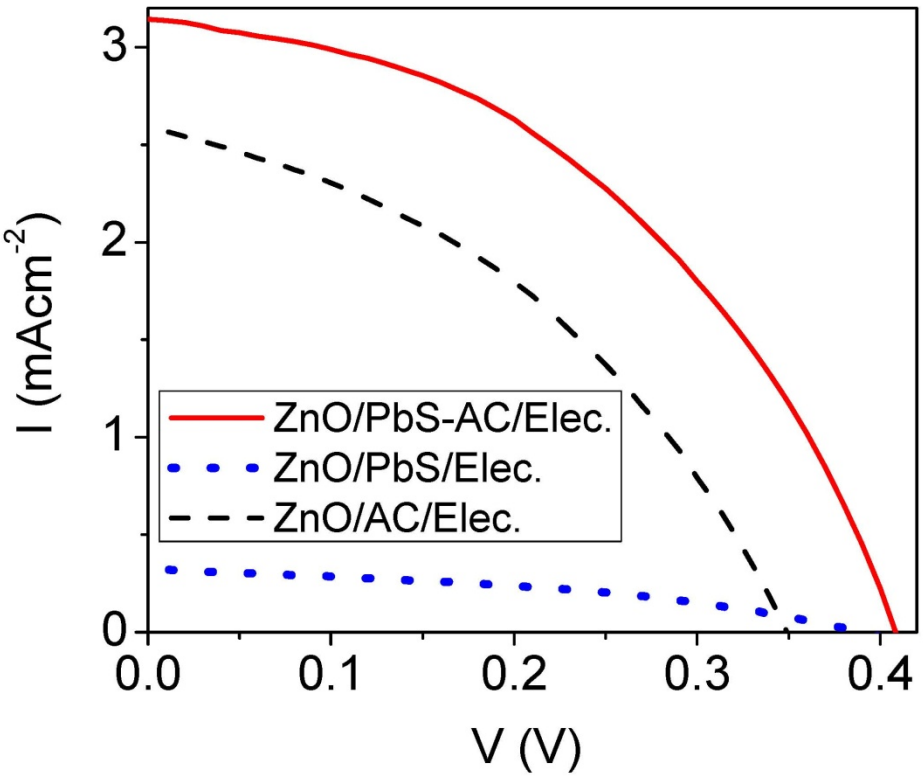

Figure 9-5: The IV characteristics of the three device structures (i.e., ZnO/Dye, ZnO/PbS, and ZnO/PbS-Dye) under illuminated with ~100mW/cm2 light source.

Table 9-1: Open circuit voltage (Voc), Short circuit current (Isc) fill factor (FF%) and the efficiency (Eff%) of the dye sensitized solar cell configurations with Dye and PbS quantum dots.

Description	V_{oc} (mV)	I_{sc} ($mAcm^{-2}$)	FF%	Eff %
ZnO/Dye	340	2.59	41.1	0.05
ZnO/PbS	380	0.32	41.6	0.36
ZnO/PbS-Dye	410	3.14	45.3	0.57

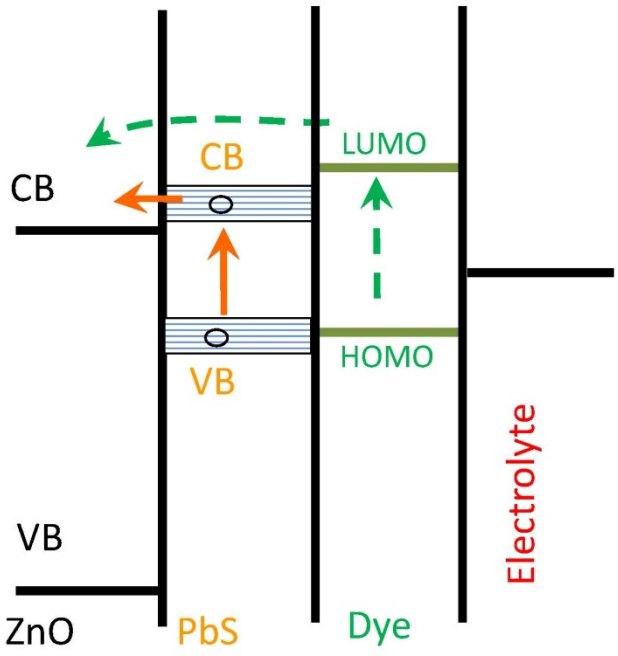

Figure 9-6: Schematic diagram of the energy bands of the device with the configuration ZnO/PbS-Dye, showing possible electron transfer mechanism through the layers.

A schematic diagram of the energy band alignment with possible electron transfer processes of the device is shown in Figure 9-6. The photons absorbed by Dye will inject an electron ballistically through the thin PbS quantum dot layer to the conduction band (CB) of the ZnO and photoexited electrons of the PbS will be injected directly to the CB of the ZnO. The hole generated at the PbS and the Dye will be filled by electrons donated by the electrolyte.

The photoresponse can be further red shifted by using larger PbS-QDs, as larger QD particles have a smaller band gap hence the absorption peak should be red shift. Larger diameter PbS quantum particles can be embedded on ZnO film by using a higher concentration of lead Acetate and by increasing the H_2S exposed time. However, with the lower band gap the band alignment will not support the electron transfer from PbS to ZnO; Therefore, arise a limitation to the maximum broadening in the response spectrum.

One drawback in the system is the fast degradation in response caused by iodide ion in the electrolyte been reacting with the PbS. Also the dye do not have proper ligands (ex. OH or COOH groups) to proper anchor on to the ZnO surface or PbS by a ionic or covalent bond, so the bonding between PbS and AC must be via Van der Waals forces.

9.3.2. ZnO/PbS Composite as a UV-IR detector

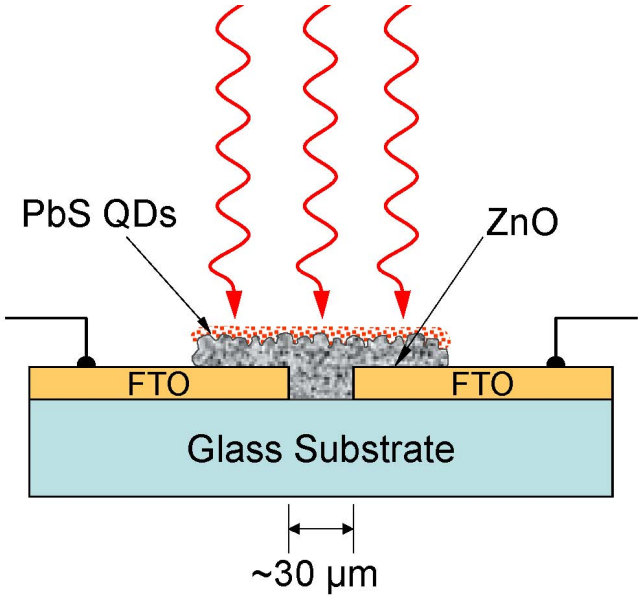

Figure 9-7 A schematic diagram illustrating sample geometry used for the dual band detector. The electrical connectivity of the FTO glass sheet was broken by engraving a scribe and a layer of colloidal ZnO embedded with PbS quantum dots were formed on top

Using the inter band transitions in the ZnO and PbS, this material combination can be used as the UV-NIR detector. The UV response will be originated from the band gap excitation of ZnO, while the NIR response will be originated by the band gap excitations of PbS-QD particles, and using an applied bias these excited carriers can be collected. A schematic of the device is shown in Figure 9-7. The device is made using fine diamond point to engrave a ~30 µm thick scribe on the surface of a FTO glass plate. The ZnO film and PbS-QDs are grown on the FTO glass as described earlier.

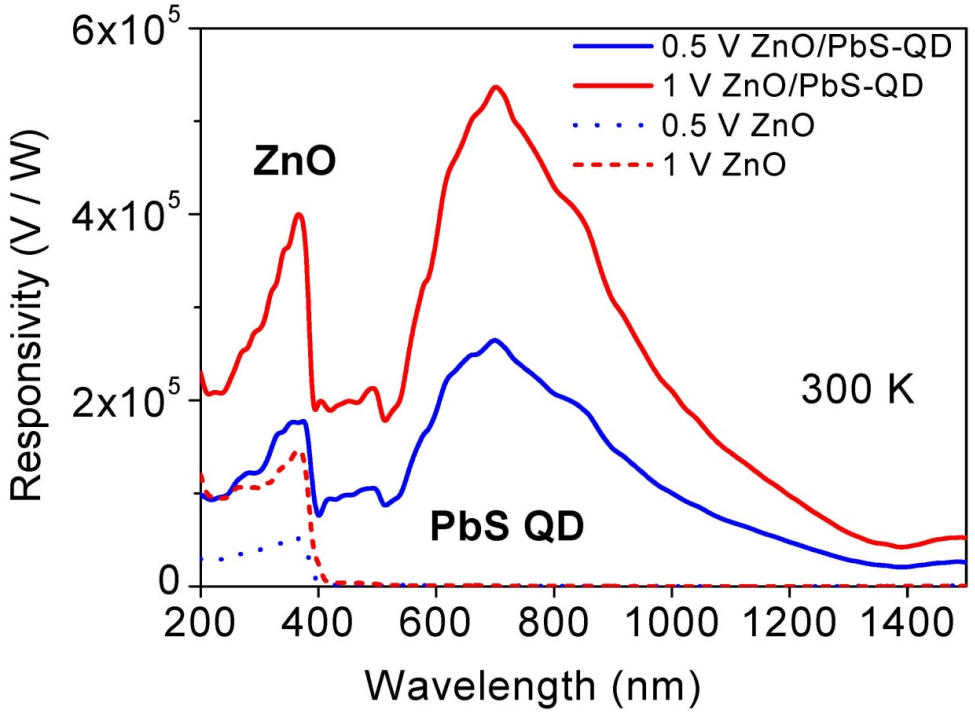

Figure 9-8 Responsivity of the PbS QD embedded ZnO dual band detector under applied biases of 0.5 V, and 1 V at room temperature. Bottom two curves (dotted lines) show the responsivity of the ZnO detector before introducing PbS QDs. As expected ZnO shows response is noticeable only in the UV region with threshold wavelength at ~380 nm, which is matched with the band gap energy of ZnO, 3.3 eV. A bias resistor of 2 MΩ was used in all measurements.

The response spectra of the device, with and without PbS-QDs, are shown in Fig. 9-8 under two different bias voltages. The bare ZnO films gave a response in the range from 200 to 400 nm with a sharp edge at 380 nm, corresponding to band-gap absorption in ZnO. For comparison, the same ZnO sample was used to embed PbS-QDs. The spectral responsivity of the PbS-QD embedded sample shows the extended response from 400 nm to 1400 nm same bias voltages. Additionally, the presence of PbS-QDs had enhanced the UV responsivity by a factor of ~ 4. The visible to near-IR (VIS-NIR) response from 500 – 1400 nm with a peak at ~700 nm clearly indicates that the VIS-NIR response is due to the PbS QDs. Since the detector is biased, larger PbS-QD partials can also transfer carries that can be collected at the contacts; therefore, the response due to PbS-QDs are further red shifted compared to the earlier DSSC. Also, presence of PbS enhance the carrier transport properties resulting enhancement in the UV photo response. All the measurements were carried out under ambient conditions. Additionally, the VIS-NIR response peak is much stronger in this structure compared to the DSSC (response in Fig. 9-4) due to the illumination from top exposing PbS-QDs to radiation, avoiding the screening from ZnO film.

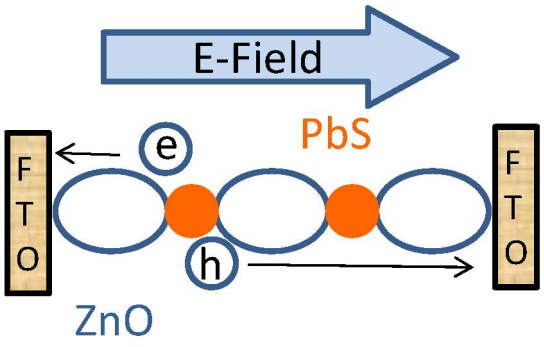

Figure 9-9 Schematic showing the carrier transport path in PbS-QD embedded ZnO. The external electric field will transport the carriers after excitation by photon absorption.

Schematic showing the carrier transport path is shown in Fig. 9-9. The excited electrons in ZnO and PbS-QDs will be transported through material length by the electric field and collected at positive electrode, while the holes will be collected at the negative electrode.

The observed response degradation with time is a result of oxidation process of PbS with exposure to air and moisture at ambient. The UV-N IR photoresponse reduced to 10% of its initial value when the sample was stored for one week under ambient conditions. Keeping the sample in vacuum can eliminate this decaying process. Therefore, for practical applications, detector should be in an airtight sealed package, which can easily achieve with a polymer sealant.

9.4 Conclusion

The investigation on DSSC shows the possibility of enhancing the performance, (by increasing photocurrent and broadening the spectral response) of dye sensitized solar cell e by adopting a thin layer of PbS quantum dots sandwiched in the DSSC structure. It also demonstrate the possibility of using the device as a multiband photodetector, as the ZnO film shows a photoresponse in the UV region in addition to the photoresponse of the PbS quantum dots. The low cost, multi-band response and easy wavelength tailorability are advantages of the device with PbS-QD embedded ZnO. SEM images confirm the different sized PbS-QDs formation on ZnO film. XPS measurements confirm the PbS formation, and oxidation stability of PbS particles. In principle, further improvement in the responsivity is possible by establishing an electronic coupling between the PbS-QDs, dye, and ZnO instead of a Van der Waals contact as in the present case.

10. CONCLUSIONS

AlGaAs structures with a graded barrier made with varying aluminum fraction demonstrated at room temperature photovoltaic response, when the Al fraction is varying from 100% to 55% a maximum photovoltaic responsivity of 450 mV/W was obtained with a detectivity (D*) of 1.2×10^6 Jones at a peak wavelength 1.8 μm. Responsivity and D* increased to ~1.2 V/W and 2.8×10^6 Jones respectively at 280 K. A non-linear improvement in responsivity was observed with increased emitter thickness.

In addition, the graded barrier has also resulted in a clear response enhancement under photo-conductive mode of operation at 77 K. Of three different methods used to grow the graded barrier named as “non-digital alloying”, “digital alloying averaging” and “digital alloying miniband” approaches, the “digital alloying averaging” approach showed around 25 times improvement in responsivity com-pared to a device without a graded barrier. Improved carrier transportation and suppression of recap-ture is believed to be the cause of the improvement.

Due to high noise in the device at 300K, the measurements not show a clear response spectrum in the photoconductive mode. The study on noise in graded barrier structure revealed that the main contribution is the shot noise originated from the dark current in the device. In addition to the shot noise, two components of generation-recombination noise were also identified. The cause of the gener-ation-recombination noise has been attributed to trap states in the GaAs emitter and AlGaAs barrier. The G-R noise components had time constants of 3.2 ms and 9.6 μs, corresponding to trap energy levels of ~0.54 eV and ~0.39 eV above the valence band. Several other trap states were identified in these structures in addition to the above. However the noise spectra did not show a significant G-R noise components resulting from carrier trapping. In addition to the shot noise and the GR noise, observed in high frequencies > 500 Hz, 1/f noise dominated in the low frequency domain. And the as the bias in-creases the 1/f noise becomes $1/f^2$ noise.

A 3×10^{18} cm^{-3}p-doped GaAs/AlGaAs multilayer hetero-junction structures with 57% Al fraction in the barrier layers were observed to have high temperature coefficients of resistance (TCR) with a value of around 4% K^{-1}, at room temperature. This is a significantly higher TCR value compared to that of VO_x or α-Si which is 2% and 2.8% respectively. Higher Al fractions and lower doping densities contribute to higher TCR. Additionally, n-doped structure has a low TCR compared to p-doped structure. The device demonstrates a bolometer like infrared (IR) response up to 20 μm with a D* of 1.7×10^{6} Jones with a low noise power, which is a requirement for good performance in a bolometer type detector.

The Burstein-Moss effect and the band gap narrowing effects were found alter the barrier height at the hetero-junction interface in GaAs/AlGaAs structures. Again it observed that the energy level alternation in the valence band due to incident light intensity, caused almost complete failure of the hetero-junction performance for small band gaps (i.e. ~ 50 meV or less), intended for long-wavelength or THz detectors especially at high temperatures.

A solar cell of configuration N-[DDD-----D]-P with a molecularly organized dye J-aggregate [DDD---D] electronically coupled to N- and P-type semiconductors is illustrated by fabricating a model device with TiO2 and CuSCN as the N- and P-type semiconductors and thiocyanate of a cationic pentamethine cyanine dye as D. The pentamethine cationic cyanine dye have two functional moieties and a Br atom in the methine chain .Two functional moieties in D anchors to TiO_2 establishing electronic coupling and serving as a template for assembly of a J-aggregated film. Bonding of sulfur in thiocyanate anion to CuSCN facilitates transfer of holes into CuSCN. The cell exhibits spectrally broad photoresponse originating from excitons generated in the bulk of the thick dye film as well as direct sensitized injection at the first interface. The dye molecular assembly is found to admit exciton transport over relatively long distances and significant hole mobility. More stringent purification of the dye and improvement of film deposition technique to eliminate H – aggregated domains will improve the efficiency. However, in order to attain orders of magnitude enhancement of the mobility, understanding of the mechanism of

hole conduction and how it relates to the dye structure would be necessary to aim synthesis of more prospective dyes.

Additionally, films of cationic dye thiocyanates adsorbed on copper based substrates form organized structures by a process of templated self-assembly. The growth process is initiated by strong S-bonding of thiocyanate ions to Cu sites, followed by repetitive and alternate bonding of dye cations and thiocyanate anions by electrostatic and dipolar forces. Rhodamine B thiocyanate and several other cationic dye thiocyanates solid films deposited this way exhibit J- aggregation behavior with large red-shifts in the absorption spectrum. Photoelectrochemical experiments with Rhodamine B thiocyanate deposited CuSCN cathodes indicated exciton diffusion lengths of order of 100 nm and space charge saturation current measurements suggested nearly three orders of magnitude enhancement of the electron mobility in the J-aggregated film. The photovoltaic properties of heterojunctions sandwiching J-aggregated dye films between n – and p-type semiconductor surfaces are investigated for potential application as solar cells and photon detectors.

REFERENCES

[1] Vincent J D, *Fundamentals of Infrared Detector Operations and Testing*. New York: John Wiley & Sons, 1990.

[2] Rogalski A and Sizov F, Terahertz detectors and focal plane arrays, *Opto-Electronics Review,* **19,** pp. 346-404, 2011/09/01 2011.

[3] Perera A G U, Yuan H X, and Francombe M H, Homojunction internal photoemission far-infrared detectors: Photoresponse performance analysis, *J. Appl. Phys.,* **77,** pp. 915-924, 1995/01/15/ 1995.

[4] Rogalski A, Infrared detectors: status and trends, *Progress in Quantum Electronics,* **27,** pp. 59-210, 2003.

[5] Martyniuk P and Rogalski A, HOT infrared photodetectors, *Opto-Electronics Review,* **21,** pp. 239-257, 2013/06/01 2013.

[6] Perera A G U, Matsik S G, Yaldiz B, Liu H C, Shen A, Gao M, Wasilewski Z R, and Buchanan M, Heterojunction wavelength-tailorable far-infrared photodetectors with response out to 70 μm, *Appl. Phys. Lett.,* **78,** pp. 2241-2243, 2001/04/09/ 2001.

[7] Komiyama S, Astafiev O, Antonov V, Kutsuwa T, and Hirai H, A single-photon detector in the far-infrared range, *Nature,* **403,** pp. 405-407, 01/27/print 2000.

[8] Cabrera B, Clarke R M, Colling P, Miller A J, Nam S, and Romani R W, Detection of single infrared, optical, and ultraviolet photons using superconducting transition edge sensors, *Applied Physics Letters,* **73,** pp. 735-737, 08/10/ 1998.

[9] Piotrowski J and Rogalski A, Uncooled long wavelength infrared photon detectors, *Infrared Physics & Technology,* **46,** pp. 115-131, 12// 2004.

[10] Rogalski A, Mohamed H, and Manijeh R, Comparison of photon and thermal detector performance, in *Handbook of Infra-red Detection Technologies*, ed Amsterdam: Elsevier Science, 2002, pp. 5-81.

[11] Whatmore R W, Osbond P C, and Shorrocks N M, Ferroelectric materials for thermal IR detectors, *Ferroelectrics,* **76,** pp. 351-367, 1987/12/01 1987.

[12] Dall'Oglio G, Melchiorri B, Melchiorri F, and Natale V, Comparison between carbon, silicon and germanium bolometers and Golay cell in the far infrared, *Infrared Physics,* **14,** pp. 347-350, 1974.

[13] Yamashita K, Murata A, and Okuyama M, Miniaturized infrared sensor using silicon diaphragm based on Golay cell, *Sensors and Actuators A: Physical,* **66,** pp. 29-32, 1998.

[14] Adachi S, *GaAs and Related Materials; Bulk Semiconducting and Superlattice Properties*. Singapore: World Csientific, 1994.

[15] Coon D D and Karunasiri R P G, New Mode of IR Detection Using Quantum Wells, *Appl. Phys. Lett.,* **45,** pp. 649-651, 1984.

[16] Jayaweera P V V, Matsik S G, Tennakone K, Perera A G U, Liu H C, and Krishna S, Spin split-off transition based IR detectors operating at high temperatures, *Infrared Physics & Technology,* **50,** pp. 279-283, 2007.

[17] Lao Y F, Pitigala P K D D P, Perera A G U, Liu H C, Buchanan M, Wasilewski Z R, Choi K K, and Wijewarnasuriya P, Light-hole and heavy-hole transitions for high-temperature long-wavelength infrared detection, *Applied Physics Letters,* **97,** pp. 091104-3, 2010.

[18] Jayaweera P V V, Matsik S G, Perera A G U, Liu H C, Buchanan M, and Wasilewski Z R, Uncooled infrared detectors for 3--5 mu m and beyond, *Applied Physics Letters,* **93,** pp. 021105-3, 2008.

[19] Kogan S, *Electronic Noise and Fluctuations in Solids*. Cambridge: Cambridge University Press.

[20] Hooge F N, $1/f$ noise is no surface effect, *Physics Letters A,* **29,** pp. 139-140, 4/21/ 1969.

[21] Kirtania A K, Das M B, Chandrasekhar S, Lunardi L M, Qua G J, Hamm R A, and Li-Wu Y, Measurement and comparison of 1/f noise and g-r noise in silicon homojunction and III-V heterojunction bipolar transistors, *Electron Devices, IEEE Transactions on,* **43,** pp. 784-792, 1996.

[22] Gillespie D T, The mathematics of Brownian motion and Johnson noise, *American Journal of Physics,* **64,** pp. 225-240, 03/00/ 1996.

[23] Blanter Y M and Büttiker M, Shot noise in mesoscopic conductors, *Physics Reports,* **336,** pp. 1-166, 9// 2000.

[24] R. J. D. Miller, G. L. McLendon, A. J. Nozik, W. Schmickler, and Willig F, in *Surface Electron Transfer Processes* ed Weinheim: VCH, 1994, pp. 167-302.

[25] Hagfeldt A and Gratzel M, Light-Induced Redox Reactions in Nanocrystalline Systems, *Chem. Rev.,* **95,** p. 49, 1995.

[26] Asbury J B, Hao E, Wang Y, Gosh H N, and Lain T, Ultrafast Electron Transfer Dynamics from Molecular Adsorbates to Semiconductor Nanocrystalline Thin Films *J. Phys. Chem. B* **105,** p. 4545, 2001.

[27] JELLEY E E, Spectral Absorption and Fluorescence of Dyes in the Molecular State, *Nature,* **138,** pp. 1009-1010, 1936.

[28] Weerasekara A, Rinzan M, Matsik S, Perera A G, Buchanan M, Liu H C, von Winckel G, Stintz A, and Krishna S, n-Type GaAs/AlGaAs heterostructure detector with a 3.2 THz threshold frequency, *Opt. Lett.,* **32,** pp. 1335-1337, 2007.

[29] Esaev D G, Rinzan M B M, Matsik S G, and Perera A G U, Design and optimization of GaAs/AlGaAs heterojunction infrared detectors, *Journal of Applied Physics,* **96,** pp. 4588-4597, 2004.

[30] Smith D L and Mailhiot C, Proposal for strained type II superlattice infrared detectors, *Journal of Applied Physics,* **62,** pp. 2545-2548, 1987.

[31] Mohseni H, Tahraoui A, Wojkowski J, Razeghi M, Brown G J, Mitchel W C, and Park Y S, Very long wavelength infrared type-II detectors operating at 80 K, *Applied Physics Letters,* **77,** pp. 1572-1574, 2000.

[32] Rogalski A and Martyniuk P, InAs/GaInSb superlattices as a promising material system for third generation infrared detectors, *Infrared Physics & Technology,* **48,** pp. 39-52, 2006.

[33] Wu C S, Wen C P, Sato R N, Hu M, Tu C W, Zhang J, Flesner L D, Pham L, and Nayer P S, Novel GaAs/AlGaAs multiquantum-well Schottky-junction device and its photovoltaic LWIR detection, *Electron Devices, IEEE Transactions on,* **39,** pp. 234-241, 1992.

[34] Kastalsky A, Duffield T, Allen S J, and Harbison J, Photovoltaic detection of infrared light in a GaAs/AlGaAs superlattice, *Applied Physics Letters,* **52,** pp. 1320-1322, 1988.

[35] Bandara K M S V, Choe J-W, Francombe M H, Perera A G U, and Lin Y F, GaAs/AlGaAs superlattice miniband detector with 14.5 mu m peak response, *Applied Physics Letters,* **60,** pp. 3022-3024, 1992.

[36] Perera A G U, Matsik S G, Pitigala D P, Lao Y F, Khanna S P, Li L H, Linfield E H, Wasilewski Z R, Buchanan M, Wu X H, and Liu H C, Effects of graded barriers on the operation of split-off band infrared detectors, *Infrared Physics & Technology,* **54,** pp. 296-301, 2011.

[37] Yi W, Narayanamurti V, Lu H, Scarpulla M A, and Gossard A C, Probing semiconductor band structures and heterojunction interface properties with ballistic carrier emission: GaAs/Al_{x}Ga_{1−x}As as a model system, *Physical Review B,* **81,** p. 235325, 2010.

[38] Debbar N, Biswas D, and Bhattacharya P, Conduction-band offsets in pseudomorphic In_{x}Ga_{1-x}As/Al_{0.2}Ga_{0.8}As quantum wells (0.07≤x≤0.18) measured by deep-level transient spectroscopy, *Physical Review B,* **40,** pp. 1058-1063, 07/15/ 1989.

[39] Watanabe M O, Yoshida J, Mashita M, Nakanisi T, and Hojo A, Band discontinuity for GaAs/AlGaAs heterojunction determined by C-V profiling technique, *Journal of Applied Physics,* **57,** pp. 5340-5344, 06/15/ 1985.

[40] Wang W I, On the band offsets of AlGaAs/GaAs and beyond, *Solid-State Electronics,* **29,** pp. 133-139, 2// 1986.

[41] Schneider H, Kheng K, Ramsteiner M, Ralston J D, Fuchs F, and Koidl P, Transport asymmetry and photovoltaic response in (AlGa)As/AlAs/GaAs/(AlGa)As single-barrier quantum-well infrared detectors, *Applied Physics Letters,* **60,** pp. 1471-1473, 03/23/ 1992.

[42] Wang Y H, Li S S, and Ho P, Photovoltaic and photoconductive dual-mode operation GaAs quantum well infrared photodetector for two-band detection, *Applied Physics Letters,* **62,** pp. 93-95, 01/04/ 1993.

[43] Larkins E C, Schneider H, Ehret S, Fleissner J, Dischler B, Koidl P, and Ralston J D, Influences of MBE growth processes on photovoltaic 3-5 μm intersubband photodetectors, *Electron Devices, IEEE Transactions on,* **41,** pp. 511-518, 1994.

[44] Matsik S G, Jayaweera P V V, Perera A G U, Choi K K, and Wijewarnasuriya P, Device modeling for split-off band detectors, *Journal of Applied Physics,* **106,** pp. 064503-6, 2009.

[45] Plis E, Annamalai S, Posani K T, Lee S J, and Krishna S, Room temperature operation of InAs/GaSb SLS infrared photovoltaic detectors with cut-off wavelength ~5 ?m, *Proc. SPIE,* **6206,** p. 62060O, 2006.

[46] Daboo C, Baird M J, Hughes H P, Apsley N, and Emeny M T, Improved surface plasmon enhanced photodetection at an Au---GaAs schottky junction using a novel molecular beam epitaxy grown Otto coupling structure, *Thin Solid Films,* **201,** pp. 9-27, 1991.

[47] Shishodia M S, Jayaweera P V V, Matsik S G, Perera A G U, Liu H C, and Buchanan M, Surface plasmon enhanced IR absorption: Design and experiment, *Photonics and Nanostructures - Fundamentals and Applications,* **9,** pp. 95-100, 2011.

[48] Casey J H C, Sell D D, and Wecht K W, Concentration dependence of the absorption coefficient for n- and p - type GaAs between 1.3 and 1.6 eV, *Journal of Applied Physics,* **46,** pp. 250-257, 1975.

[49] Trainor J and Rose K, Some properties of inn films prepared by reactive evaporation, *Journal of Electronic Materials,* **3,** pp. 821-828, 1974.

[50] Burkhard H, Dinges H W, and Kuphal E, Optical properties of In[sub 1 - x]Ga[sub x]P[sub 1 - y]As[sub y], InP, GaAs, and GaP determined by ellipsometry, *Journal of Applied Physics,* **53,** pp. 655-662, 1982.

[51] Gordon N, Lees D, Bowen G, Phillips T, Haigh M, Jones C, Maxey C, Hipwood L, and Catchpole R, HgCdTe detectors operating above 200 K, *Journal of Electronic Materials,* **35,** pp. 1140-1144, 2006.

[52] Liu H C, Dudek R, Shen A, Dupont E, Song C Y, Wasilewski Z R, and Buchanan M, High absorption ([greater-than] 90%) quantum-well infrared photodetectors, *Applied Physics Letters,* **79,** pp. 4237-4239, 2001.

[53] Pour S A, Nguyen B M, Bogdanov S, Huang E K, and Razeghi M, Demonstration of high performance long wavelength infrared type II InAs/GaSb superlattice photodiode grown on GaAs substrate, *Applied Physics Letters,* **95,** pp. 173505-3, 2009.

[54] Bhattacharya P, Su X H, Chakrabarti S, Ariyawansa G, and Perera A G U, Characteristics of a tunneling quantum-dot infrared photodetector operating at room temperature, *Applied Physics Letters,* **86,** pp. 191106-3, 2005.

[55] Plis E, Rodriguez J B, Kim H S, Bishop G, Sharma Y D, Dawson L R, Krishna S, Lee S J, Jones C E, and Gopal V, Type II InAs/GaSb strain layer superlattice detectors with p-on-n polarity, *Applied Physics Letters,* **91,** pp. 133512-3, 2007.

[56] Liu H C, Photoconductive gain mechanism of quantum-well intersubband infrared detectors, *Applied Physics Letters,* **60,** pp. 1507-1509, 1992.

[57] Mathine D L, Maracas G N, Gerber D S, Droopad R, Graham R J, and McCartney M R, Characterization of an AlGaAs/GaAs asymmetric triangular quantum well grown by a digital alloy approximation, *Journal of Applied Physics,* **75,** pp. 4551-4556, 1994.

[58] Ershov M and Korotkov A N, Noise in single quantum well infrared photodetectors, *Applied Physics Letters,* **71,** pp. 1667-1669, 1997.

[59] Rupani R A, Ghosh S, Su X, and Bhattacharya P, Low frequency noise spectroscopy in InAs/GaAs resonant tunneling quantum dot infrared photodetectors, *Microelectronics Journal,* **39,** pp. 307-313, 2008.

[60] Pitigala P K D D P, Jayaweera P V V, Matsik S G, Perera A G U, and Liu H C, Highly sensitive GaAs/AlGaAs heterojunction bolometer, *Sensors and Actuators A: Physical,* **167,** pp. 245-248, 2011.

[61] Perera A G U, Shen W Z, Ershov M, Liu H C, Buchanan M, Gunapala S D, Bandara S V, Liu J K, Ye H H, and Schaff W J, Effect of interface states on the performance of GaAs p[sup +]-i far-infrared detectors, Ottawa, Canada, 2000, pp. 597-600.

[62] Perera A G U, Silvestrov V G, Matsik S G, Liu H C, Buchanan M, Wasilewski Z R, and Ershov M, Nonuniform vertical charge transport and relaxation in quantum well infrared detectors, *Journal of Applied Physics,* **83,** pp. 991-997, 1998.

[63] Kleinpenning T G M and Holden A J, 1/f noise in n-p-n GaAs/AlGaAs heterojunction bipolar transistors:iImpact of intrinsic transistor and parasitic series resistances, *Electron Devices, IEEE Transactions on,* **40,** pp. 1148-1153, 1993.

[64] Pascal F, Jarrix S, Delseny C, Lecoy G, and Kleinpenning T, Generation-recombination noise analysis in heavily doped p-type GaAs transmission line models, *Journal of Applied Physics,* **79,** pp. 3046-3052, 1996.

[65] Makinen J, Corbel C, Hautojarvi P, Moser P, and Pierre F, Positron trapping at vacancies in electron-irradiated Si at low temperatures, *Physical Review B,* **39,** p. 10162, 1989.

[66] Williams G F, Capasso F, and Tsang W T, The graded bandgap multilayer avalanche photodiode: A new low-noise detector, *Electron Device Letters, IEEE,* **3,** pp. 71-73, 1982.

[67] Szatkowski J, Placzek-Popko E, Sieranski K, and Hansen O P, Deep hole traps in Be-doped Al[sub 0.5]Ga[sub 0.5]As layers grown by molecular beam epitaxy, *Journal of Applied Physics,* **86,** pp. 1433-1438, 1999.

[68] Mari R H, Shafi M, Aziz M, Khatab A, Taylor D, and Henini M, Electrical characterisation of deep level defects in Be-doped AlGaAs grown on (100) and (311)A GaAs substrates by MBE, *Nanoscale Research Letters,* **6,** p. 180, 2011.

[69] Szatkowski J, Sieranski K, Hajdusianek A, and Placzek-Popko E, Deep hole traps in Be-doped Al0.2Ga0.8As layers grown by molecular beam epitaxy, *Physica B: Condensed Matter,* **340-342,** pp. 345-348, 2003.

[70] Ilegems M, Properties of III-V layers, in *The Technology and Physics of Moleculer Beam Epitaxy*. **vol. 1**, Parker E H C, Ed., ed New York and London: Plenum Press, 1985, pp. 83-142.

[71] Brammertz G, Martens K, Sioncke S, Delabie A, Caymax M, Meuris M, and Heyns M, Characteristic trapping lifetime and capacitance-voltage measurements of GaAs metal-oxide-semiconductor structures, *Applied Physics Letters,* **91,** pp. 133510-3, 2007.

[72] Lagowski J, Gatos H C, Parsey J M, Wada K, Kaminska M, and Walukiewicz W, Origin of the 0.82-eV electron trap in GaAs and its annihilation by shallow donors, *Applied Physics Letters,* **40,** pp. 342-344, 1982.

[73] Bhattacharya P K, Buhlmann H J, Ilegems M, and Staehli J L, Impurity and defect levels in beryllium-doped GaAs grown by molecular beam epitaxy, *Journal of Applied Physics,* **53,** pp. 6391-6398, 1982.

[74] Hoof C V, Moor P D, Mohamed H, and Manijeh R, PolySiGe uncooled microbolometers for thermal IR detection, in *Handbook of Infra-red Detection Technologies*, ed Amsterdam: Elsevier Science, 2002, pp. 449-479.

[75] Steinhage P W and Zeyfang R R, Performance of pyroelectric detectors and vidicons based on modified Pb(Ti, Zr)O_3 ceramics, *Ferroelectrics,* **11,** pp. 301 - 304, 1976.

[76] Kruse P W, Can the 300-K radiating background noise limit be attained by uncooled thermal imagers?, in *Infrared Technology and Applications XXX*, Orlando, FL, USA, 2004, pp. 437-446.

[77] Wissmar S, Hoglund L, Andersson J, Vieider C, Savage S, and Ericsson P, High signal-to-noise ratio quantum well bolometer materials, in *Optical Materials in Defence Systems Technology III*, Stockholm, Sweden, 2006, pp. 64010N-11.

[78] Sun Y, Balkan N, Erol A, and Arikan M C, Electronic transport in n- and p-type modulation-doped GaInNAs/GaAs quantum wells, *Microelectronics Journal,* **40,** pp. 403-405, 2009.

[79] Hu M, Wu M, Lv Y, Dou Y, and Cui M, Study on thermal sensitivity of a VOx/SiO2/PS/Si multi-layer structure, *Surface and Coatings Technology,* **201,** pp. 4858-4860, 2007.

[80] Ahmed A and Tait R N, Noise behavior of amorphous GexSi1-xOy for microbolometer applications, *Infrared Physics & Technology,* **46,** pp. 468-472, 2005.

[81] Songprakob W, Zallen R, Liu W K, and Bacher K L, Infrared studies of hole-plasmon excitations in heavily-doped p-type MBE-grown GaAs:C, *Physical Review B,* **62,** p. 4501, 2000.

[82] Songprakob W, Zallen R, Tsu D V, and Liu W K, Intervalenceband and plasmon optical absorption in heavily doped GaAs:C, *Journal of Applied Physics,* **91,** pp. 171-177, 2002.

[83] Burstein E, Anomalous Optical Absorption Limit in InSb, *Physical Review,* **93,** pp. 632-633, 1954.

[84] Lahtinen J A, Electroreflectance study of the Burstein-Moss shift in indium phosphide, *Physical Review B,* **33,** pp. 2550-2553, 1986.

[85] Kleinman D A and Miller R C, Band-gap renormalization in semiconductor quantum wells containing carriers, *Physical Review B,* **32,** pp. 2266-2272, 1985.

[86] Ferreira A C, Holtz P O, Sernelius B E, Buyanov A, Monemar B, Ekenberg U, Mauritz O, Sundaram M, Campman K, Merz J L, and Gossard A C, Optical studies of acceptor centre doped GaAs/AlGaAs quantum wells, *Solid-State Electronics,* **40,** pp. 89-92, 1996.

[87] Wagner J, Photoluminescence and excitation spectroscopy in heavily doped n- and p-type silicon, *Physical Review B,* **29,** pp. 2002-2009, 1984.

[88] Gering M Z I and White K B, The Burstein-Moss shift for mercury cadmium telluride *Journal of Physics C: Solid State Physics,* **20,** pp. 1137-1145, 1987.

[89] He M, Qiu F, and Lin Z, Toward High-Performance Organic–Inorganic Hybrid Solar Cells: Bringing Conjugated Polymers and Inorganic Nanocrystals in Close Contact, *The Journal of Physical Chemistry Letters,* **4,** pp. 1788-1796, 2013/06/06 2013.

[90] Sze S M and Ng K K, in *Physics of Semiconductor Devices*, ed Hoboken, New Jersey: A JOHN WILEY & SONS, INC., PUBLICATION, 2007.

[91] Jain S C and Roulston D J, A simple expression for band gap narrowing (BGN) in heavily doped Si, Ge, GaAs and GexSi1−x strained layers, *Solid-State Electronics,* **34,** pp. 453-465, 1991.

[92] Mahan G, Energy gap in Si and Ge: Impurity dependence, *J. Appl. Phys.,* **51,** pp. 2634-2646, 1980.

[93] Zheng H Q, Wang H, Zhang P H, Zeng Z, Radahakrishnan K, Yoon S F, and Ng G I, Band gap narrowing effect in Be-doped AlxGa1−xAs studied by photoluminescence spectroscopy, *Solid-State Electronics,* **44,** pp. 37-40, 2000.

[94] Matsik S G, Rinzan M B M, Perera A G U, Liu H C, Wasilewski Z R, and Buchanan M, Cutoff tailorability of heterojunction terahertz detectors, *Applied Physics Letters,* **82,** pp. 139-141, 2003.

[95] Rinzan M B M, Perera A G U, Matsik S G, Liu H C, Wasilewski Z R, and Buchanan M, AlGaAs emitter/GaAs barrier terahertz detector with a 2.3 THz threshold, *Applied Physics Letters,* **86,** pp. 071112-3, 2005.

[96] Zhu X Y, Yang Q, and Muntwiler M, Charge-Transfer Excitons at Organic Semiconductor Surfaces and Interfaces, *Accounts of Chemical Research,* **42,** pp. 1779-1787, 2009/11/17 2009.

[97] Gregg B A, The Photoconversion Mechanism of Excitonic Solar Cells, *MRS Bulletin,* **30,** pp. 20-22, 2005.

[98] Karl N, Kraft K H, Marktanner J, Munch M, Schatz F, Stehle R, and Uhde H M, Fast electronic transport in organic molecular solids?, Baltimore, Maryland (USA), 1999, pp. 2318-2328.

[99] Eisfeld A and Briggs J S, The J-band of organic dyes: lineshape and coherence length, *Chemical Physics,* **281,** pp. 61-70, 7/15/ 2002.

[100] Ribierre J C, Sato M, Ishizuka A, Tanaka T, Watanabe S, Matsumoto M, Matsumoto S, Uchiyama M, and Aoyama T, Organic field-effect transistors based on J-aggregate thin films of a bisazomethine dye, *Organic Electronics,* **13,** pp. 999-1003, 6// 2012.

[101] Siebbeles L D A, Huijser A, and Savenije T J, Effects of molecular organization on exciton diffusion in thin films of bioinspired light-harvesting molecules, *Journal of Materials Chemistry,* **19,** pp. 6067-6072, 2009.

[102] Głowacki E D, Voss G, Leonat L, Irimia-Vladu M, Bauer S, and Sariciftci N S, Indigo and Tyrian Purple – From Ancient Natural Dyes to Modern Organic Semiconductors, *Israel Journal of Chemistry,* **52,** pp. 540-551, 2012.

[103] Tian H and Meng F, Solar Cells Based on Cyanine and Polymethine Dyes, in *Organic Photovoltaics*, Sariciftci N S and Sun S, Eds., ed New York CRC Press, 2005, pp. 313-330.

[104] Hiramoto M, Kitada K, Iketaki K, and Kaji T, Near infrared light driven organic p-i-n solar cells incorporating phthalocyanine J-aggregate, *Applied Physics Letters,* **98,** pp. 023302-3, 01/10/ 2011.

[105] Deing K C, Mayerhoffer U, Wurthner F, and Meerholz K, Aggregation-dependent photovoltaic properties of squaraine/PC61BM bulk heterojunctions, *Physical Chemistry Chemical Physics,* **14,** pp. 8328-8334, 2012.

[106] Akselrod G M, Walker B J, Tisdale W A, Bawendi M G, and Bulovic V, Twenty-Fold Enhancement of Molecular Fluorescence by Coupling to a J-Aggregate Critically Coupled Resonator, *ACS Nano,* **6,** pp. 467-471, 2012/01/24 2011.

[107] Scheblykin I G, Lepnev L S, Vitukhnovsky A G, and Van der Auweraer M, Electroluminescence and optical properties of poly(phenylenevinylene)/J-aggregate composites, *Journal of Luminescence,* **94–95,** pp. 461-464, 12// 2001.

[108] Tischler J R, Scott Bradley M, Zhang Q, Atay T, Nurmikko A, and Bulović V, Solid state cavity QED: Strong coupling in organic thin films, *Organic Electronics,* **8,** pp. 94-113, 4// 2007.

[109] Kuznetsova Y Y, Remeika M, High A A, Hammack A T, Butov L V, Hanson M, and Gossard A C, All-optical excitonic transistor, *Optics Letters,* **14,** pp. 1587-1589, 2010.

[110] GrossoG, GravesJ, Hammack A T, High A A, Butov L V, HansonM, and Gossard A C, Excitonic switches operating at around 100 K, *Nat Photon,* **3,** pp. 577-580, 10//print 2009.

[111] Jayaweera P V V, Perera A G U, Senevirathna M K I, Pitigala P K D D P, and Tennakone K, Dye-sensitized near-infrared room-temperature photovoltaic photon detectors, *Appl. phys. Lett.,* **85,** pp. 5754-5756, 6 December 2004 2004.

[112] Jayaweera P V V, Pitigala P K D D P, Seneviratne M K I, Perera A G U, and Tennakone K, 1/f Noise in dye-sensitized solar cells and NIR photon detectors, *Infrared Physics & Technology,* **50,** pp. 270-273, 2007.

[113] Peumans P, Yakimov A, and Forrest S R, Small molecular weight organic thin-film photodetectors and solar cells, *Journal of Applied Physics,* **93,** pp. 3693-3723, 04/01/ 2003.

[114] Mishra A and Bäuerle P, Small Molecule Organic Semiconductors on the Move: Promises for Future Solar Energy Technology, *Angewandte Chemie International Edition,* **51,** pp. 2020-2067, 2012.

[115] Kim S-o, An T K, Chen J, Kang I, Kang S H, Chung D S, Park C E, Kim Y-H, and Kwon S-K, H-Aggregation Strategy in the Design of Molecular Semiconductors for Highly Reliable Organic Thin Film Transistors, *Advanced Functional Materials,* **21,** pp. 1616-1623, 2011.

[116] Matsumoto M, J-aggregate formation of dyes in Langmuir–Blodgett films, *Journal of Photochemistry and Photobiology A: Chemistry,* **158,** pp. 199-203, 6/2/ 2003.

[117] Decher G, Polyelectrolyte Multilayer an Overview, in *Multilayer Thin Films*, Decher G and Schlenoff J B, Eds., ed: Wiley-VCH, 2003, pp. 1-31.

[118] Fukumoto H and Yonezawa Y, Layer-by-layer self-assembly of polyelectrolyte and water soluble cyanine dye, *Thin Solid Films,* **327–329,** pp. 748-751, 8/31/ 1998.

[119] Okamoto K, Chithra P, Richards G, Hill J, and Ariga K, Self-Assembly of Optical Molecules with Supramolecular Concepts, *International Journal of Molecular Sciences,* **10,** pp. 1950-1966, 2009.

[120] Tennakone K, Abeysooriya P, Kahanda M, Kasige C, Kaviranta P, and Wijenayake R H, Dye sensitization of cuprous thiocyanate photocathode in aqueous thiocyanate, *J. Electrochem. Soc.,* **131,** pp. 1574-1577, 1984.

[121] Fernando C A N, de Silva P H C, Wethasinha S K, Dharmadasa I M, Delsol T, and Simmonds M C, Investigation of n-type Cu2O layers prepared by a low cost chemical method for use in photo-voltaic thin film solar cells, *Renewable Energy,* **26,** pp. 521-529, 8// 2002.

[122] Lange B, Lovrić M, and Scholz F, The catalytic action of adsorbed thiocyanate ions and thiourea in the electron transfer from glassy carbon to solid copper(I) selenide and copper(I) sulfide particles, *Journal of Electroanalytical Chemistry,* **418,** pp. 21-28, 11/21/ 1996.

[123] Safarowsky C, Spaenig A, Broekmann P, and Wandelt K, Reconstruction of a Cu(100) electrode in the presence of thiocyanate anions, *Surface Science,* **538,** pp. 137-146, 7/20/ 2003.

[124] Tennakone K, Dewasurendra M, and Hewaparakkrama K P, The exciton mediated photocurrent generation in a p-CuCNS photocathode sensitized with rhodamine B, *Solar Energy Materials,* **15,** pp. 475-483, 9// 1987.

[125] Greijer Agrell H, Lindgren J, and Hagfeldt A, Coordinative interactions in a dye-sensitized solar cell, *Journal of Photochemistry and Photobiology A: Chemistry,* **164,** pp. 23-27, 6/1/ 2004.

[126] Natoli L M, Ryan M A, and Spitler M T, J aggregate sensitization of zinc oxide electrodes as studied by internal reflection spectroscopy, *The Journal of Physical Chemistry,* **89,** pp. 1448-1453, 1985/04/01 1985.

[127] Jana A K, Solar cells based on dyes, *Journal of Photochemistry and Photobiology A: Chemistry,* **132,** pp. 1-17, 3/20/ 2000.

[128] Jayaweera P V V, Perera A G U, and Tennakone K, Why Gratzel's cell works so well, *Inorganica Chimica Acta,* **361,** pp. 707-711, 2/15/ 2008.

[129] IWASAKI M, KITA M, ITO K, KOHNO A, and FUKUNISHI K, INTERCALATION CHARACTERISTICS OF 1,1 '-DIETHYL-2,2'-CYANINE AND OTHER CATIONIC DYES IN SYNTHETIC SAPONITE: ORIENTATION IN THE INTERLAYER, *Clays and Clay Minerals,* **48,** pp. 392-399, 2000.

[130] Clark J, Silva C, Friend R H, and Spano F C, Role of Intermolecular Coupling in the Photophysics of Disordered Organic Semiconductors: Aggregate Emission in Regioregular Polythiophene, *Physical Review Letters,* **98,** p. 206406, 05/17/ 2007.

[131] Gierschner J, Directional exciton transport in supramolecular nanostructured assemblies, *Physical Chemistry Chemical Physics,* **14,** pp. 13146-13153, 2012.

[132] Orski S V, Fries K H, Sontag S K, and Locklin J, Fabrication of nanostructures using polymer brushes, *Journal of Materials Chemistry,* **21,** pp. 14135-14149, 2011.

[133] Tennakone K, Kumara G R R A, Kumarasinghe A R, Wijayantha K G U, and Sirimanne P M, A dye-sensitized nano-porous solid-state photovoltaic cell, *Semiconductor Science and Technology,* pp. 1689-1693, 1995.

[134] Bach U, Lupo D, Comte P, Moser J E, Weissortel F, Salbeck J, Spreitzer H, and Gratzel M, Solid-state dye-sensitized mesoporous TiO2 solar cells with high photon-to-electron conversion efficiencies, *Nature,* **395,** pp. 583-585, 10/08/print 1998.

[135] Ernst K, Belaidi A, and Konenkamp R, Solar Cell with extremely thin absorber on highly structured surface, *Semicond. Sci. Technol.,* **18,** pp. 475-479, 2003.

[136] Wright M and Uddin A, Organic—inorganic hybrid solar cells: A comparative review, *Solar Energy Materials and Solar Cells,* **107,** pp. 87-111, 12// 2012.

[137] Tennakone K, Kumara G R R A, Kottegoda I R M, Perera V P S, and Aponsu G M L P, Nanoporous n-/selenium/p-CuCNS photovoltaic cell *Journal of Physics D: Applied Physics,* **31,** p. 2326, 1989.

[138] Li Y, Sonar P, Murphy L, and Hong W, High mobility diketopyrrolopyrrole (DPP)-based organic semiconductor materials for organic thin film transistors and photovoltaics, *Energy & Environmental Science,* **6,** pp. 1684-1710, 2013.

[139] Tennakone K, Pitigala P K D D P, and Perera A G U, Exciton transport and electron mobility of organized aggregates of cationic dye thiocyanates, *RSC Advances,* **3,** pp. 2770-2775, 2013.

[140] Henary M and Mojzych M, Stability and Reactivity of Polymethine Dyes in Solution, in *Heterocyclic Polymethine Dyes*. **vol. 14**, Strekowski L, Ed., ed Berlin Heidelberg: Springer, 2008, pp. 221-238.

[141] Mojzych M and Henary M, Synthesis of Cyanine Dyes in Heterocyclic Polymethine Dyes, in *Heterocyclic Polymethine Dyes*. **vol. 14**, Strekowski L, Ed., ed Berlin Heidelberg: Springer, 2008, pp. 1-9.

[142] Bae E, Choi W, Park J, Shin H S, Kim S B, and Lee J S, Effects of Surface Anchoring Groups (Carboxylate vs Phosphonate) in Ruthenium-Complex-Sensitized TiO2 on Visible Light Reactivity in Aqueous Suspensions, *The Journal of Physical Chemistry B,* **108,** pp. 14093-14101, 2004/09/01 2004.

[143] Vujačić A, Vasić V, Dramićanin M, Sovilj S P, Bibić N, Hranisavljevic J, and Wiederrecht G P, Kinetics of J-Aggregate Formation on the Surface of Au Nanoparticle Colloids, *The Journal of Physical Chemistry C,* **116,** pp. 4655-4661, 2012/02/23 2012.

[144] Eisfeld A and Briggs J S, The J- and H-bands of organic dye aggregates, *Chemical Physics,* **324,** pp. 376-384, 5/31/ 2006.

[145] Verma S, Ghosh A, Das A, and Ghosh H N, Exciton-Coupled Charge-Transfer Dynamics in a Porphyrin J-Aggregate/TiO2 Complex, *Chemistry – A European Journal,* **17,** pp. 3458-3464, 2011.

[146] de Miguel G, Ziółek M, Zitnan M, Organero J A, Pandey S S, Hayase S, and Douhal A, Photophysics of H- and J-Aggregates of Indole-Based Squaraines in Solid State, *The Journal of Physical Chemistry C,* **116,** pp. 9379-9389, 2012/05/03 2012.

[147] Kawasaki M and Sato T, Direct Voltammetric Observation of Reversible and Irreversible Oxidations of Two-Dimensional J-Aggregates of Cyanine Dye, *The Journal of Physical Chemistry B,* **105,** pp. 796-803, 2001/02/01 2000.

[148] Perera V P S, Pitigala P K D D P, Jayaweera P V V, Bandaranayake K M P, and Tennakone K, Dye-Sensitized Solid-State Photovoltaic Cells Based on Dye Multilayer−Semiconductor Nanostructures, *The Journal of Physical Chemistry B,* **107,** pp. 13758-13761, 2003/12/01 2003.

[149] Senevirathna M K I, Pitigala P K D D P, and Tennakone K, Chromopore-Linked Conducting Polymers Attached to Semiconductor Surfaces: A Strategy for Development of Dye-Sensitized Solar Cells, *The Journal of Physical Chemistry B,* **109,** pp. 16030-16033, 2005/08/01 2005.

[150] Vogel R, Hoyer P, and Weller H, Quantum-Sized PbS, CdS, Ag2S, Sb2S3, and Bi2S3 Particles as Sensitizers for Various Nanoporous Wide-Bandgap Semiconductors, *The Journal of Physical Chemistry,* **98,** pp. 3183-3188, 1994.

[151] Wang Y, Suna A, Mahler W, and Kasowski R, PbS in polymers. From molecules to bulk solids, *The Journal of Chemical Physics,* **87,** pp. 7315-7322, 1987.

[152] K. Tennakone, I. R. M. Kottegoda, L. A. A. De Silva, and Perera V P S, The possibility of ballistic electron transport in dye-sensitized semiconductor nanocrystalline particle aggregates, *Semicond. Sci. Technol.,* **14,** 1999.

[153] K. Tennakone, P. K. M. Bandaranayake, P. V. V. Jayaweera, A. Konno, and Kumara G R R A, Dye-sensitized composite semiconductor nanostructures, *Physica E,* **14,** pp. 190-196, 2002.

[154] K. Tennakone, J. Bandara, P. K. M. Bandaranayake, G. R. A. Kumara, and Konno A, Enhanced Efficiency of a Dye-Sensitized Solar Cell Made from MgO-Coated Nanocrystalline SnO2, *Jpn. J. Appl. Phys. ,* **40,** p. L732, 2001.

[155] G. R. R. A. Kumara, K. Tennakone, V. P. S. Perera, A. Konno, S. Kaneko, and Okuya M J, Suppression of recombinations in a dye-sensitized photoelectrochemical cell made from a film of tin IV oxide crystallites coated with a thin layer of aluminium oxide, *Phys. D: Appl. Phys.,* **34,** p. 868, 2001.

[156] I. Bedja and P. V. Kamat, Capped Semiconductor Colloids. Synthesis and Photoelectrochemical Behavior of TiO2 Capped SnO2 Nanocrystallites, *J. Phys. Chem. B,* **99,** p. 9182, 1995.

[157] Hoyer P and Konenkamp R, Photoconduction in porous TiO_2 sensitized by PbS quantum dots, *Applied Physics Letters,* **66,** pp. 349-351, 1995.

[158] Black K, Jones A C, Chalker P R, Gaskell J M, Murray R T, Joyce T B, and Rushworth S A, MOCVD of ZnO thin films for potential use as compliant layers for GaN on Si, *Journal of Crystal Growth,* **310,** pp. 1010-1014, 2008.

[159] Xu Z-Q, Deng H, Xie J, Li Y, and Zu X-T, Ultraviolet photoconductive detector based on Al doped ZnO films prepared by sol-gel method, *Applied Surface Science,* **253,** pp. 476-479, 2006.

[160] J Baltrusaitis, C R Usher, and V H Grassian, Reactions of Sulfur Dioxide on Calcium Carbonate Single Crystal and Particle Surfaces at the Adsorbed Water Carbonate Interface, *Physical Chemistry Chemical Physics,* **9,** pp. 3011-3024, 2007.

[161] Fairley N, in *CasaXPS Version 2.3.14*, ed, 1999-2008.

[162] Y. Nosaka, Finite depth spherical well model for excited states of ultrasmall semiconductor particles: an application, *Journal of Physical Chemistry,* **95,** pp. 5054-5058, 1991.

[163] Zhang L and Yang L, A facile method to synthesize spherical PbS and their shape evolution process, *Cryst. Res. Technol. ,* **43,** pp. 1026-1029, 2008.

[164] N. N. Parvathy, G. M. Pajonk, and Rao A V, Synthesis and study of quantum size effect, XRD and IR spectral properties of PbS nanocrystals doped in SiO2 xerogel matrix, *J. Cryst. Growth,* **179,** pp. 249-257, 1997.

APPENDICES

Appendix A: Schematics of instrumentation setups used in measurements

Spectral Measurements

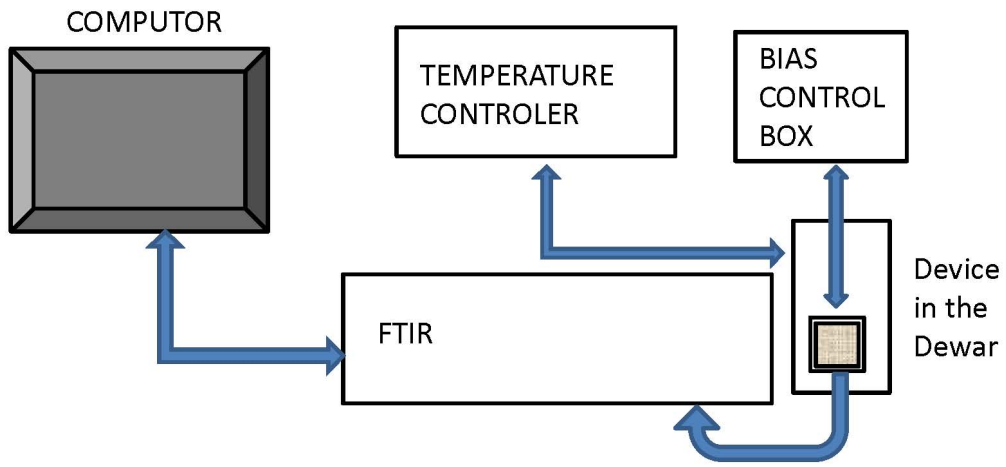

For the spectral measurements of the IR detectors, the device is mounted on a Dewar and illuminated using the infrared source in the Furrier Transform Infrared Spectrophotometer (FTIR). The device is biased using an external DC power supply. And a temperature is controlled by the attached temperature controller to the Dewar.

IVT and CVT measurements

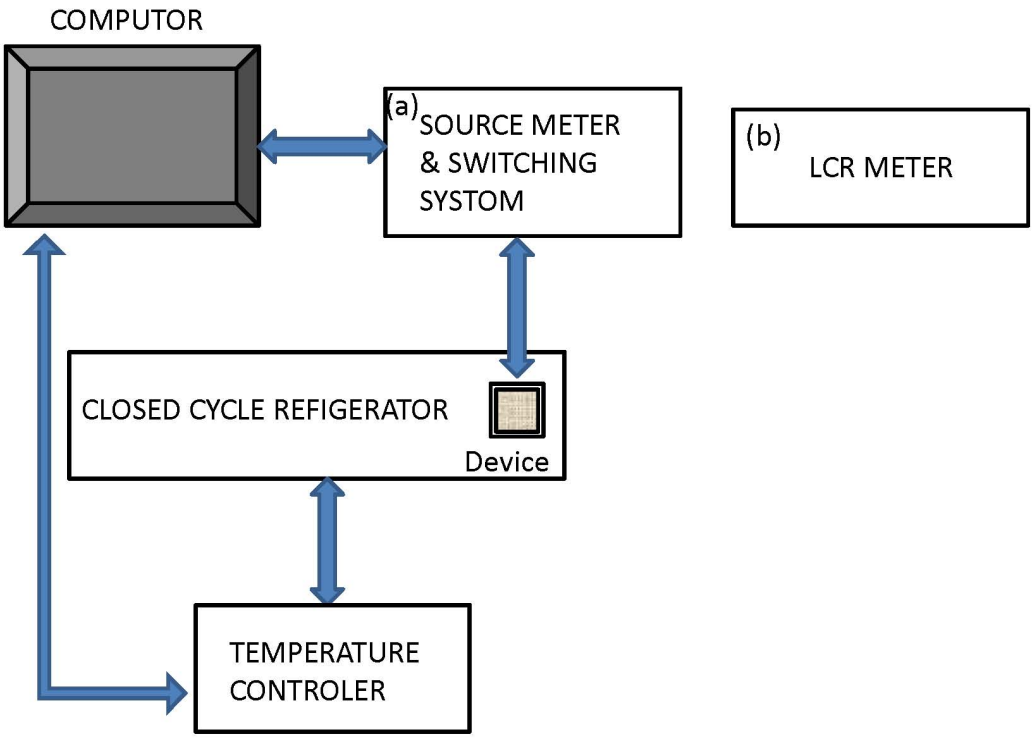

For the current-voltage-Temperature measurements, the device is mounted on a closed cycle refrigerator, connected with the temperature controller. The source meter is used to apply a bias and measure the current and a switching system is used to switch between different mesas in the sample. For capacitance – voltage measurements the source meter is replaced by the LCR meter.

Noise measurements

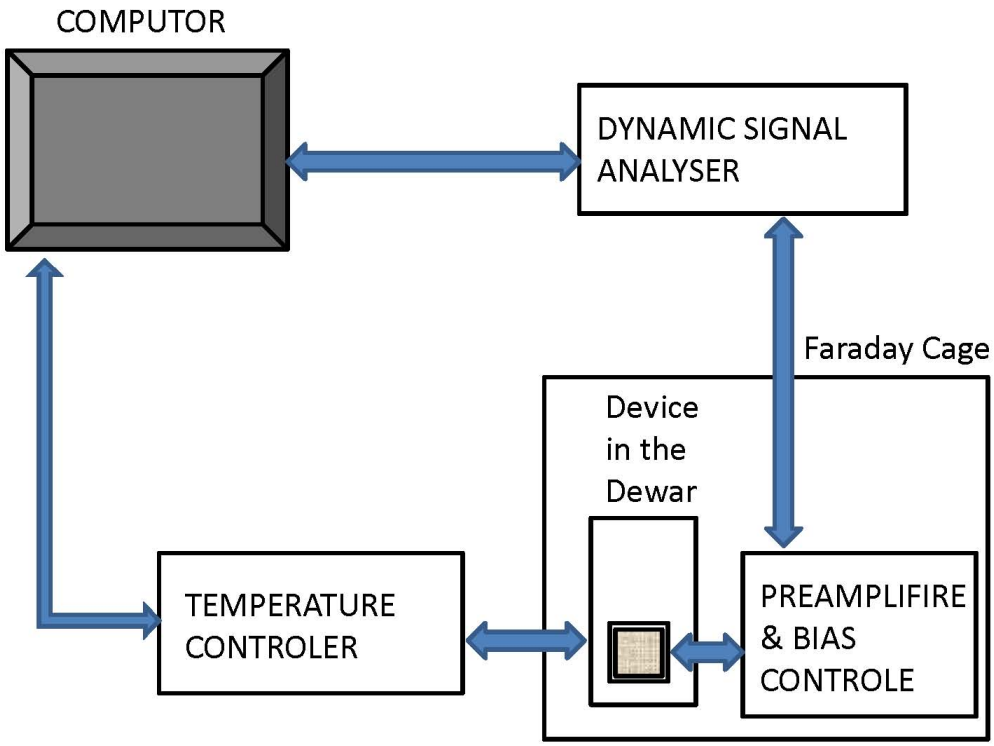

For noise measurements, the device is mounted in the Dewar and pleased inside a Faraday cage to isolate from outside background noise. Temperature controller is used for temperature dependent noise measurements. A bias voltage is applied through an alkaline battery pack or the internal DC power source in the preamplifier. The output signal is feed in to the dynamic signal analyzer.

Photoluminescence (PL) measurements

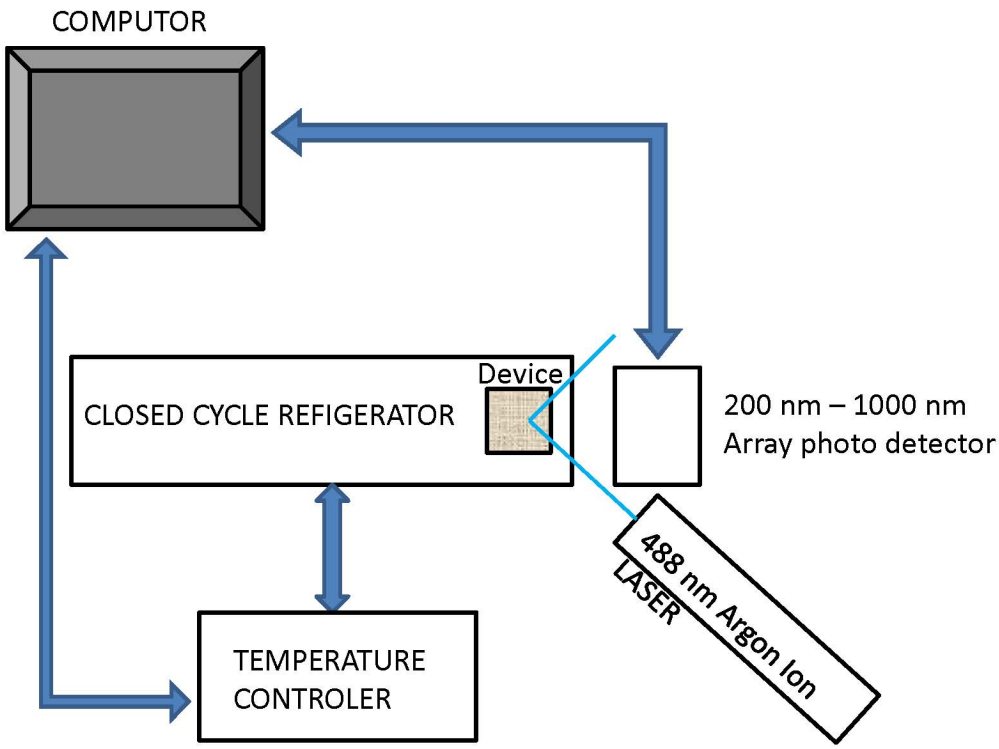

For photoluminescence measurements, the film samples were mounted in a closed cycle refrigerator attached with a temperature controller for temperature variant measurements. The 488nm Argon-Ion laser is used as the excitation beam and the emission is detected using a photodiode array system (Ocean Optics USB4000) sensitive in the 200 nm to 1000 nm wavelength region. For detecting the IR emission the FTIR is used as the detector, by feeding the emission radiation in the FTIR's external source port.

Appendix B: Preparation steps for dye sensitized solid state solar cells

Preparation of TiO2 colloid for compact TiO2 Films

TiO_2 colloid was prepared as described below. The chemical ingredients are,

1.	Titanium isopropoxide	5.0 ml
2.	acetic acid	5.5 ml
3.	Propan-2-ol	20.0 ml

These chemicals are added into a flask in the above order then mixed and stirred vigorously. After about 30 min stirring, adding 5 ml of H_2O drop vice (~ 1mL in every 5 minutes for duration of ~ 30 min).

After ~ 2 Hours stirring add 4 g of TiO2 (Degussa P25) and stirred them for overnight.

The colloidal TiO_2 prepared by this method was used to grow the nanoporous compact TiO_2 Film on the FTO glass as describe below,

- Painting the colloidal TiO_2 solution on the preheated FTO glass surface on a hot plate heated to ~150 C.
- TiO_2 painted glass plate is sintering at 450°C for 10 minutes in an oven.
- These baked glass plates were taken out from the oven and let them cool for few minutes, and then rube off the loose crust with cotton wool.
- This process is repeated for about 15-20 times until a film of ~8-10μm is formed. Finally the film is sintered at 450°C for an half an hour.

Selecting good quality TiO_2 Films for testing DSSCs

- Examine the TiO_2 film with a lamp illuminated from the back side.
    - You should only see a fade scattered light.
    - If no scattered light coming through the TiO_2 film, the thickness can be too high.
    - If direct light is observed, it implies the film thickness is low. You can try with several additional repetitions of the film growth procedure.
    - The TiO_2 film should be uniform everywhere: this can also be observed by scattered light coming through the TiO_2 film. Partially filled films are difficult to repair by additional rounds of growth procedure, these films cannot be used.
    - If there are scratches on the film they cannot be used.

Coating a layer of dye on the semiconductor surface

- Immerse the TiO_2 films in an alcoholic (Ethanol or Methanol) solution of the dye with a suitable molar concentration for desired time.
- Then the dye adsorbed films is rinsed with the alcohol to remove the excess dye molecules that were not properly chelated to TiO_2 surface.
- If testing for multilayer dye films, **do not** wash the film instead wipe of the glass to remove and dye molecules attached with the glass surface. If you need to wash find a solvent that will not detach the dye layers.

Some occasions a layer of dye can be painted on the semiconductor surface to fabricate thick dye layers (to fabricate more than a monolayer of dye).

Preparation and deposition of CuI and CuSCN for the DSSC

Deposition of CuSCN Films

A solution of CuSCN in propylsulfide was used in fabricating the p-type layer of the DSSSC.

- Dissolve ~ 50mg of the CuSCN powder in 8ml of propyl sulfide.
- Deposite CuSCN on the dye coated TiO_2 film by evenly spreading the CuSCN solution, while heating the Dye coated TiO_2 plate to ~90^oC on a hot plate
- Film is then dried in a warm air current to expel excess propyl sulfide.
- Test the photovoltage as you grow thin layers of CuSCN and stop depositing on more CuSCN when you reach maximum voltage.
- Carefully apply a graphite layer on the CuSCN

Deposition of CuI Films

- 1.2g of CuI powder was dissolved in 50ml of acetonitrile (methylcyanide).
- CuI was deposited on the dye coated TiO_2 film by evenly spreading the solution on dye coated TiO_2 plate placed on a hot plate at ~90^oC.
- Film is then dried in a warm air current to expel excess acetonitrile.
- Check the photocurrent and photovoltage as you grow thin layers of CuI; stop CuI deposition when you reach maximum performance.

Appendix C: Solar cell related basic measurements

I-V characteristics

The most important characteristic measurement in a solar cell is the I-V characteristics curve. I-V curve data are used to get a basic idea about the performance of the solar cell by the characteristic factors such as open circuit voltage (V_{oc}), short circuit current (I_{sc}), Fill Factor (FF %) and the efficiency (η%).

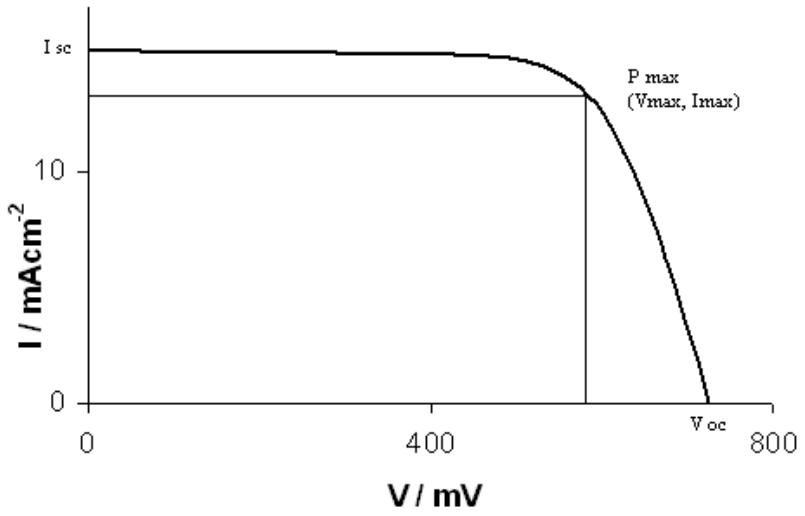

Figure C1: Illustration of a typical I-V curve with maximum power point marked on it.

Following equation is used to calculate the fill factor (FF)

$$FF\% = \left[\frac{(V_{\max})(I_{\max})}{(V_{oc})(I_{sc})} \right]$$

Where I_{max} and V_{max} are the current and voltage values at the maximum power point (P_{max}). V_{oc} and I_{sc} is the open circuit photovoltage and short circuit photocurrent of the solar cell (Figure C1).

Efficiency (η%) of a solar cell is calculated by,

$$\eta\% = \left[\frac{(V_{oc})(I_{sc})(FF\%)}{Incident\ Light\ Intensity} \right]$$

The Incident Light Intensity is $1000Wm^{-2}$ (or $100mWcm^{-2}$).

Photocurrent action spectrum and IPCE

Another informative characterization of a solar cell is photocurrent action spectrum (response spectrum) and the incident photon to photocurrent conversion efficiency (IPCE). With the action spectrum we can observe the current variation with the wavelength (λ) of the incident light spectrum. And the IPCE gives the number of electrons pass through in the external circuit per 100 photons incident on the solar cell at a specific wavelength.

$$IPCE\% = \left(\frac{No.\ of\ electronrs\ per\ \mathrm{sec}ond}{No.\ of\ Incident\ Photons\ per\ \mathrm{sec}ond} \right) * 100\%$$

Appendix D: LIST OF ABBREVIATIONS

AC: Acriflavine (3,6-Diamino-10-methylacridinium chloride)

CB : conduction band

CQD : colloidal quantum dot

CTO : conducting tin oxide

CuI : Copper Iodide

Cu_2O : Copper (I) Oxide

CUSCN : Copper Thiocyanate

DS: dye-sensitized

DSSCs: dye-sensitized solar cells

eV: electron volts

FDN: frequency dependent noise

FIR: far-infrared

FT-IR: Fourier-transform infrared

FTO: Fluorine doped tin oxide

G-R: generation-recombination

HEIWIP: heterojunction interfacial workfunction internal photoemission

HH or **hh:** heavy hole

HIWIP: homojunction interfacial workfunction internal photoemission

HOMO : highest occupied molecular orbital

IR: Infrared

LH or **lh:** light hole

LUMO : lowest unoccupied molecular orbital

MC: mercurochrome

MBE: moleculer beam epitaxy

NEP: Noise Equivalent Power

NIR : near-infrared

PbS: Lead Sulfide

QDs: Quantum dots

RhB: Rhodamine B ([9-(2-carboxyphenyl)-6-diethylamino-3-xanthenylidene]-diethylammonium chloride)

RhBSCN: Rhodamine B- Thiocyanate

THz : Terahertz

TiO_2 : Titanium dioxide

UV : ultraviolet

VB : valence band

ZnO : Zinc Oxide